New Developments in Ultrafast Polarization Sensitive Infrared Spectroscopy

---

Dissertation
zur
Erlangung der naturwissenschaftlichen Doktorwürde
(Dr. sc. nat.)

vorgelegt der
Mathematisch-naturwissenschaftlichen Fakultät
der
Universität Zürich

von
Julien Réhault
aus
Frankreich

Promotionskomitee
Prof. Dr. Peter Hamm (Vorsitz)
Dr. Jan Helbing
Prof. Dr. Jürg Hutter

Zürich, 2013

New Developments in Ultrafast Polarization Sensitive Infrared Spectroscopy

---

Dissertation
zur
Erlangung der naturwissenschaftlichen Doktorwürde
(Dr. sc. nat.)

vorgelegt der
Mathematisch-naturwissenschaftlichen Fakultät
der
Universität Zürich

von
Julien Réhault
aus
Frankreich

Promotionskomitee
Prof. Dr. Peter Hamm (Vorsitz)
Dr. Jan Helbing
Prof. Dr. Jürg Hutter

Zürich, 2013

*“There are some enterprises in which a careful disorderliness
is the true method.“*

Herman Melville, *Moby Dick*.

List of Publications

Some of the results presented here have been published and presented in the following journals and conferences.

Journal Publications

- J. Thøgersen, J. Réhault, M. Odelius, T. Ogden, N.K. Jena, S.J. Knak Jensen, S.R. Keiding, and J. Helbing
  Hydration dynamics of aqueous nitrate.
  Journal of Physical Chemistry B, **117** 3376-3388, 2013.

- J. Réhault and J. Helbing
  Angle determination and scattering suppression in polarization-enhanced two-dimensional infrared spectroscopy in the Pump-Probe Geometry.
  Optics Express, **20** (19) 21665–21677, 2012.

- J. Réhault, V.Zanirato, M.Olivucci and J. Helbing
  Linear dichroism amplification: Adapting a long-known technique for ultrasensitive femtosecond IR spectroscopy.
  Journal of Chemical Physics, **134** (12) 124516, 2011.

- J. Briand, O. Bräm, J. Réhault, J. Leonard, A. Cannizzo, M. Chergui, V. Zanirato, M. Olivucci, J. Helbing, S. Haacke
  Coherent ultrafast torsional motion and isomerization of a biomimetic dipolar photoswitch.
  Physical Chemistry Chemical Physics **12** (13) 3178-3187, 2010.

Conference Proceedings

- J. Réhault and J. Helbing
  Exploring the polarization degrees of freedom in collinear two-dimensional infrared spectroscopy
  In Ultrafast Phenomena XVIII, Oxford University Press, New York, 2012.

- J. Thøgersen, J.B. Nielsen, S.K. Jensen, S.R. Keiding, M. Odelius, J. Réhault and J. Helbing
  The rotation of NO_3^- (aq) as a probe of molecular ion-water interactions
  In Ultrafast Phenomena XVIII, Oxford University Press, New York, 2012.

Talks at Conferences

- J. Réhault and J. Helbing
  Amplification of linear dichroism for ultrasensitive femtosecond IR spectroscopy.
  XXV International Conference on Photochemistry 2011, Beijing (China), 2011.

- J. Réhault (invited) and J. Helbing
  Amplification du dichroisme linaire en spectroscopie ultrarapide infrarouge.
  9e Journées des Phénomènes Ultrarapides, Rouen (France), 2011.

- J. Réhault, V.Zanirato, M.Olivucci and J. Helbing
  Tracking ultrafast cis-trans isomerization with transient infrared anisotropy measurements
  XXIII IUPAC Symposium on Photochemistry, Ferrara (Italy), 2010.

- J. Réhault, V.Zanirato, M.Olivucci and J. Helbing
  Ultrafast infrared spectroscopy of new biomimetic photoswitches driven by Z/E isomerization
  International Conference on Photochemistry, Toledo (Spain), 2009.

Posters at Conferences

- J. Réhault and J. Helbing
  Amplification of linear dichroism for ultrasensitive femtosecond IR spectroscopy. Time Resolved Vibrational Spectroscopy XV, Ascona (CH), 2011.

- J. Réhault and J. Helbing
  Amplification of linear dichroism for ultrasensitive femtosecond IR spectroscopy. Swiss Chemical Society meeting, Lausanne (CH), 2011.

- J. Réhault, V.Zanirato, M.Olivucci and J. Helbing
  Tracking ultrafast cis-trans isomerization with transient infrared anisotropy measurements.
  Swiss Chemical Society meeting, Zürich (CH), 2010.

- J. Réhault, V.Zanirato, M.Olivucci and J. Helbing
  Ultrafast infrared sSpectroscopy of new biomimetic photoswitches driven by Z/E isomerization
  Swiss Chemical Society meeting, Lausanne (CH), 2009.

Contents

Abstract

The aim of this thesis was to study the ultrafast photoisomerization of a new class of biomimetic photoswitches proposed by the group of Prof. Olivucci from the university of Siena. These photoswitches undergo ultrafast and efficient *cis/trans* photoisomerization in a similar way to retinal, the photoreceptor of the human eye, which triggers the vision process. They can act as artificial chromophores, and also be linked to peptides or DNA strands to modulate biomolecular conformations. Also, the rotation motion accompanying the *cis/trans* isomerization makes these photoswitches interesting prototypes for molecular rotors fuelled by light. One prerequisite for this application is unidirectionality of rotation, which is what we aim to determine with ultrafast spectroscopies.

We used ultraviolet-pump infrared-probe and two dimensional infrared (2D-IR) spectroscopy with the particular emphasis on the manipulation of the polarization of the light pulses which trigger and monitor the photoswitching. Polarization measurements allows one to determine anisotropy, which can be directly related to structural information. We applied pump-probe spectroscopy on a newly designed zwitterionic switch, which carries a very large conformation dependent dipole moment. We showed that we can follow in time the isomerization process and determine its speed and efficiency in both *cis/trans* and *trans/cis* directions. This photoswitch has a chiral framework, meaning that it potentially isomerizes or rotates in a preferential direction. Based on the predicted structural changes during isomerization , we demonstrated that the time dependence of the anisotropy permits in principle to extract the direction of rotation. However, this required to boost the sensitivity of the pump-probe measurements, and motivated the developments of new strategies for amplifying the anisotropy signals.

We adapted a method called the near crossed polarizer technique to ultrafast infrared spectroscopies. With this, we demonstrated that we can strongly amplify pump-probe signals while removing unwanted background contributions. We additionally evidenced a gain of precision in the determination of angles between transition dipole moments. This is interesting considering the direct determination of the direction of rotation during *cis/trans* isomerization, but also a major improvement of the spectroscopy for structure determination in general. The method was further applied to 2D-IR spectroscopy, and revealed that in addition to increasing signals, it eliminated the scattering contributions which often limit the sensitivity of this technique. The manipulation of the pulse polarizations also permited to improve the flexibility of the 2D-IR spectroscopy set-up, which we demonstrated by measuring dispersive spectra.

Zusammenfassung

Das Ziel dieser Arbeit war es, die ultraschnelle Isomerisierung einer neuen Klasse von biomimetischen Photoschaltern zu untersuchen, die von der Arbeitsgruppe um Professor Olivucci der Universität Siena vorgeschlagen wurden. Ähnlich wie Retinal, dem Photorezeptor des menschlichen Auges, lassen sich diese Photoschalter sehr effizient und schnell zwischen ihren cis- und trans-Konformationen hin und herschalten. Sie eignen sich als künstliche Chromophore und lassen sich mit Peptiden oder DNA verbinden, um die Konformationen dieser Biomoleküle zu beeinflussen. Die Rotationsbewegung, die mit der Photoisomerisierung einhergeht, macht diese Photoschalter zudem zu interessanten Prototypen für lichtgetriebene molekulare Rotoren. Mit zeitaufgelöster Spektroskopie möchten wir bestimmen können, ob diese Drehbewegung nur in eine Richtung erfolgt, da dies eine Vorraussetzung für diese Entwicklung ist.

Pump-Probe Spektroskopie mit ultravioletter Anregung und Infrarotnachweis sowie zweidimensionale Infrarotspektroskopie (2D-IR) wurden eingesetzt. Besondere Bedeutung hatte dabei die Polarisation der für Start und Nachweis der Reaktion verwendeten Lichtpulse. Aus polarisationsabhängigen Messungen lässt sich die Anisotropie ermitteln, die direkte Schlüsse auf die Struktur der Moleküle erlaubt. Mit Pump-Probe Spektroskopie konnte die Isomerisierung eines neuartigen Photoschalters verfolgt werden, der zwitterionische Eigenschaften und ein sehr grosses, konformationsabhängiges Dipolmoment besitzt. Geschwindigkeit und Effizienz der Reaktion wurden in cis-trans sowie in trans-cis Richtung bestimmt. Der Photoschalter hat eine chirale Struktur, was bedeutet, dass die Isomerisierung oder Rotation in eine bevorzugte Richtung erfolgen sollte. Auf der Grundlage von theoretisch vorhergesagten Strukturänderungen während der Isomerisierung konnten wir zeigen, dass Anisotorpiemessungen im Prinzip in der Lage sind, den Drehsinn der Moleküle zu ermitteln. Jedoch wäre es hierfür notwendig, zunächst die Empfindlichkeit der Pump-Probe Experiments zu vergrössern. Dies begründete die Entwicklung neuer Strategien für die Verstärkung anisotroper Signale im zweiten Teil dieser Arbeit.

Wir haben die sogenannte Kreuzpolarisationsmethode für die ultraschnelle Infrarotspektroskopie weiterentwickelt und konnten damit zeigen, dass sich Pump-Probe Signals signifikant verstärken lassen, wobei gleichzeitig unerwünschte Hintergrundsignale unterdrückt werden. Dies ist nicht nur im Zusammenhang mit der Drehsinnbestimmung bei der cis-trans Isomerisierung interessant, sondern stellt auch eine wichtige Verbesserung der Pump-Probe Technik im Allgemeinen dar. Die Methode wurde im weiteren auf die 2D-IR Spektroskopie angewandt, wo zusätzlich zur Signalverstärkung auch Streulichtunterdrückung möglich ist. Damit konnte ein oft limitierender Faktor in der 2D-Spektroskopie vermieden werden. Die Polarisationskontrolle der Laserpulse erlaubte es weiterhin, die Vielseitigkeit des 2D-IR Aufbaus zu vergrössern. Dies wurde beispielhaft durch die Messung dispersiver Spektren gezeigt.

Introduction

Scientists have developed over the past century experimental and theoretical tools to study in detail the structure of molecules. Even when their chemical compositions were known in detail, the three-dimensional structures of complex biomolecules such as DNA and proteins were not known until the middle of last century. In 1962, the Nobel prize of chemistry was awarded to M.F. Perutz and J.C. Kendrew for the determination of the structure of haemoglobin with X-Ray spectroscopy. At the same time J.D. Watson and F.H.C. Crick received the Nobel prize of physiology and medicine for the discovery of the helical structure of DNA.

"If you want to understand function, study structure." said F. H. C. Crick [1]. The role of DNA and its structure allowed biologists to understand how genetic information is encoded into certain structural motifs. In the same way, the difference between oxygenated and reduced state of haemoglobin structure raised the question of the relation between function and structure, suggesting that structure may be an important factor for the activity of other biological systems. These findings are fundamental, and the study of structure with new experimental and theoretical tools has motivated a huge amount of research since. X-Ray diffraction has become the method of choice to determine the structure of crystalline compounds. In a similar manner, Nuclear Magnetic Resonance (NMR) spectroscopy has become the most powerful analytical method for elucidating the structure of proteins, and giving important dynamical information in the time scale of millisecond to microsecond [2]. NMR spectroscopy and X-Ray diffraction are now well developed analytical methods that are widely used by chemists.

Nonetheless, for studying fast chemical events such as bond breaking, isomerization, electron or proton transfer and conformational changes such as protein folding or unfolding, there is often a need for methods with better time resolution. In this regard, the advent of femtosecond lasers and their use for time-resolved spectroscopy has revolutionized chemistry and permitted the study of many chemical processes previously inaccessible. For example, the photodissociation of carbon monoxide from haemoglobin has been studied in real time with subpicosecond resolution, by using transient mid-infrared spectroscopy [3]. Also, picosecond X-ray crystallography has been used to study ultrafast structural changes in myoglobin, with a spatial resolution better than 2 Angström [4]. More than structure itself, the dynamics of structure is the purpose in this case.

Femtochemistry has emerged in the end of the last century as a new field of study, and many experimental methods have been developed with the aim of studying ultrafast events in chemistry. These methods are non-linear spectroscopies in the sense that the detected signal is proportional to the product of different electromagnetic fields. Second order spectroscopies give signals proportional to the product of two fields, third order signals are proportional to the product of three fields and so on. In this thesis, two related third order techniques are considered : pump-probe spectroscopy and two dimensional infrared (2D-IR) spectroscopy.

Pump-probe spectroscopy in the ultraviolet(UV), visible (Vis) and infrared (IR) is probably the most widely used technique in the ultrafast community. In particular, UV-pump IR-probe (UV-IR) spectroscopy aims to study the dynamics of molecular systems after photoexcitation in the UV. An electronic transition is induced by the pump pulse, triggering a chemical reaction. If this reaction is ultrafast and occurs within the time scales spanned by typical experiments (from femtoseconds to nanoseconds), one can track the entire reaction by monitoring changes in probe pulse absorption. Using broadband mid-infrared probe pulses, the resulting transient vibrational spectra can be related to molecular structure with the help of quantum chemistry calculations. Pump-probe spectroscopy has provided important insights into fundamental processes such as photodissociation [5], proton transfer [6], bond breaking [7] and *cis/trans* isomerization [8].

Whereas UV-IR pump-probe measurements are concerned with using IR spectroscopy to follow photoinduced processes, 2D-IR spectroscopy uses IR-pump IR-probe measurements to reveal additional structural information of the ground state. This is achieved by constructing a two-dimensional frequency map of the coupling between vibrational modes, which show up in a 2D spectrum as cross peaks. The additional axis of a 2D-IR spectrum is obtained by resolving the frequency of the pump excitation. 2D-IR spectroscopy provides information about molecular structure and structural changes [9–11], solute and solvent dynamics [12, 13], as well as on the nature of lineshape broadening [14, 15]. For example, 2D-IR spectroscopy has been used recently to resolve the structural changes accompanying the gating mechanism of the proton channel of influenza A, a virus responsible for flu [16]. This finding contributes to understanding the functioning of such viruses and find ways to limit their activity.

2D-IR spectroscopy has the potential to reveal structural changes happening in the time-scales between tens of femtoseconds and nanoseconds. Many different experimental strategies have been used to measure 2D-IR spectra. In this thesis, we used exclusively the pump-probe geometry, which has become one of the easiest ways to perform 2D-IR spectroscopy.

In both UV-IR pump-probe and 2D-IR spectroscopy, the polarization of the light fields is a key aspect for the determination of structural information. Polarization measurements can be used to manipulate the molecular response, and permit the calculation the anisotropy (or linear dichroism), which is the most direct structural information one can get from time-resolved spectroscopy, as it is related directly to an angle between the transition dipoles of vibrational modes.

The motivation of this thesis is the study of newly designed biomimetic photoswitches, which undergo an ultrafast *cis/trans* (or Z/E) isomerization in a similar way to retinal (see Fig. 1), the natural photoreceptor of rhodopsin, that triggers the vision process of superior animals. Retinal, incorporated into the protein membrane rhodopsin, is a model compound in terms of quantum yield and rate of isomerization [17–19]. When isolated in solution, due to other isomerization processes taking place, the photo-isomerization of retinal is slower, less efficient and less specific. A large body of experimental and theoretical work have been produced to explain the remarkable properties of retinal [20–25].

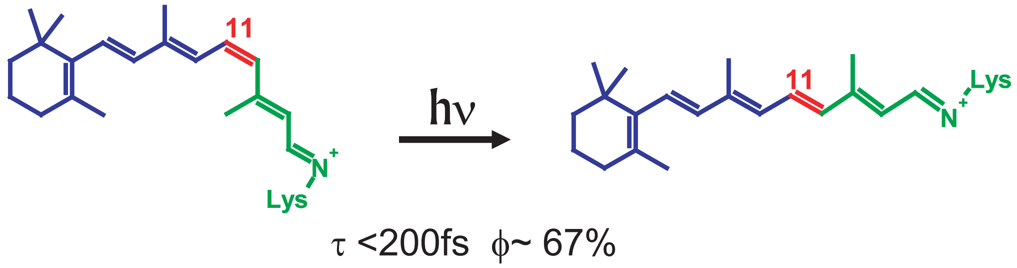

Figure 1: The *trans* to *cis* isomerization of Retinal occurs around the double bound C11, with a record time scale and quantum yield

Understanding the structural changes accompanying isomerization and deducing the most important parameters to achieve fast and efficient isomerization are essential for one who aims to build artificial photoswitches with improved properties. In this context, Prof. Olivucci and co-workers, have designed a new class of molecular switches based on the N-alkylated indanylidene-pyrroline Schiff base(NAIP) framework (Fig. 2), which mimic several aspects of the *cis/trans* isomerization of the Rhodopsin chromophore [26–28]. Theoretical predictions and experiments have already shown a remarkable agreement for a prototype methoxylated NAIP (MeO-NAIP) molecule [28]. It has been found that the excited state life time is as short as 300 fs, and that isomerization takes place on the same timescale. The molecules subsequently cool in the electronic ground state with a time-constant of less than 10 ps. A fully light-driven Z-E-Z cycle of MeO-NAIP can thus be completed in twenty picoseconds.

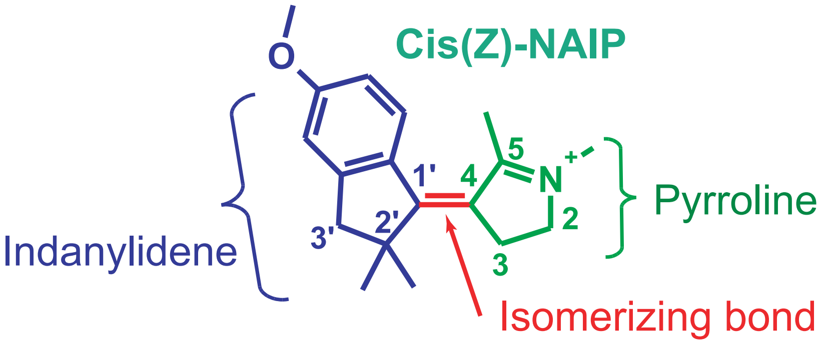

Figure 2: A NAIP photoswitch in the *cis* form. The pyrroline moiety is expected to rotate around the isomerizing bond after photoexcitation, while the indanylidene moiety is mostly static, justifying the application for molecular rotors.

In the first part of this thesis, we introduce the relevant background theory in chapter 1 and the experimental details in chapter 2. We present in part II our results on a NAIP zwitterion. ZW-NAIP is a chiral variant of the MeO-NAIP, with the notable feature that it carries a very large 15 Debye dipole moment on the pyrroline moiety. The *cis/trans* isomerization of ZW-NAIP thus entails an unusually strong 30 Debye dipole change by inverting the dipole direction in the molecular frame. Transient infrared absorption data are presented with the support of ultrafast visible spectroscopies performed by collaborators from the University of Strasbourg (Group of Prof. Haacke) and École Polytechnique Fédérale de Lausanne (group of Prof. Chergui).

ZW-NAIP is a good candidate for the achievement of unidirectional photo-isomerization. It has been predicted that chirality determines the unidirectional nature of the cis-trans isomerization. This is a crucial aspect in building molecular rotors fuelled by light. The work presented here is motivated by the possibility of detecting unidirectional rotation with ultrafast IR spectroscopies. In chapter 4 we demonstrate that with anisotropy measurements, we have a direct insight into structural changes, and can make use of the time dependence of anisotropy for determining the direction of rotation over the course of *cis/trans* isomerization. These observations motivated the need to develop new methods of increasing the sensitivity of the experiments to anisotropy.

In part III, we show in chapter 5 theoretically how to increase the signal to noise ratio (S/N) of our experiments by exploiting the properties of anisotropy and manipulating the pump and the probe polarizations [29]. For this purpose, we use the near crossed polarizer geometry. Placing polarizers in the probe beam permits the use of intense fields at the sample, amplifying the anisotropic signal. We explain how we can obtain more precise structural information from the signals compared with conventional anisotropy measurements. The enhancement of S/N and flexibility are explained as well as certain technical limitations. In chapter 6 we demonstrate this method on a photoswitch of the NAIP family introduced earlier. We propose different experimental implementation that use the crossed polarizer technique, and discuss their advantages and drawbacks.

In a similar fashion, we use the near crossed polarizer technique to improve the S/N of 2D-IR spectroscopy in the pump-probe geometry [30]. We show in chapter 7 that unwanted artefacts that normally perturb the measured signals can be removed with our method. We also improve the flexibility of the experiment with regard to measuring signals that are not normally accessible in the pump-probe geometry.

We finally summarize the results shown in this thesis and give some perspectives and conclusions of this work.

Part I

Methods

In this first part, we develop the formalism needed to understand the signals measured in third order non-linear spectroscopy. Starting with the general expression of the third order polarization, we explain the different contributions that participate to the measured third order signal. We formulate it for the specific one dimensional (1D) UV-pump/IR-probe spectroscopy and on two dimensional infrared spectroscopy (2D-IR). The light pulse polarization is taken into account in the molecular response. The formulation of induced third order non-linear polarization is given in function of the response functions R_n which were derived previously in the literature [31, 32]. As a theoretical background, double-sided Feynman diagrams and isotropic averages are used. Additional information on these concepts can be found in appendices A and B. The pump-probe geometry is discussed and compared to the alternative four-wave mixing geometry.

The second chapter presents the technical details of the different experiments that we used during this thesis. The study of ultrafast chemical processes with spectroscopy relies first on ultrafast laser sources. These apparatus generate ultrashort laser pulses in the near IR. Their frequency can be converted using non-linear optical processes to the mid-IR or visible and ultraviolet range. Then, the pulses are combined into the set-ups. The two set-ups mentioned in the introduction, i.e. UV-IR and 2D-IR are described in this chapter. Some technical details like polarization modulation and polarizers are presented.

Chapter 1

Non-linear signals in the pump-probe geometry.

1.1 Signals in 3^{rd} order spectroscopy

In non-linear spectroscopy, light-matter interaction is described using the formalism of the density matrix, which is used to describe the statistical ensemble of quantum states of the system under study. Three input fields, provided by the ultrashort laser pulses, create a third order non-linear polarization in the sample. Two fields are provided by the pump pulse, E_1 and E_2, while the third field E_3 comes from the probe pulse.

Then, the third order non-linear polarization $P^{(3)}$ gives rise to a signal field E_{sig} which we are interested in. An additional field E_{LO}, called local oscillator, is added for heterodyne detection.

1.1.1 General formulae

We start from the expression of the third order non-linear polarization in the interaction picture, created by three input fields E_1,E_2 and E_3 , that interact with a molecule at times τ_1, τ_2, and τ_3 respectively [31, 32]

$$\begin{aligned}\overrightarrow{P}^{(3)}(t) = \left(\frac{i}{\hbar^3}\right) \int_{-\infty}^{t} d\tau_3 \int_{-\infty}^{\tau_3} d\tau_2 \int_{-\infty}^{\tau_2} d\tau_1 \\ \times\, Tr\left(\overrightarrow{\mu}(t)[\overrightarrow{E}_3.\overrightarrow{\mu}(\tau_3),[\overrightarrow{E}_2.\overrightarrow{\mu}(\tau_2),[\overrightarrow{E}_1.\overrightarrow{\mu}(\tau_1),\rho(-\infty)]]]\right)\end{aligned} \tag{1.1}$$

where $\rho(-\infty)$ is the density matrix of the unperturbed system, μ the dipole operator, and where the fields are vector expressions to take into account their polarization state. The square brackets are used for the commutation operation, and Tr is used to represent the trace of the matrix. The commutator in Eq. 1.1 will give rise to different terms R_n that we call response function, corresponding to different Liouville pathways [31–33], that can be represented with double-sided Feynman diagrams (see Fig. 1.1).

For a single vibrational transition, and when the molecules are initially all in the fundamental vibrational state (the density matrix is $\mid 0\rangle\langle 0 \mid$), the commutator will give rise to twelve terms described by six Feynman diagrams and their complex conjugate. These Feynman diagrams are depicted in Fig. 1.1. For the description and use of Feynman diagrams, the reader can refer to appendix A.

We first consider the fields and the transition dipole moments as scalar quantities, we will reintroduce later the polarization of the fields and the orientation of the transition dipole moment. We can re-write the total polarization as a sum of the different response functions cor-

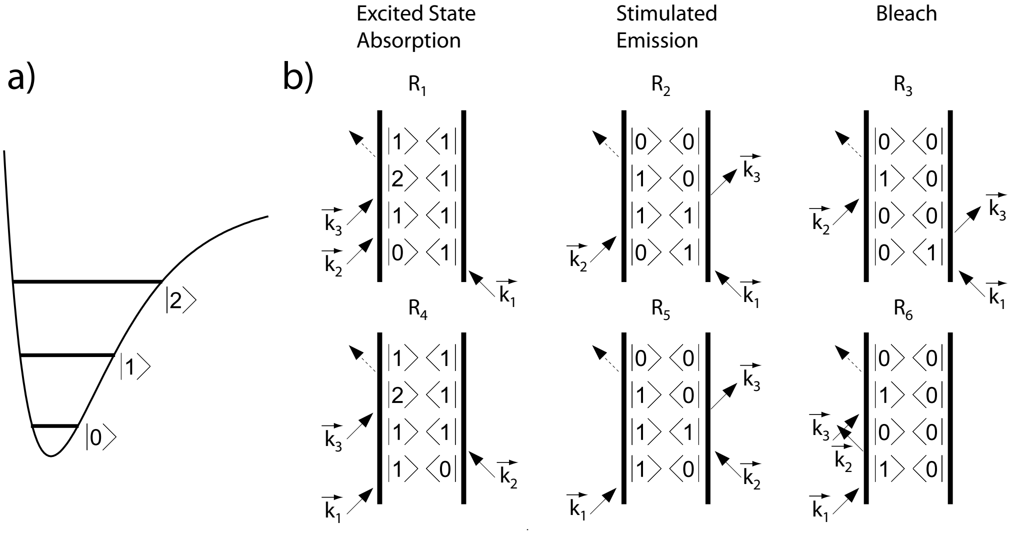

Figure 1.1: a) Morse potential with 3 vibrational levels. b) Feynman diagrams describing the evolution of the density matrix after each of the 3 interactions with the light field at time τ_1,τ_2 and τ_3.

responding to different Feynman pathways, and replacing absolute time τ's with time intervals t's [1]:

$$P^{(3)}(t) \propto -i \int_0^\infty dt_3 \int_0^\infty dt_2 \int_0^\infty dt_1 E_3(t-t_3).E_2(t-t_3-t_2) \\ .E_1(t-t_3-t_2-t_1) \sum_n R_n(t_3,t_2,t_1) \tag{1.2}$$

The electric fields come from short laser pulses which are long in comparison to the oscillation of the light field, but short in comparison to the time-scales of the system. We are then in the semi-impulsive limit [31,32], and the envelop of the pulses are approximated by delta functions, but they keep their carrier frequency ω, phase ϕ and wave-vector $\overrightarrow{k}$:

$$E_n \propto \delta(\tau_n) e^{\pm i\omega\tau_n \mp i\overrightarrow{k}.\overrightarrow{r} \mp i\phi} \tag{1.3}$$

In this limit, the convolutions in Eq. 1.1 vanish, and the third order polarization reflects directly the response functions, which carries the information we are interested in:

$$P^{(3)}(t_3,t_2,t_1) \propto e^{i(\mp\overrightarrow{k_1} \pm \overrightarrow{k_2} + \overrightarrow{k_3})\overrightarrow{r}} e^{i(\pm\phi_1 \mp \phi_2 + \phi_3)} \sum_n R_n(t_3,t_2,t_1) \tag{1.4}$$

The third-order polarization emits a field E_{sig} with a 90° phase shift, referred to as optical free induction decay :

$$\overrightarrow{E}_{sig}(t_3,t_2,t_1) \propto i\overrightarrow{P}^{(3)} \\ \propto e^{i(\mp\overrightarrow{k_1} \pm \overrightarrow{k_2} + \overrightarrow{k_3})\overrightarrow{r}} e^{i(\pm\phi_1 \mp \phi_2 + \phi_3)} \sum_n iR_n(t_3,t_2,t_1) \tag{1.5}$$

---

[1] the t_i are the time intervals between τ_i and τ_{i+1},

Signal field are usually weak and can not be homodyne detected, which means we can not detect them directly with a detector. We use a technique of heterodyne detection, which consist of mixing the signal field with an external field called local oscillator (LO). The signal S that we measure is the interference on the detector of the signal field (E_{sig}) with a local oscillator field (E_{LO}). The detectors we used are square law detectors, so that they are sensitive to intensities and not to field. They integrate interferences of the fields over their duration:

$$\begin{aligned} S(t_3, t_2, t_1) &\propto \int_0^{\infty} \mid E_{LO}(t_3 - t_{LO}) + E_{sig}(t_3, t_2, t_1) \mid^2 dt_3 \\ &\approx I_{LO} + 2\Re \int_0^{\infty} \{E_{LO}(t_3 - t_{LO}).E_{sig}(t_3, t_2, t_1)\} dt_3 \end{aligned} \tag{1.6}$$

where we neglected the homodyne term $\mid E_{sig} \mid^2$, and wrote the intensity $I_{LO} = \mid \ E_{LO} \ \mid^2$. Again, in the semi-impulsive limit, the integrand disappears, so that we get:

$$S(t_3, t_2, t_1) \approx I_{LO} + 2\Re \left(E_{LO}.E_{sig}(t_3, t_2, t_1)\right) \tag{1.7}$$

Measuring the signal through a spectrometer with an array detector is equivalent to do a Fourier transformation of the fields with respect to time t_3 prior to detection. We get then a spectrum along the probe direction:

$$\begin{aligned} S(\omega_3, t_2, t_1) &\approx \int_0^{\infty} S(t_3, t_2.t_1) e^{i\omega_3 t_3} dt_3 \\ &\approx I_{LO}(\omega) + 2\Re \left(E_{LO}.E_{sig}(\omega_3, t_2, t_1)\right) \end{aligned} \tag{1.8}$$

The signal field $E_{sig}(\omega_3, t_2, t_1)$ (now E_{sig})is proportional to i times the non-linear polarization $P^{(3)}$ (Eq. 1.5), which is itself proportional to i times the probe field ($= E_{LO}$ here); the product of the two i's gives E_{sig} the opposite sign to E_{LO}, so that E_{sig} interferes destructively with E_{LO} which leads to an absorption[2]. The polarization has in fact an absorptive imaginary component and a dispersive real component. The two are dependent and connected through the Kramers-Kronig relation so that measuring one or the other leads to the same information (see section 7.5).

If we want to measure absorption, when E_{LO} and E_{probe} are in phase, we compare the intensity detected when the pump field is on and off, and take the decadic logarithm:

$$\begin{aligned} \Delta A(\omega_3, t_2, t_1) &\propto -\log_{10}\left(\frac{S(\omega_3, t_2, t_1)}{I_{probe}}\right) \\ &\propto -\log_{10}\left(1 + \frac{E_{LO}.E_{sig}}{\mid E_{LO} \mid^2}\right) \end{aligned} \tag{1.9}$$

For small signals in comparison to the heterodyning field, we get:

$$\Delta A(\omega_3, t_2, t_1) \approx \frac{\mid E_{sig} \mid}{\mid E_{LO} \mid} \tag{1.10}$$

---

[2] Alternatively, if a phase shift of $\frac{\pi}{2}$ is applied to E_{LO} only, we then multiply the product $(E_{LO}(\omega).E_{sig}(\omega)$ by $e^{\frac{i\pi}{2}} = -i$, and we then measure a dispersive lineshape, see chapter 7.5.

So that the measured absorption is directly proportional to the signal field but inversely proportional to the heterodyning field.

The signal measured are typically small, and the quality of the data depends on the signal to noise ratio (S/N) that we can achieve. Increasing E_{sig} while keeping E_{LO} as small as possible guarantees the best S/N.

Below, we present two experimental set-up usually used to measure third order signals : the four-wave mixing geometry and the pump-probe geometry. We explain advantages and drawbacks regarding their simplicity, sensitivity and flexibility.

1.1.2 Four-wave mixing geometry vs pump-probe geometry

Four-wave mixing geometry

The determination of the third order polarization requires to use three light pulses for which we have to precisely know the phase and time difference (Eq. 1.1 and 1.5), and to overlap them spatially on the sample. A fourth pulse can be used for heterodyne detection. The use of four different beams with different k vectors (or directions) is referred to as four-wave mixing, and is considered as the most sensitive and flexible way of measuring 2D spectra for reason that are listed below.

This configuration is introduced briefly here as it was not used in this thesis. This technique is the most complete of the third order spectroscopy and can be more easily related to the equations presented in the previous section.

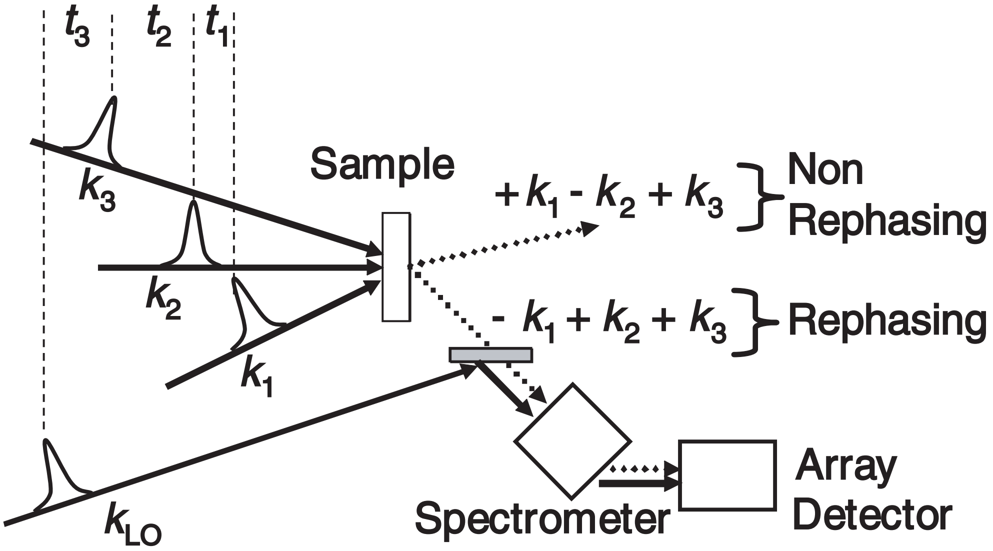

Figure 1.2: Four-wave mixing set-up for 2D measurements. The three excitation pulses represented by wave-vectors k_1, k_2 and k_3 are overlapped on the sample. Two third order signals, rephasing and non-rephasing, are emitted in different directions. Overlapping one of them with the LO allows heterodyne detection on the detector.

In the four-wave mixing geometry, like it is sketched in Fig. 1.2, the signal is emitted in the phase matching direction ($\overrightarrow{k}_{sig} = \sum_{i=1}^{3} \overrightarrow{k}_i$) and the LO field is set so to overlap the emitted signal field (Eq. 1.5). It has to be noted that in this geometry, not all the Feynman pathways of Fig. 1.1 are measured simultaneously. The diagrams corresponding to the response function R_1, R_2 and R_3 are emitted in a different direction than the R_4, R_5 and R_6 diagrams. The first three are called rephasing diagrams and the three last non-rephasing diagrams for a reason that is explained in appendix A. To measure the full response, one needs to measure both rephasing and non-rephasing diagrams, which, according to Fig. 1.2 requires to move the LO field and the detector to overlap the rephasing or the non-rephasing signal. In practice, the two are measured by exchanging pulse 1 and 2 which is equivalent to exchanging the phase matching direction of rephasing and non-rephasing signals.

The signal measured this way is a function of t_1, t_2 and ω_3 (or ω_{probe}). To generate a 2D spectra, we have to make a Fourier transform along time t_1, which will generate the axis ω_1 (or ω_{pump}). Summing rephasing and non-rephasing contributions gives the better spectral resolution and leads to absorptive lineshapes, which are more intuitive and easier to interpret [34] (see Fig. 1.3). One advantage of the four-wave mixing geometry is the flexibility, as the intensities, polarizations and timings of the pulses can be tuned individually. A second advantage is the sensitivity, as the intensity of the LO can be set independently from the intensity of the other pulses (We will see that it is not the case in a usual pump-probe geometry).

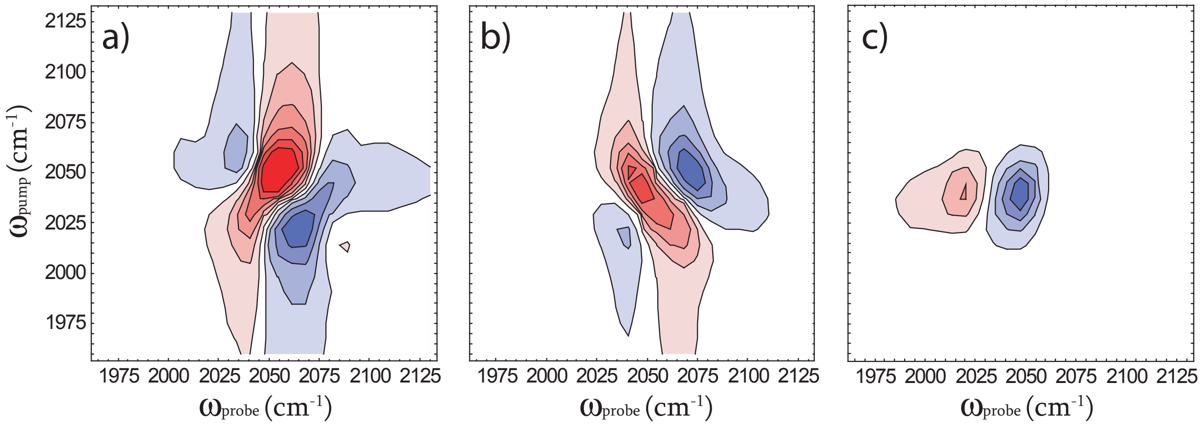

Figure 1.3: 2D-IR spectra of azide in water. a) Rephasing spectra b) Non-rephasing spectra c) Absorptive spectra, calculated summing rephasing and non-rephasing spectra. Blue corresponds to a lack of absorption and red to absorption.

Drawbacks are the complexity of alignment, the difficulty of phase determination at the sample and the necessity of doing two successive measurements to get an absorptive spectrum.

The pump-probe geometry

In the pump-probe geometry in its most simple form, a pump pulse excites the sample before a delayed probe pulse monitors the difference of absorption with and without excitation, and the probe pulse is then dispersed in a spectrometer (Fig. 1.4). The pulses have a duration in the order of 100 fs, and the delay between the pulses can be set precisely using a delay stage. The ultrafast dynamics of the system is studied measuring for example the transient absorption at various delays. This scheme is intensively used in chemistry [35] and in the infrared [36]. The advantage of this configuration which makes it so popular is that the interpretation of the spectra is intuitive, as it usually does not require the understanding of theoretical formalism developed earlier. However, use of this formalism allows one to have a better understanding of what contributes to the signal, and can be used to increase the S/N and manipulate the molecular response as we will show later on. The pump-probe geometry was also used to acquire the first 2D-IR spectra in the frequency domain [37]. An alternative time-domain approach of 2D-IR spectroscopy can also be achieved with this geometry [38–40]. For the different methods used to acquire 2D-IR spectra, the reader can consult chapter 9 of ref. [32]

In this thesis, we use exclusively the pump-probe geometry. The probe pulses are always in the infrared range, and thus monitor the vibrational changes induced by the pump pulse. Pump pulses can be either in the UV or the IR range, triggering electronic or vibrational excitation. In the pump-probe geometry, the two first interactions are collinear and the probe acts as the third interaction and also as a heterodyning field. Only two beams have to be overlapped on the sample.

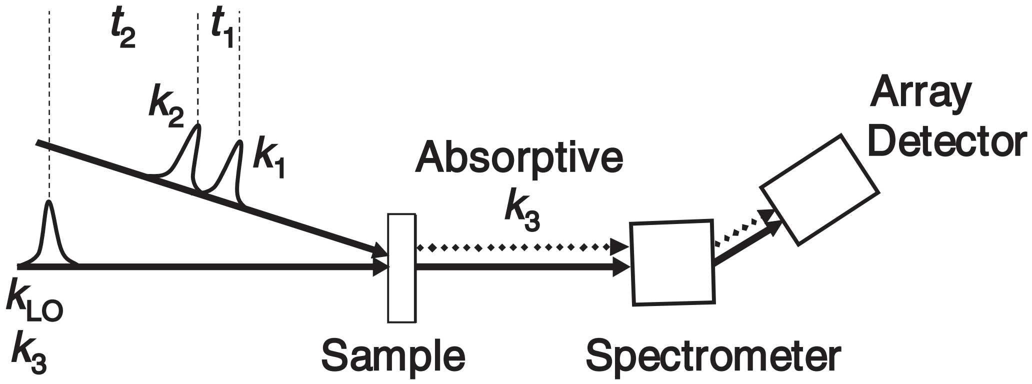

Figure 1.4: 2D set-up in the pump-probe geometry. Absorptive spectra (sum of rephasing and non-rephasing spectra) are measured.

From Eq. 1.10, we can see that as the signal field is proportional to the probe which is also the LO field. The measured absorption is in this case independent of the probe intensity. Still, it is interesting to increase the probe field intensity, because the S/N of the experiment depends on the quantity of light on the detector, whose dynamic range is usually a limiting factor.

This is actually a limitation of the pump-probe geometry, that the signal magnitude is independent of the probe intensity [38]. Because the probe and the LO fields are coming from the same beam[3], they are both measured on the detector, whose dynamic range limits the intensity we can put on the probe beam. One aim of this thesis is to enhance sensitivity and

---

[3] We then talk about self-heterodyning

flexibility of the pump probe geometry, using polarization tricks to separate the probe and local oscillator fields.

In the pump probe geometry, several simplifications on the formulation of the signal of Eq. 1.5 arise:

First, the pump fields E_1 and E_2 are coming from the same pulse and have same amplitude, phase and wavevectors , so that we note:

$$\begin{aligned} E_{pump} &= E_1 = E_2 \\ \overrightarrow{k_1} &= \overrightarrow{k_2} \\ \phi_1 &= \phi_2 \end{aligned} \tag{1.11}$$

Second, as mentioned earlier, the signal emitted from the sample and due to the polarization $P^{(3)}(t)$ has the same direction that the probe field E_3 and LO field E_{LO} (see Appendix A). We can make the simplification:

$$\begin{aligned} E_{probe} &= E_3 = E_{LO} \\ \overrightarrow{k_{LO}} &= \overrightarrow{k_{probe}} \\ \phi_{LO} &= \phi_{probe} \\ t_3 &= 0 \end{aligned} \tag{1.12}$$

Moreover, rephasing and non-rephasing signals are emitted in the same direction, and both are measured simultaneously, leading directly to absorptive spectra [38].

The signal field then becomes the simple expression:

$$E_{sig} \propto \sum_n iR_n(t_3, t_2, t_1) \tag{1.13}$$

Two different pump-probe set-ups are used for UV-pump IR-probe and for 2D-IR spectroscopy. The former leads to one dimensional spectra, and the pump frequency is not resolved in that case, as the same UV pump pulse creates the two first interactions (see chapter 6). The latter leads to 2D-IR spectra and is presented in chapter 7.

1.2 Polarization control of the molecular response

Polarization of the fields interacting with the sample is of a great importance in 1D or 2D-IR spectroscopy[4]. Comparing signals with a probe pulse polarized parallel or perpendicular relative to the pump pulse polarization permits to measure angles between transition dipole moments, and to study the rotational diffusion of molecules [41–45]. In the general expression of polarization $\overrightarrow{P}^{(3)}$ in Eq. 1.1, the electric fields and transition dipole moments are vector quantities, and the different scalar product $\overrightarrow{E_i}.\overrightarrow{\mu}(\tau_i)$ are dependent of the relative orientations of fields and dipole moments. Thus, the response function of a system also exhibits an orientational dependence.

---

[4] The reader might be confused by the use of the word "polarization" with two different meanings. It is important to distinguish polarization of matter, which is the separation of charges of opposite sign in matter and the polarization of light, which is related to the direction of the electromagnetic field. We try to make the distinction clear when not obvious.

1.2.1 Orientational four-point correlation functions

The way to treat the orientation dependence of the signals is to separate the rotational and vibrational terms, which implicitly assumes that vibrational and rotational motions are uncorrelated. This is done in the equations expressing the vector quantities as a product of an amplitude and a unit vector. The electric fields and transition dipole moments can be written as:

$$\overrightarrow{E}_n = \delta(\tau_n) e^{\pm i\omega\tau_n \mp i\overrightarrow{k}.\overrightarrow{r} \mp i\phi} \overrightarrow{e}_n \tag{1.14}$$

$$\overrightarrow{\mu} = \mu \overrightarrow{u} \tag{1.15}$$

where $\overrightarrow{e}_n$ and $\overrightarrow{u}$ are unit vectors, which represents respectively the polarization of the field and the transition dipole moment orientation in the frame of the laboratory.
As seen in Eq. 1.2, the third order polarization can be expressed in function of the different response functions $R_n(t_1, t_2, t_3)$, and each of the response will have a different orientational dependence, as the transition dipoles involved in the successive interactions are not the same. Now we introduce the orientational dependence of the measured signal :

$$\overrightarrow{\Theta}(R_n) = (\overrightarrow{u}(\tau_3)\,(\overrightarrow{u}(\tau_2).\overrightarrow{e}_3)\,(\overrightarrow{u}(\tau_1).\overrightarrow{e}_2)\,(\overrightarrow{u}(\tau_0).\overrightarrow{e}_1)) \tag{1.16}$$

so that we can rewrite Eq. 1.4:

$$\overrightarrow{P}^{(3)}(t_3, t_2, t_1) \propto \sum_n \overrightarrow{\Theta}(R_n) R_n(t_3, t_2, t_1) \tag{1.17}$$

Now the heterodyne signal is a scalar product between $\overrightarrow{E}_{LO}$ and $\overrightarrow{P}^{(3)}$.

$$S \propto \overrightarrow{E}_{LO}.\overrightarrow{E}_{sig} \propto i\overrightarrow{E}_{LO}.\overrightarrow{P}^{(3)} \tag{1.18}$$

and the signal can be expressed as follows:

$$S \propto \sum_n \overrightarrow{e}_{LO}.\overrightarrow{\Theta}(R_n) R_n(t_3, t_2, t_1) \tag{1.19}$$

So that all the orientation dependence of the molecular response is contained in the scalar product $\overrightarrow{e}_{LO}.\overrightarrow{\Theta}(Rn)$, while the $R_n(t_3, t_2, t_1)$ terms contain the vibrational dependence of the signal.

Eq. 1.19 represents the response of a molecular ensemble with fixed orientation(all molecules have the same orientation), but this is of course not the case when we deal with systems in the condensed phase. The molecules are isotropically distributed, so that the expression of the detected signal requires the summation over all possible orientation of the molecules. There is a way to predict signals using isotropic averages [137], which are detailed in appendix B. From now on, we use the symbols $\langle .. \rangle$ to refer to the bulk response after isotropic averaging.

What we can control in an experiment is the polarization orientation of the fields. In this thesis, the light propagates along the Z axis in the frame of the laboratory, so that the electric fields can have a polarization either along the X or the Y axis. The transition dipole orientation in the molecular frame is what we want to measure, and from now on, we will use the shorthand notation:

$$\langle XXXX\rangle = \langle \overrightarrow{e}_{LO}.\overrightarrow{\Theta}(R_n)\rangle = \langle (\overrightarrow{e}_X.\overrightarrow{u}_{sig})\,(\overrightarrow{e}_X.\overrightarrow{u}_3)\,(\overrightarrow{e}_X.\overrightarrow{u}_2)\,(\overrightarrow{e}_X.\overrightarrow{u}_1)\rangle \tag{1.20}$$

$$\langle XXYY\rangle = \langle (\overrightarrow{e}_X.\overrightarrow{u}_{sig})\,(\overrightarrow{e}_X.\overrightarrow{u}_3)\,(\overrightarrow{e}_Y.\overrightarrow{u}_2)\,(\overrightarrow{e}_Y.\overrightarrow{u}_1)\rangle \tag{1.21}$$

$$\langle XYXY\rangle = \langle (\overrightarrow{e}_X.\overrightarrow{u}_{sig})\,(\overrightarrow{e}_Y.\overrightarrow{u}_3)\,(\overrightarrow{e}_X.\overrightarrow{u}_2)\,(\overrightarrow{e}_Y.\overrightarrow{u}_1)\rangle$$

$$\langle XYYX\rangle = \langle (\overrightarrow{e}_X.\overrightarrow{u}_{sig})\,(\overrightarrow{e}_Y.\overrightarrow{u}_3)\,(\overrightarrow{e}_Y.\overrightarrow{u}_2)\,(\overrightarrow{e}_X.\overrightarrow{u}_1)\rangle$$

which means in the case of Eq. 1.20 that the probe and the pump fields are all X-polarized, whereas in the case of Eq. 1.21, the probe is X-polarized and the pump is polarized along the Y axis.

The different transition dipole moments orientations in these equations depend on the Feynman pathway for which we want to calculate the orientation dependence. For example in 2D-IR, for a bleach on the diagonal, the same transition dipoles is involved in each of the interactions. When a single transition is considered, it is a good approximation to state that the orientation of the transition dipoles between 0→1 and 1→2 is the same. The next table, adapted from [44], gives the polarization response for the different sequence of polarized pulses, depending on the pathway involved.

Pathway	XXXX	XXYY	XYXY	XYYX
jjjj	1/5	1/15	1/15	1/15
jiji	($4P_2$+5)/45	P_2/15	(5-$4P_2$)/45	P_2/15
jjii	($4P_2$+5)/45	(5-$2P_2$)/45	P_2/15	P_2/15
jiij	($4P_2$+5)/45	P_2/15	P_2/15	(5-$2P_2$)/45

Table 1.1: Orientational response for the different possible pathways involving i or j dipoles, with the sequence of pulses polarized along X or Y. P_2 is the second order polynomial, depending on the angle between the i and j dipoles. ($P_2 = \frac{1}{2}(3cos^2\theta_{ij} - 1)$)

In fact, the field polarizations can be used to modulate the signal arising from the different Feynman pathways. For example, the diagonal peaks of a 2D-IR spectra which involve four time the same dipole in the expression of the orientation dependence will give rise to an absorption change three times higher with parallel probing than in the perpendicular one. This fact can be used to eliminate diagonal peaks from 2D spectra, by doing the subtraction $A_{\parallel} - 3A_{\perp}$ [47].

Also, cross peaks with well defined anisotropy can be eliminated by a proper choice of pulse polarizations [43, 48].

1.2.2 Algebra of the orientational four-point correlation functions

First it is important to note that over all the polarization sequences possible, only three are linearly independent, and related to each other by the equation [49].

$$\langle XXXX\rangle = \langle XXYY\rangle + \langle XYXY\rangle + \langle XYYX\rangle \tag{1.22}$$

Also, in the dipole approximation, all the terms which contains an odd number of a polarization component vanish. (ex:$\langle XXXY\rangle = \langle XYYY\rangle = 0$).(See appendix B).

When one wants to combine pulses with polarizations different than X or Y, but still in the XY plane, it is always possible to express these polarization conditions in function of one of the terms of Eq. 1.22. For example, for a pulse with a linear polarization making an angle α relative to the X axis, we can write its polarization as $X\cos(\alpha) + Y\sin(\alpha)$.

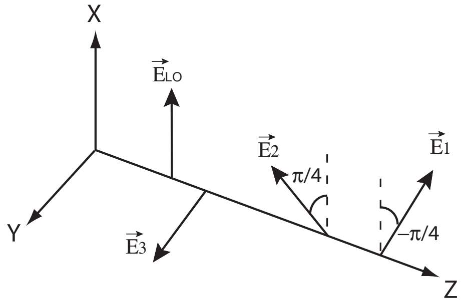

Figure 1.5: Example of a sequence of polarized pulses with their orientation.

For the succession of pulses depicted in Fig. 1.5 , we can re-express the orientational term:

$$\langle\ XY(X\cos(\frac{\pi}{4}) + Y\sin(\frac{\pi}{4}))(X\cos(\frac{\pi}{4}) - Y\sin(\frac{\pi}{4}))\rangle = \frac{1}{2}\langle XY(X+Y)(X-Y) \tag{1.23}$$

$$= \frac{1}{2}(\langle XYXY\rangle - \langle XYYX\rangle) \tag{1.24}$$

Other useful sets of field polarizations can be easily expressed in function of the different tensor elements [47]. Some are depicted in table 1.2.

E_{LO}	E_3	E_2	E_1	Tensor element
0	$\pi/4$	$-\pi/4$	0	$1/2\ (\langle XXYY\rangle + \langle XYXY\rangle)$
$\pi/4$	0	$-\pi/4$	0	$1/2\ (\langle XXYY\rangle + \langle XYYX\rangle)$
$\pi/4$	$-\pi/4$	0	0	$1/2\ (\langle XYYX\rangle + \langle XYXY\rangle)$
0	$\pi/3$	$-\pi/3$	0	$1/4\ (\langle XXXX\rangle - 3\langle XYYX\rangle)$
θ	$-\theta$	$\pi/2$	0	$1/2\ \sin(2\theta)\ (\langle XYXY\rangle - \langle XYYX\rangle)$

Table 1.2: Some useful polarization combination and the tensor elements they can be reduced to.

Chapter 2

Experimental

2.1 Introduction

In this chapter are presented the different apparatus needed to perform ultrafast IR spectroscopy. Commercial femtosecond lasers generate near-IR light pulses that are later frequency-converted to the visible with non-linear crystals or to mid-IR with home-built optical parametric amplifiers (OPA). The different beams are brought to the pump-probe set-up where they interact with the sample, and the spectral changes in the probe are monitored.

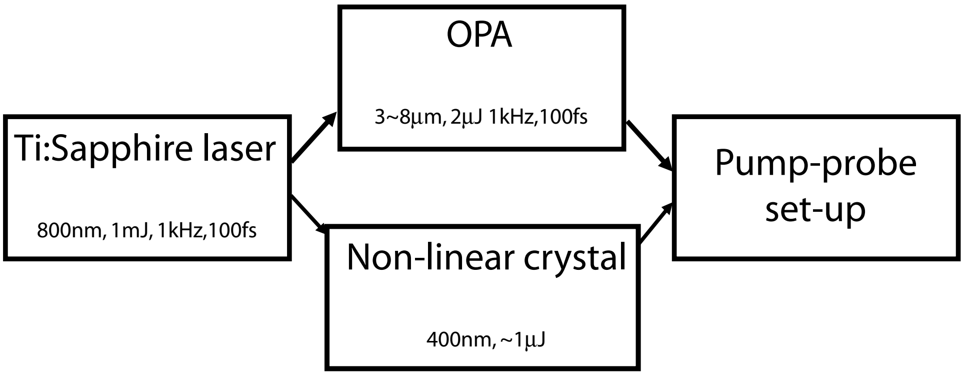

Figure 2.1: General overview of the experimental set-up

2.2 Femtosecond Laser

The femtosecond laser pulses are generated by a commercial laser system from Spectra-Physics. A *Tsunami*® oscillator pumped by a continuus wave *Millenia*® emits 100 fs nanojoule pulses at a repetition rate of 80 MHz,tunable between 775 nm and 840 nm. This pulses are then amplified in the *Spitfire*® chirped pulses amplifier, pumped by the *Evolution*®, leading to pulses of ≈1 mJ at 800 nm at 1 kHz.

2.3 Frequency conversion

2.3.1 UV light generation

The near IR pulses can be converted to near UV by using second harmonic generation in a 1 mm β-Barium Borate (BBO) non-linear crystal cut at 30°. A small fraction of the output from the regenerative amplifier (typically 10 μJ) is focused on the BBO crystal and generates blue light. This results in 390-420nm (depending one oscillator wavelength), 100 fs pulses of a few μJ, that can be used as a pump pulse in the experiment to trigger a photoreaction.

2.3.2 Mid-IR light generation

A two stage OPA, combined with difference frequency generation (DFG) are used to generate mid-IR pulses in the 3 μm to 8 μm spectral range [54, 55]. The general layout is drawn in Fig. 2.2.

The near-IR part of the spectrum from the white light generated in a sapphire plate is overlapped spatially and temporally with a small amount ($\approx$10 μJ) of the fundamental frequency into a BBO (type II, 4 mm) to generate weak signal and idler. The signal is refocused back into the BBO and overlapped with an intense ($\approx$250 μJ) beam to generate intense signal and idler (60 μJ together). Signal and idler are then separated and recombined in a $AgGaS_2$ (type I,1.5 mm) crystal for DFG of mid-IR pulses in the range of 3 to 8 μm. The pulse have a spectral bandwidth of about 200 cm^{-1}, and their central frequency can be tuned by changing the orientation of the BBO and $AgGaS_2$ crystal for best phase matching of the input and output frequencies.

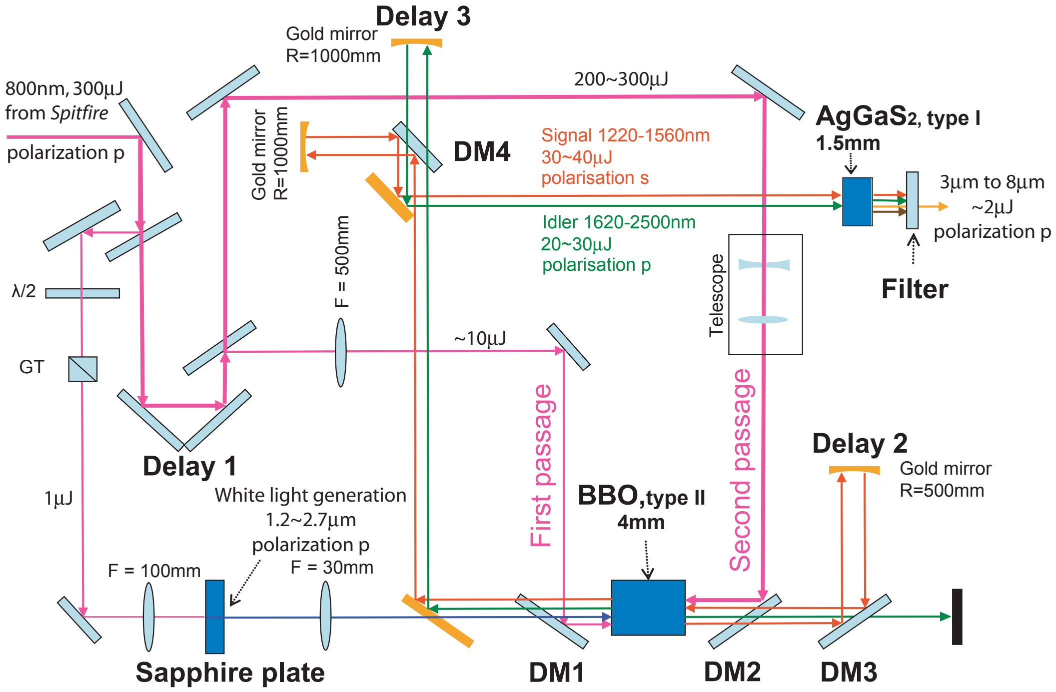

Figure 2.2: Schematic representation of the OPA. DM : dichroic mirrors. R refers to the radius of spherical mirrors. F refers to the focal length of lenses.

2.4 The pump-probe Experiments

2.4.1 UV-IR set-up

In Fig.2.3 is shown a layout of the UV-pump IR-probe set-up used to acquire transient absorption data. The principle is quite simple and was already introduced in chapter 1.

The pump pulse is delayed in a computer controlled delay line that permit to scan the time T between pump and probe pulses. The pump is chopped at half the repetition rate of the probe, i.e. 500Hz, which allows us to measure the intensity of the probe with and without pump alternatively.

A small portion of the energy of the mid-IR pulses coming from the OPA is used as probe light. The waist of the probe beam is first magnified in a telescope, allowing to get a smaller spot size at the sample where it is focused by off-axis parabolic mirrors. The probe beam is split into two, a reference and a signal beam to correct for the laser energy fluctuations. Those two beams propagates together, separated vertically by about 2cm. Both reference and signal are imaged through a spectrometer (Triax Series, Jobin Yvon) on two independent array of an MCT (2×32 pixels, Infrared Asssociates, Inc).

This way, the absorption change can be expressed in function of the intensity of probe and reference on each of the array detectors, when pump is on or blocked by the chopper :

$$\Delta A = -\log\left(\frac{I_{probe}^{pumpoff}}{I_{probe}^{pumpon}} \times \frac{I_{ref}^{pumpon}}{I_{ref}^{pumpoff}}\right) \tag{2.1}$$

This set up has a high detectivity and the noise on the absorbance is usually as low as 20 μOD for an accumulation time of 1 s (1000 shots). Some modifications on this set-up are shown in chapter 6.

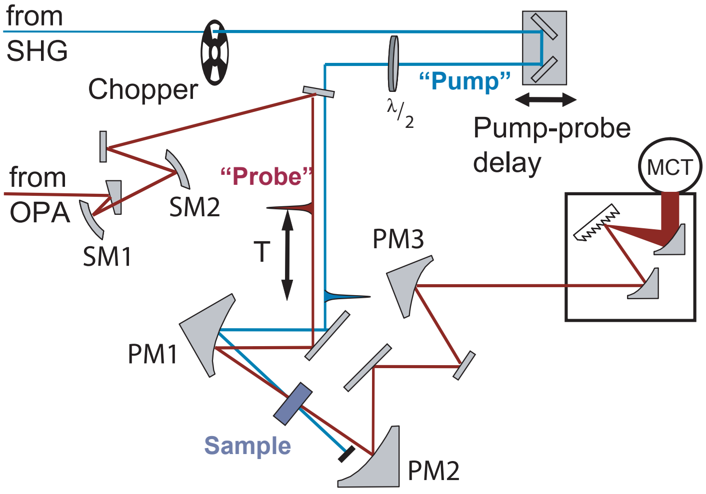

Figure 2.3: Schematic representation of the pump-probe set-up. SM 1 & 2 are spherical mirrors making a telescope. PM 1, 2 & 3 are parabolic mirrors to focus light at sample and on the entrance of the spectrometer. T is the pump-probe delay.

2.4.2 2D-IR set-up

The 2D-IR set-up presented in Fig 2.4 is a recent implementation that is now used intensively in our laboratory. The same set-up as for UV-pump IR-probe spectroscopy is used, only an additional interferometer is placed in the intense IR beam output from the OPA. The complete description of this set-up can be found in [40].

The interferometer creates a pair of collinear pulses, whose path difference t_1 is accurately determined through their interferogram. A He-Ne laser is used to track the position of the moving mirrors in the interferometer, allowing interferometric accuracy. This scheme enables fast scanning of the delay t_1 and minimizes the noise in the 2D spectra, by reducing the effect of the fast energy fluctuation between successive pulses.

The 2D-signals are obtained by Fourier transformation of the light intensity (Eq. 1.9) with respect to t_1. This isolates the oscillating term $Re[E_{sig}.E_{LO}]$ (see Eq. 1.7), making the signal proportional to E_{sig}, while eliminating the unwanted pump probe signals arising from the individual pump pulses. In conventional pump-probe spectroscopy, the light intensity is measured with and without pump beam (chopper) and the log-ratio of the two measurements is taken (Eq. 2.1). The signal is then independent of the spectrum of the probe beam. The same is achieved in our 2D-scans by dividing the signal by the t_1-averaged intensity, and no chopper is needed in that case.

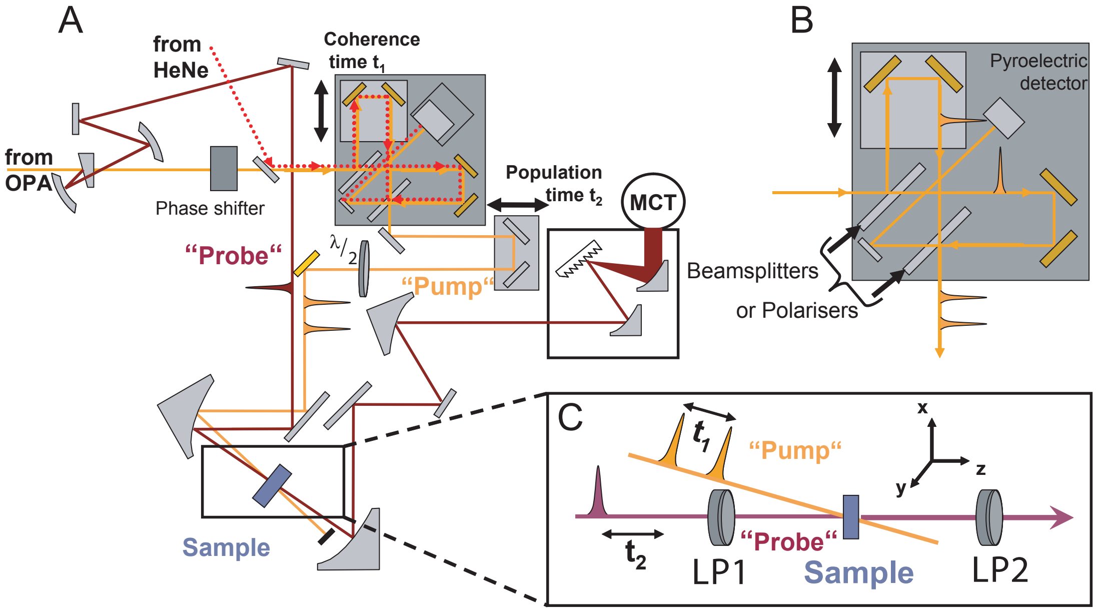

Figure 2.4: Schematic representation of the 2D-IR set-up in the pump-probe geometry. A) General overview B) A zoom on the interferometer to generate the pair of pump pulses. C) A zoom on the implementation for signal enhancement where LP1 and LP2 are nearly crossed polarizers

The spectrometer is usually equipped with broadband beamsplitters, but we can also use polarizers (see Fig.2.4B), in which case the two pump pulses are perpendicularly polarized, allowing to measure new tensor elements of the orientational response function. (see section 1.2.1)

The inset C in Fig.2.4 describes the scheme that was used in this thesis to measure 2D-IR spectra with increased sensitivity (see chapters 5 and 7).

2.4.3 Practical aspects

Photo-Elastic Modulator

In this thesis, we use both waveplates and Photo-Elastic Modulators (PEM) to change the polarization of the pulses. The main interest of PEM is that they can modulate polarization at the repetition rate of the laser, while waveplates have to be rotated between two successive accumulations. This way, two consecutive pulses can have distinct polarization state. The quality of the anisotropy measurement is greatly enhanced this way, as the fluctuations of the laser between the two required measurements (parrallel and perpendicular probing) are correlated (see discussion in section 6.4.3 or reference [29]).

The principle of PEM is the following : a plate of an isotropic material is placed between piezometers which apply a mechanical stress on the plate. Applying a sinusoidal voltage on the piezometers at the resonant frequency of the material, a large birefringence proportional to the strain is induced which can be used to change the polarization state of light.

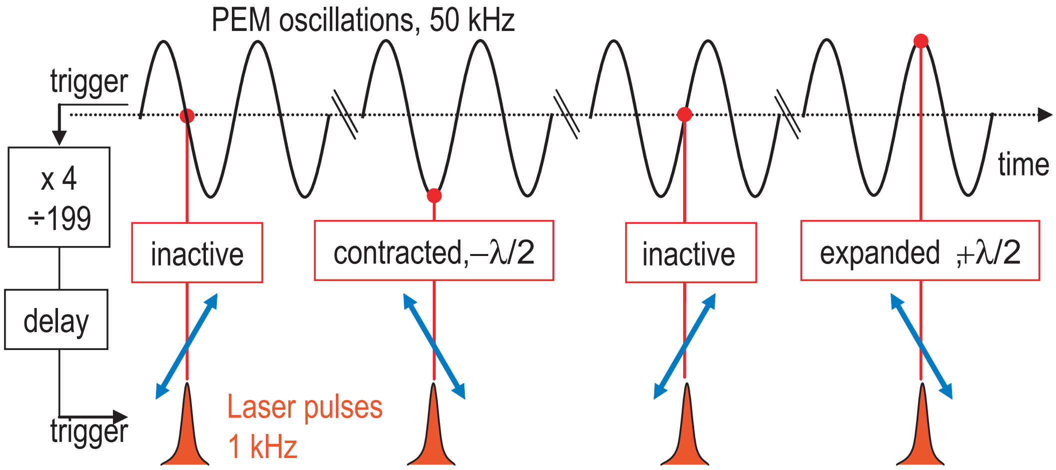

Figure 2.5: Scheme of the PEM state fo four consecutive laser pulses, with their respective polarizations.

The polarization of either the UV-pump or the IR probe (for set-up 2.3) laser pulses could be modulated by different photoelastic modulators. Since our PEMs need to operate at a given resonance frequency $f \approx 50$ kHz, we have synchronized the laser to the PEM, as described in detail elsewhere [56, 57], and shown schematically in Fig. 2.5. In brief, the fourth harmonic of the PEM frequency was down-counted by an odd number to provide a trigger for the laser amplifier of approximately 1 kHz. This trigger was delayed in such a way that the femtosecond pulses cross the modulator when it is in a relaxed state (no polarization change) or at a turning point of its oscillations, i.e. when it acts as a $\pm\lambda/2$ plate. The linear polarization of probe pulses initially at an angle β with respect to the PEM optical axis was thus alternatingly left unchanged or it was rotated to an angle $-\beta$.

The use of a PEM may also have some disadvantages. For example, they need high voltage to activate the piezometers, which results in a electronic noise affecting the signals, dependent on the voltage. One way to reduce this noise was to use a half wave plate in front of the PEM to create a circular polarization. Then, the PEM was tuned with half the voltage to a quarter wave plate, which reduced the electronic noise. Some other artefacts due to PEM are discussed in chapter 6.

Wire grid polarizers

Some of the measurements presented in this thesis rely on the high quality of the polarizers used in the set-ups. We use free standing wire grid polarizer (InfraSpecs , P03 model), with extinction ratio $< 10^{-4}$. These polarizers have a transmission of only 50%, which is a drawback in our case, as we need as much energy as possible at the sample to increase the signal.
An alternative which was not used in this thesis, is to use brewster angle polarizer made of germanium, which can in principle have extinction ratio $< 10^{-7}$ [51].

Part II

Study of biomimetic photoswitches

Nature has created fascinating devices for the interconversion of chemical and mechanical energy, where *cis/trans* isomerization (CTI) plays an important role [58]. This includes the process of vision [17], protein folding and unfolding [59], gating of ion channels [60] or even cellular dynamics [61].

The retinal protonated Schiff base chromophores of Rhodopsin proteins are a class of biological photoreceptors which constitute natural E/Z switches [1]. In the protein, these molecules undergo bond-selective and efficient photo isomerization, which lead to the conformational changes in the protein framework that trigger the vision process [17,18]. The selective 11-cis to all-trans isomerization of retinal in rhodopsin occurs around the C11=C12 double bond, and is achieved with the record value of 200 fs . It is the most efficient isomerization known, with a reaction quantum yield of 0.67 [18,21] . Retinal can be regarded as a model in terms of quantum yield, rate and unidirectionality for building artificial light-driven molecular switches [62–64].

Based on these observations, a new class of molecular switches based on a N-alkylated indanylidene-pyrroline Schiff base(NAIP) framework was proposed, with the aim to mimic the photochemistry of retinal in Rhodopsin.

Initially designed on computer, the NAIP-framework features a well-isolated singlet excited state characterized by significant charge transfer from the pyrroline to the indanylidene moiety (see Introduction). Combined Quantum Mechanics/Molecular Mechanics (QM/MM) computations [28] have shown that the molecule relaxes from the Frank-Condon region in the first excited state to the ground state by passing through a conical intersection (CI) on a barrierless reaction path. This leads to an efficient and fast isomerization process very similar to that of the biological chromophore retinal on which it was modelled [65–67]. The theoretical predictions are in very good agreement with experiments, probing the complete photocycle of a prototype methoxylated NAIP molecule (MeO-NAIP) by time-resolved electronic and vibrational spectroscopy [27,28].

In chapter 3 are presented the results from ultrafast infrared spectroscopy on zwitterion photoswitch of the NAIP family (ZW-NAIP). The ultrafast spectroscopy of the ZW-NAIP photoswitch and its new properties make it attractive for the design of unidirectional molecular rotors fuelled by light. In fact, its chiral framework is expected to induce unidirectional rotation during the *cis* to *trans* and *trans* to *cis* isomerization processes. The consequence of unidirectional rotation on the signals, and the possibility to detect it from the anisotropy of transient IR spectroscopy measurements is explained in chapter 4 and was the motivation for the experimental development described in part III of this thesis.

---

[1] Z and E refer to the *cis* and *trans* configuration respectively

Chapter 3

Ultrafast spectroscopy of the bi-directional isomerization of a dipolar biomimetic photoswitch

The work presented in this chapter reports on time-resolved infrared data characterizing a zwitterionic switch (ZW-NAIP, see Fig. 3.1) based on the NAIP scheme presented in the introduction of this thesis [27, 63]. ZW-NAIP exhibits remarkable new properties [26]. A negatively charged carboxylate group at the C2-position of the pyrroline moiety acts as an internal counterion , creating a permanent dipole moment of approximately 15 Debye in methanol solution. In the molecular frame, the predicted dipole change is almost 30 Debye between Z and E isomers (See Fig. 3.1), which is significantly larger than any photo-induced dipole change observed so far (e.g. 17 D for indolinospyrobenzopyrane [68]). The carboxylate group will, in the future, serve as a linkage to peptides, where the new switch may provide an interesting alternative to the widely-used azobenzene-based chromophores [69], for example by greatly enhancing the solubility of apolar sequences in aqueous solvents. Moreover, unlike the previously investigated switches, ZW-NAIP is a chiral molecule (although the experiments reported here were performed on a racemic mixture) and constitutes a first step toward a switch with directional preference for the isomerization of two enantiomers [63, 70–72].

Our mid-IR results are complementary to UV-visible transient absorption and time-resolved fluorescence measurements on ZW-NAIP, which are reported in the article we published with our collaborators [73]. Some of these results will be mentioned here to support our discussion. While vibrational spectroscopy is highly sensitive to the return of population to the electronic ground state and can more easily distinguish the two isomers, electronic spectroscopy provides a detailed picture of the wavepacket-like behaviour in the S1 excited state, with evidence for an impulsive passage through a conical intersection.

3.1 Experimental set-up

We used here the UV-pump IR-probe set-up described earlier in section 2.4.1. The pump pulses at 390 nm had energy of 0.5 μJ.

Data in three overlapping spectral windows were recorded consecutively under identical conditions and assembled to produce transient spectra between 1475-1675 cm^{-1}, with a 4 cm^{-1} resolution.

Zwitterionic N-alkylated indanylidene-pyrroline (ZW-NAIP) was synthesized by our collaborators in Italy, in racemic mixture as described in reference [26]. It was dissolved at a concentration of 20 mM in 1 ml deuterated methanol dried over molecular sieves. The sample was circulated with a peristaltic pump in a 100 μm thick flow cell made of two 2 mm CaF_2 windows [74]. The maximum optical density in the mid-IR was 130 mOD at 1630 cm^{-1}. Sam-

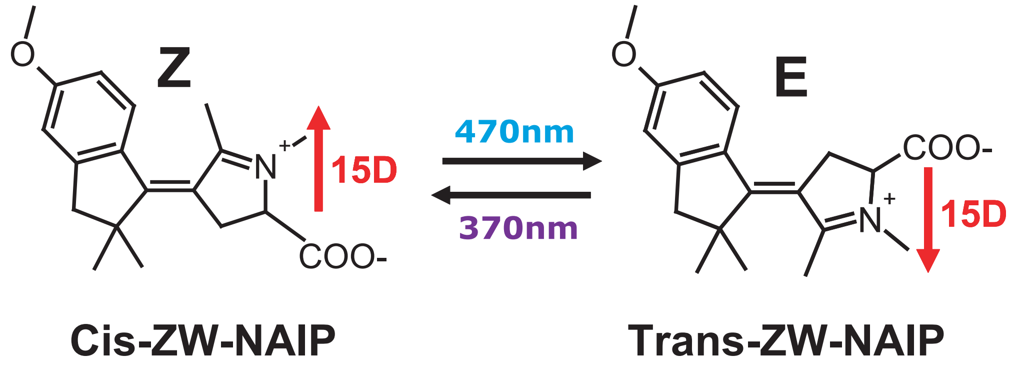

Figure 3.1: The isomerization of ZW-NAIP induces a 15D dipole change in the molecular frame.

ple purity and isomer concentrations were checked shortly before and after measurements by recording ^{1}H-NMR spectra on a 300 MHz spectrometer (Bruker). FTIR data was recorded at 2 cm^{-1} resolution on a BioRad FTS-175 Fourier transform spectrometer.

3.2 Results

3.2.1 Steady State measurements

In the dark at room temperature ZW-NAIP is found almost entirely in the Z conformation. Irradiation of the sample in the UV-visible leads to the formation of molecules in the metastable E form, which relax back to Z only very slowly with a 6.5 h time constant [62] . ^{1}H-NMR spectra could thus be recorded to determine the exact isomer concentrations in the irradiated samples, yielding the infrared absorption spectra of both isomers (Fig. 3.2).

The FTIR spectrum of ZW-NAIP in methanol (Fig.3.2) shows four bands in our spectral window between 1475 cm^{-1} and 1675 cm^{-1} , which can be compared with harmonic normal mode calculations (Gaussian program suite [75] , B3LYP with 6-31G+ basis set). The small band near 1490 cm^{-1} is due to CH_3 bending modes. The band at 1570 cm^{-1} (1563 cm^{-1} for the E-isomer) is assigned to a stretching mode dominated by in-phase contraction of the isomerizing C1'-C4 double bond and the C5-N bond of the pyrroline moiety. The corresponding transition dipole moment is expected to be nearly parallel to the C1'-C4 bond and the electronic transition dipole moment, consistent with an anisotropy in the pump-probe data close to 0.4 (ratio of 3 between parallel and perpendicular probing, see Fig. 3.3).

Two normal modes involve strong asymmetric C=O stretching motion of the negatively charged carboxylate group (as well as out of phase C1'-C4 and C5=N stretch). One of them can be assigned to the 1626 cm^{-1} band, based on its slightly negative anisotropy in the pump-probe data and a predicted transition dipole moment nearly perpendicular to the C1'-C4 bond. The second mode involving C=O stretch may either not be resolved or give rise to the shoulder at 1608 cm^{-1} . This shoulder could, however also be due to another mode that is predicted to carry oscillator strength, which is characterized by deformation of the 6-membered ring (equally involving some out of phase C1'-C4 and C5-N stretch motion).

After a few minutes of continuous irradiation at 470nm (light-emitting diode 70 mW), a wavelength at which the Z-isomers absorb 2-3 times stronger than the E-isomers, it was possible to reach a photoequilibrium with a relative E concentration of 80% (Fig. 3.2c). Subsequent

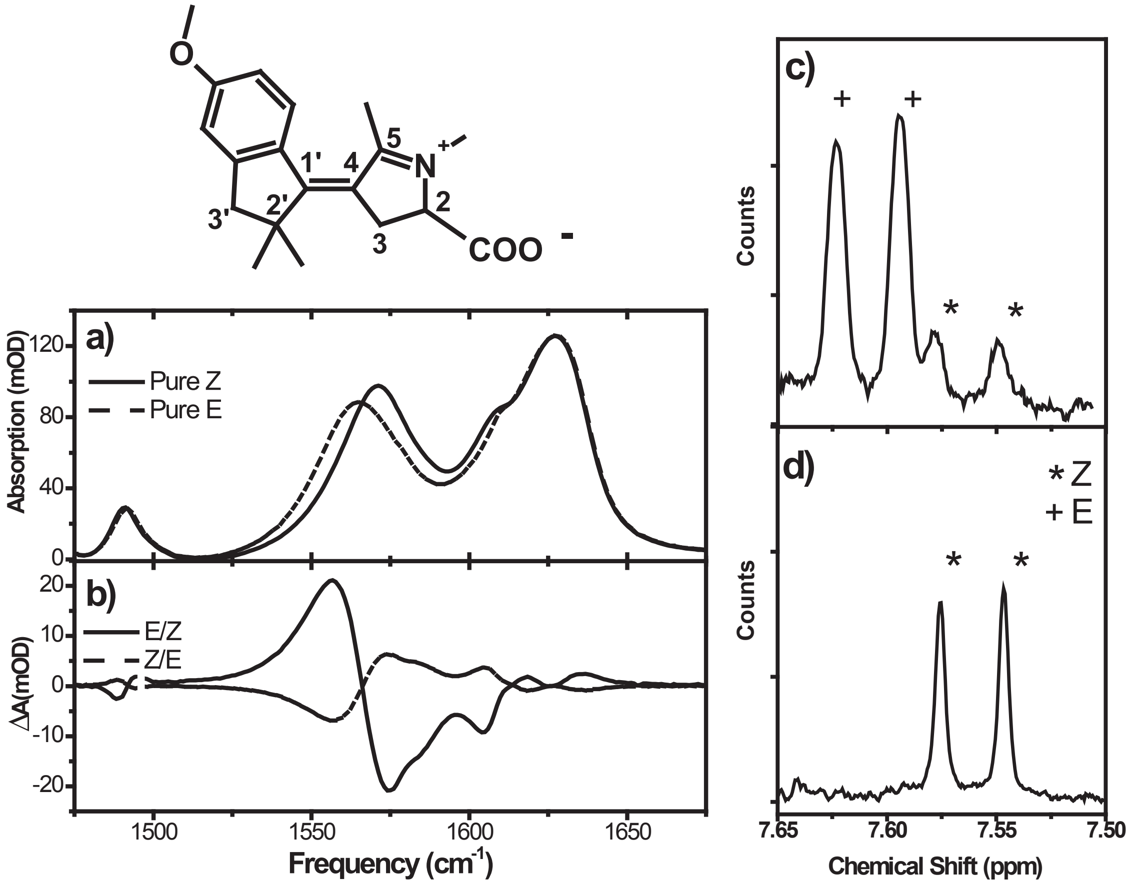

Figure 3.2: Structure and a) vibrational spectrum of the Z and E isomers of ZW-NAIP. b) Absorption changes after irradiation of Z at 470 nm (solid line) and irradiation of an E-enriched sample at 370 nm (dashed line). c) ^{1}H-NMR spectra show that the switch can be prepared with an E-concentration of 80% after irradiation at 470 nm. d) ^{1}H-NMR spectra obtained with a pure Z conformation of the sample when left in the dark

irradiation at 370 nm partially reversed the changes in the FTIR spectra observed for Z→E isomerization (Fig. 3.2b). This and the transient experiments performed on this E-enriched sample (see results below), demonstrates that ZW-NAIP can be efficiently used as a reversible bi-directional dipolar switch.

The isomer concentrations in photoequilibrium for irradiation at the isosbestic point (equal E and Z absorption) at 412 nm (unfocused fs-laser beam, average power 50 mW) was found to be 40% Z and 60% E, indicating that the quantum yield of the Z→ E photo isomerization is 1.5 higher than in the E→Z direction. (Lower E concentrations reported in [26] are most likely due to thermal relaxation ($k_R \approx 6.5$ h) during longer irradiation with weaker light sources, competing with the isomerization process).

3.2.2 Mid-IR Time-resolved Spectroscopy

Z → E isomerization

Immediately after 390 nm excitation of a sample containing only Z-isomers, the transient spectrum (Fig 3.5a, 0.25 ps) is dominated by the bleaching of the 1570 cm^{-1} and 1630 cm^{-1} ground state absorption bands of ZW-NAIP. Comparison with the inverted FTIR spectrum (dashed line) reveals that between 1590 cm^{-1} and 1620 cm^{-1} bleaching is weaker or partially compensated by induced absorption. (An additional, unstructured and fast-decaying offset due to the

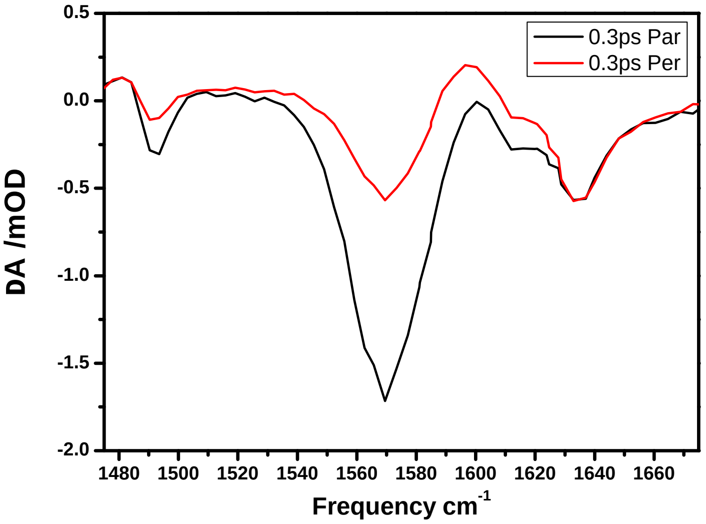

Figure 3.3: Background-corrected pump-probe data for Z-excitation at 300 fs delay for parallel and perpendicular polarization of UV-pump and IR-probe pulses. Anisotropy at 1570 cm^{-1} (C=C stretch) is in line with nearly parallel electronic and vibrational dipoles while dipole due to C=Os stretch at 1620 cm^{-1} makes an angle around 55° the electronic dipole.

Kerr signal of the cell windows has been subtracted).

Between 0.2 ps and 1 ps delays, an induced absorption signal is growing at the low frequency side of the C=C stretch band. After 1 ps, its maximum is continuously shifting to higher wavenumbers, increasing the overlap of this induced band with the initial bleach. This leads to a decrease of the total signal in the C=C stretch region on a time scale of approximately 10 ps. After 20 ps the transient spectrum already very closely resembles the steady-state E-Z difference spectrum.

We integrated the signal over the transient spectra between 1505 and 1590 cm^{-1} in order to extract a time constant of this growing absorption band. The time trace shown in Fig. 3.5e (open circles) can be fitted by a single exponential with a 200 fs rise time. We will argue below that the ultrafast rise of this signal corresponds to the recovery of the double bond character in the electronic ground state of both Z and E isomers after internal conversion (IC). The essentially constant integrated signal at delays longer than 1 ps indicates that, on the picosecond timescale, the photo-induced absorption band is merely shifting and narrowing as the molecules dissipate excess energy to the solvent.

The measured transient IR spectra in Fig. 3.5a are difference spectra, composed of the absorption of the molecules after excitation minus their absorption before excitation. The latter contribution can be eliminated by subtracting a properly scaled FTIR spectrum (dashed line in Fig. 3.5a). This yields to the "true" absorption spectra of ZW-NAIP molecules from the moment of excitation up to the completion of the photoreaction; these spectra are shown in Fig. 3.5c and d. Growth and shifts of the vibrational bands can now be directly observed:

- The band at 1630 cm^{-1} can be seen to weaken and to undergo an immediate red-shift upon photoexcitation, leading to induced absorption that partially compensates the bleaching of the equally red-shifted 1608 cm^{-1} transition. Fast spectral changes on a sub-picosecond timescale comprise a decay of this red shift and a slight broadening of the C=O stretch band, which give rise to the positive absorption signal near 1650 cm^{-1} in the transient

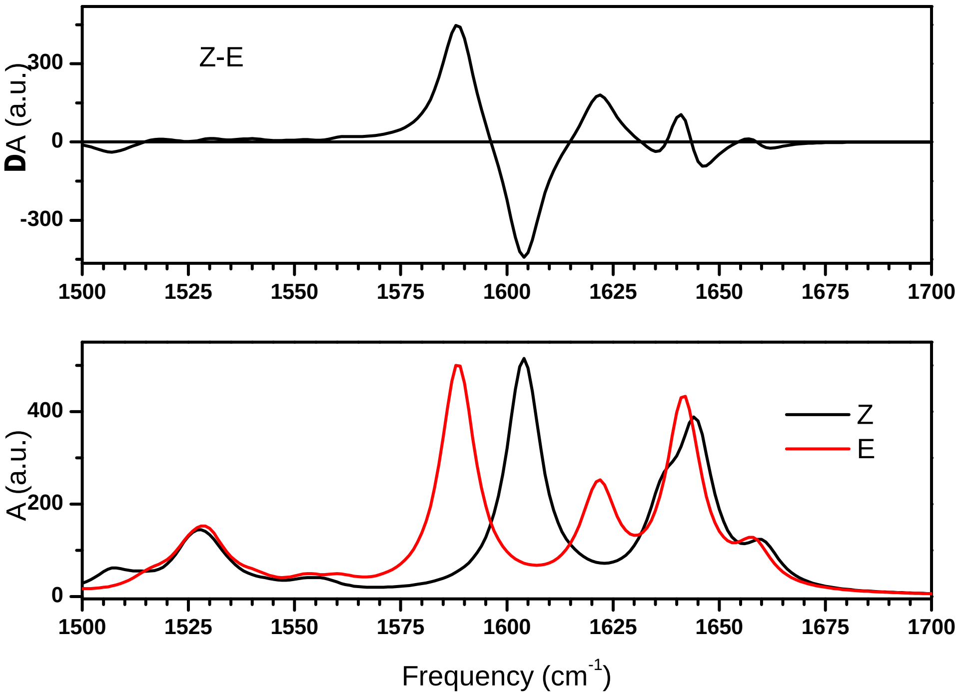

Figure 3.4: Harmonic normal mode specta of Z and E forms of the ZW-NAIP switch in the gas phase (B3LPY, 6-31G+ basis set). The mode at 1605 cm^{-1} (1586 cm^{-1} for E) is dominated by C1'-C4 and C=N stretch motion, the two modes near 1640 cm^{-1} (1620 and 1640 cm^{-1} for E) are characterized by asymmetric C=O stretch motion. In the gas phase optimized structure, the carboxylate group is rotated with respect to the QM/MM solution structure of [26].

data of Fig. 3.5a. Unlike the C=C stretch mode (1570 cm^{-1}) whose integrated intensity remains constant after 2 ps, the 1630 cm^{-1} band continues to grow on a picosecond timescale. (Solid line in Fig. 3.5 e)

- The band associated with the C=C stretch vibration is weak at early times, and grows back during the first picosecond as seen in Fig. 3.5c. The growth of this band is depicted by the integral in Fig. 3.5e (circles) and takes place with a 200 fs time constant. While its integral stays constant after 2 ps, the band shifts on the picosecond time scale (Fig. 3.5d), until the spectra matches that of the fully relaxed ground state.

E → Z isomerization

The reverse E→Z photo-isomerization was investigated after establishing an E-isomer concentration of 80% in a photoequilibrium maintained by continuous irradiation of the sample at 470 nm. A higher absorption cross section for E at the pump-laser wavelength (390 nm) ensured that only 10 to 15% of the excited molecules were initially in the Z form.

The results are depicted in Fig. 3.6. The spectral changes at short delay times are very similar to those observed for Z excitation. Bleaching is again strongest for the C=C stretch band, with a red-shifted induced absorption band forming within the first picosecond. Spectral

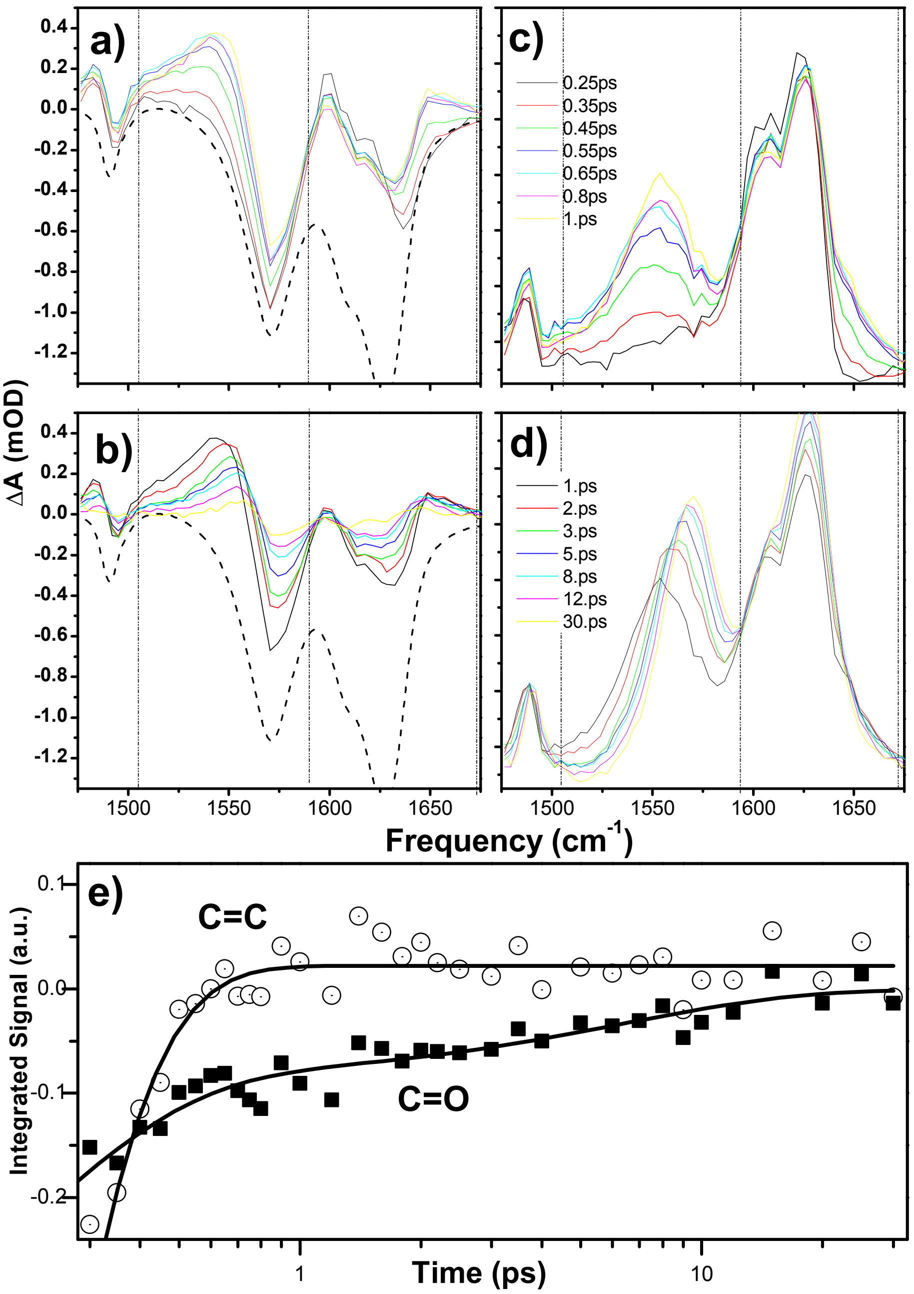

Figure 3.5: a) and b) Transient absorption spectra at different delays after excitation at 390 nm of a sample containing only Z isomers. Pump energy 0.3 J, time resolution (cross correlation) 150 fs FWHM. Dashed line: inverted FTIR absorption spectrum. c) and d) Same data as after substraction of the inverted absorption spectrum, which eliminates the bleaching component. Pump-probe delay times are given in picoseconds e) Integral of the transient spectra in a and b between vertical dashed lines at 1505 cm^{-1} and 1590 cm^{-1} (C=C stretch band, open circles) and between vertical dash lines at 1590 cm^{-1} and 1675 cm^{-1} (C=O stretch bands, solid squares). Solid lines represent mono-exponential (200 fs) and bi-exponential (200 fs and 5.5 ps) fits, respectively.

integration between 1505 and 1590 cm^{-1} produces an exponentially rising signal with a time-constant (a least square fit yields 250 fs) similar to that found in the Z→E direction (Fig. 3.6e). This integrated signal stays constant for delays larger than 2 ps (Fig. 3.6e). Again, the shift and growth affecting the C=O band occur both on the picosecond time scale (Fig. 3.6e)

Quantum yield of isomerization

Figure 3.7 presents the comparison between FTIR spectra and time-resolved spectra obtained for both Z→E and E→Z photoisomerization processes in order to determine quantum yields of isomerization. For this purpose, the time resolved spectra were intensively accumulated for only 2 delays, i.e. 300 fs where the bleach spectrum can be compared with the inverted FTIR spectra of the photo-excited isomer, and at 300 ps where the spectrum matches the difference spectrum obtained under irradiation in FTIR. The noise was low enough to reveal absorption changes smaller than 10 μOD.

By fitting the FTIR absorption spectrum to the 1570 cm^{-1} bleach signal in the early delay pump-probe spectra of Z-ZW-NAIP (Fig. 3.7)a, we calculate the number of molecules which have actually absorbed a photon. Matching the FTIR-difference and transient signal at 300 ps delay allows us to deduce the ratio of each isomer in solution. We find then a 35% quantum efficiency for Z→E isomerization. This must be regarded as an upper limit because unlike the previously studied parent molecule NAIP (no carboxylate group), where the C=C stretch band was spectrally well-isolated [28], the transient spectra immediately after photoexcitation is not an exact replica of the (inverted) absorption. The additional modes in ZW-NAIP do not disappear in the excited state but broaden, shift in frequency and change oscillator strength, which may partially reduce the C=C bleach and thus increase the calculated quantum efficiency as we may under estimate the number of excited molecules.

Following the same analysis, the upper limit for the quantum efficiency of the E→Z reaction is found to be 22 %, and the bleach spectrum subtracted in Fig. 3.6 c and d corresponds to this calculated yield. This E→Z quantum efficiency is 0.6 times the Z→E quantum efficiency, in line with the photoequilibrium concentration ratio under irradiation at the isosbestic point. We also used this ratio in order to include in the E→Z quantum efficiency calculations the contribution of the molecules (≈10-15%) that were excited in the Z-form.

Thermal contribution and photodegradation We noticed a change in the transient spectra when the pump-pulse energy was raised above 0.5 μJ (corresponding to approximately 2×10^{10} W/cm2 in the focal spot), in which case the difference spectrum at long delays (30-300 ps) no longer matches the FTIR data, with an additional bleach contribution appearing in the C=O stretch region. Prolonged irradiation under these conditions also led to changes in the FTIR and NMR spectrum of the sample. Multiphoton excitation in very strong laser fields can thus lead to photodegradation of ZW-NAIP. On the other hand, only very small changes in sample absorption (due to the heating of the methanol solvent) were observed in the spectral window under investigation when the temperature was raised from 22 to 24 Celsius degrees (see Fig. 3.8). The contribution of temperature to the transient spectra due to the (sub Kelvin) temperature increase in the irradiated sample volume can thus be neglected.

Computational results

Our collaborators from Italy, in the group of Prof. Olivucci, have studied ZW-NAIP with quantum mechanics/molecular mechanics (QM/MM) computations. They could show that the excited state properties of ZW-NAIP were similar to the previously studied MeO-NAIP photoswitch [26,28] and to that of Rhodopsin. A result from this computational work is shown in Fig. 3.9. They could show that the excited states of the *cis* and *trans* isomers display a smooth barrierless path form the Franck-Condon until a conical intersection (CI) with the ground state. This is a prediction that the take place on the sub-picosecond time scale, and in both $Z \rightarrow E$ and $E \rightarrow Z$ directions. They predicted barrierless torsional motion about

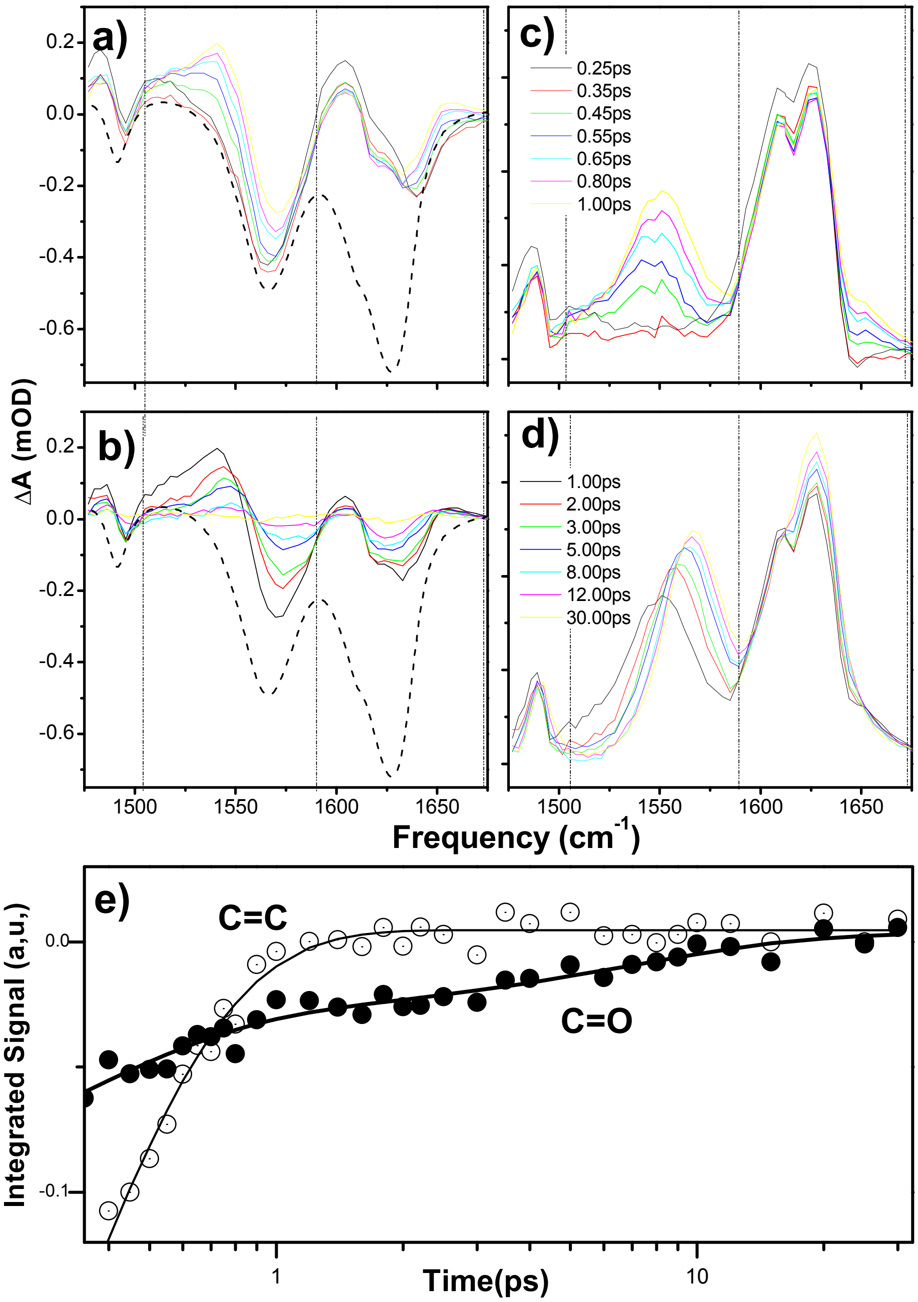

Figure 3.6: a) and b) Transient absorption spectra at different delays after excitation at 390 nm of a sample with an E isomer concentration of 80%. Data was recorded under identical conditions as in Fig.3.5 as soon as photoequilibrium was established by 470 nm irradiation. Dashed line: inverted FTIR absorption spectrum (85% E, 15% Z). c) and d) Same data after subtraction of the inverted absorption spectrum, which eliminates the bleaching component. Pump-probe delay times are given in picoseconds e) Integral of the transient spectra shown in a and b between vertical dashed lines at 1505 cm^{-1} and 1590 cm^{-1} (C=C stretch band, open circles) and between vertical dash lines at 1590 cm^{-1} and 1675 cm^{-1} (C=O stretch bands, solid squares). Solid lines represent mono-exponential (250 fs) and bi-exponential (250 fs and 4 ps) fits, respectively.

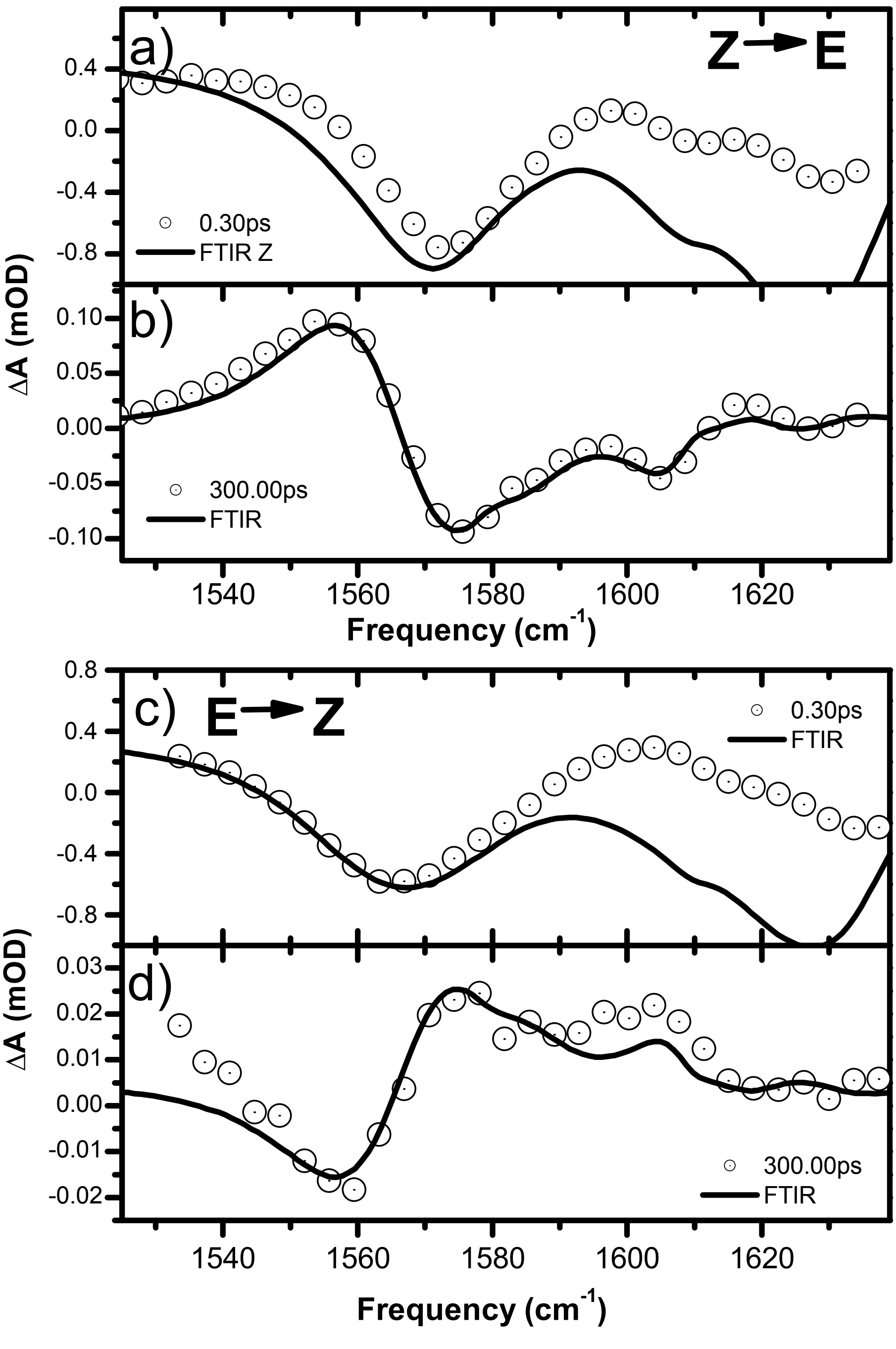

Figure 3.7: a) and c) Comparison between bleaching at early times (0.3 ps) and FTIR spectrum of ZW-NAIP for both Z→E and E→Z isomerization process. b) and d) comparison of the later times (300 ps) and FTIR difference spectra obtained under irradiation.

the C1'-C4 bond and loss of its double bond character [26] in the excited state. Trajectory simulations on the excited state potential estimated the time scale of isomerization to be on

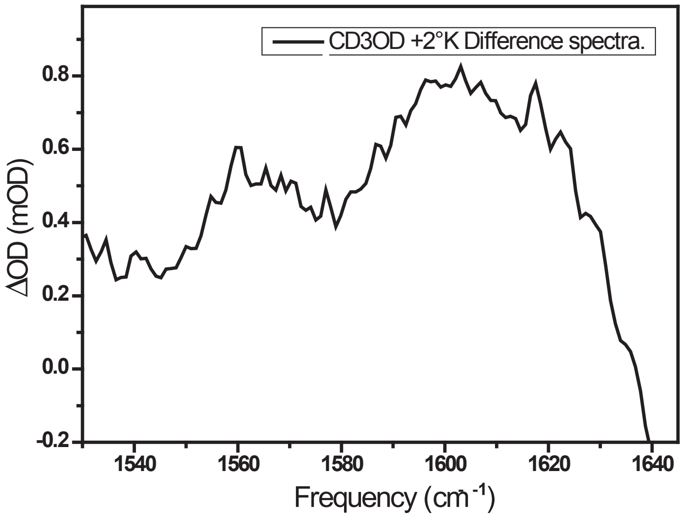

Figure 3.8: Difference spectra obtained after 2K increase of temperature corresponds to a shift of 0.8 mOD at 1600 cm^{-1}.A temperature increase <0.05° could explain the 10 μOD difference between FTIR and long delays time resolved spectra consistent with a 0.5 μJ deposited in the focal volume.

the order of 300 fs.

Results from ultrafast UV/VIS spectroscopy

Briand et al., who investigated the photoreaction in the Z→E direction by ultrafast UV-visible spectroscopy observed an ultrafast fluorescence decay with a 140 fs time constant, and a broad excited state absorption undergoing a strong spectral shift on a 200 fs timescale [73]. Its longest-lived component near 300 nm decays with a 160 fs time constant. An induced absorption that is red-shifted with respect to the ground state S1-absorption band is attributed to hot molecules in the electronic ground state. It rises with a 200 fs delay and reaches its maximum 380 fs after photoexcitation. Those experiments thus provide clear evidence for ultrafast excited state decay, in line with our results discussed below.

3.3 Discussion

From our transient infrared spectra, the most prominent signal for both Z and E excitation is the instantaneous bleach and re-formation, on a sub-picosecond timescale, of the band associated with the C=C stretch vibration. The bleaching is consistent with ab initio minimum energy path calculations in the electronically excited state, The re-formation of the vibrational band in this spectral region is thus interpreted as a signature for the return of photo-excited molecules into the electronic ground state, as previously observed for the NAIP parent molecule [76]. Our signal in the C=C stretch region is also similar to data recorded for the chromophore of Bacteriorhodopsin [77,78]. However, due to longer pulse durations and, more importantly, perturbed free induction decay (PFID) signals at negative pump-probe delay and a Kerr-signal from the sample cell windows, our mid-IR experiment cannot unambiguously distinguish between an instantaneous or a delayed onset of ground state population. Nevertheless, the 250 fs spectrum in Fig. 3.5a and c, which is the first one free of PFID and Kerr-signal contributions, shows only a very small positive C=C stretch band.

While the C=C stretch signal is growing in, it is continuously narrowing and the band center is shifting toward higher frequencies. In such a case, only the integrated band intensity

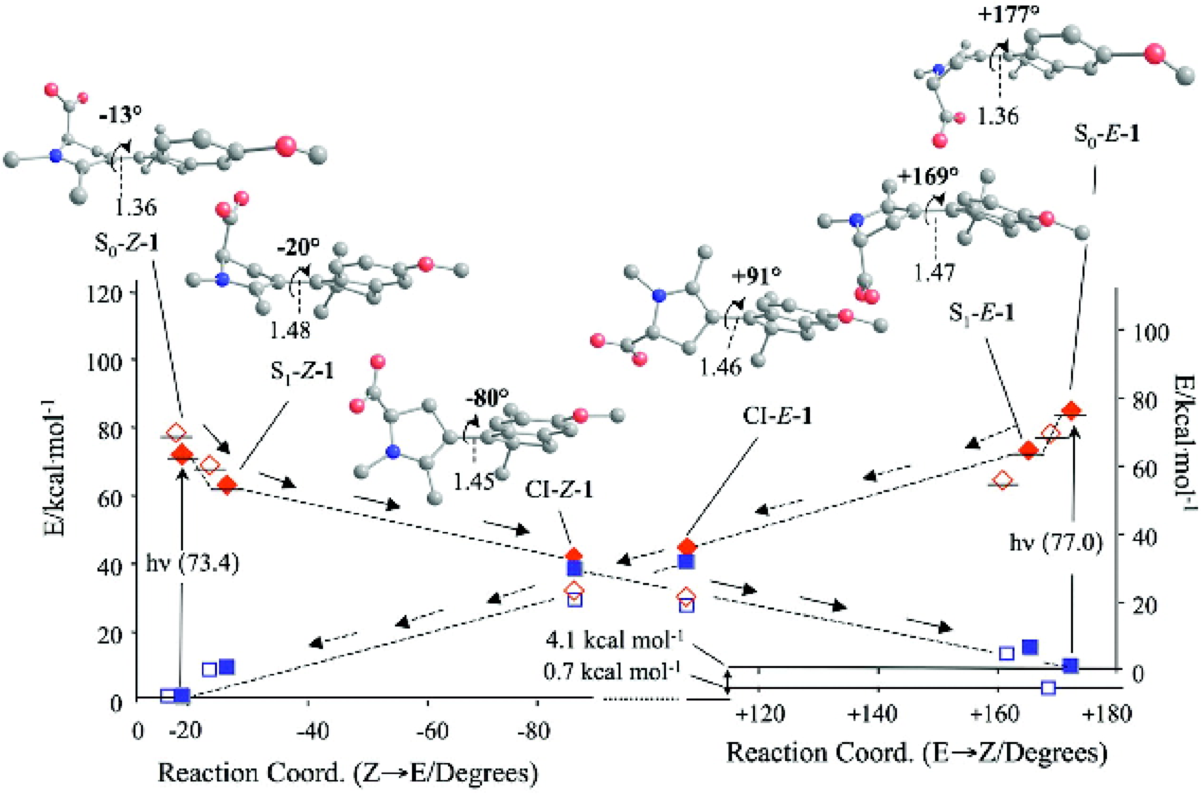

Figure 3.9: The Minimum Energy Path calculations for Z→E and E→Z isomerizations. The arrows indicate the motion to the conical intersection and back to the ground state to either Z or E isomer

yields a meaningful measure of the underlying population dynamics, whereas the time traces at individual probe frequencies can only be fitted using multiple time constants. Nevertheless, the numbers extracted from the fits of the integrated spectra in Fig. 3.5e and 3.6.e still carry large error bars, as they are sensitive to band overlap and to the decay of the cell window signal.

In the transient spectra shown in Fig. 3.5 and 3.6 the red-shift of both Z and E photoproduct bands due to anharmonic coupling to low-frequency vibrations, does not allow us to distinguish isomerizing molecules from those returning to the initial Z or E conformation until the end of vibrational cooling approximately 10 ps after excitation. Due to a similar shift of the visible spectrum of vibrationally hot molecules, an electronic transient signal resembling the static Z-E difference spectrum could also only be observed after 10 ps [73]. The high quantum yield and the existence of a conical intersection with a twisted geometry argue for an isomerization occurring at the moment of the recovery of the ground state during the first picosecond, when the C1'-C4 double bond is restored. The isomerization time is then determine from the fits in Fig. 3.5e) and 3.6, which gives 200 fs and 250 fs for the Z→E and E→Z isomerization processes respectively.

The strong initial red-shift of the C=C stretch band immediately after electronic decay is due to excited low-frequency vibrational modes that are populated in the hot molecules after electronic decay. These are coupled anharmonically to the observed high frequency vibrational transitions and typically shift them to lower energy [79]. As the excess energy is dissipated to the solvent, the high frequency modes gradually recover the spectral position and lineshape characteristic of the cold molecules in the electronic ground sate.

Unlike the C=C stretch signal, the vibrational bands associated with C=O stretch vibration do not disappear in the electronically excited state but shift in frequency and change oscillator strength. This is likely to be caused by a change in normal mode character (in the electronic ground state all vibrational modes in this spectral window contain C=C and C=N stretch motion) and by the important charge redistribution. The oscillator strength of the highest frequency mode continues to grow during the cooling phase of the photoreaction with a 4-6 ps time constant. We interpret this change as a signature of solvation of the large permanent dipole due to rearrangement of the solvent structure.

The quantum efficiencies obtained are greater than the value found from kinetic measurements using HPLC analysis [26], which have recently yielded to a value of 19% for $Z \to E$ process. A source of error in the present measurements is the exact E/Z concentration ratio obtained from ^{1}H-NMR spectra and used to determine the pure E spectra. Also the number of photoexcited molecule we guess from the intensity of the bleach signal may be under estimated here due to the positive C=O band contribution on excited state.

3.4 Conclusion

We have demonstrated the functioning of a zwitterionic molecule with a rotating 15 D dipole moment as an ultrafast bi-directional photoswitch. Despite strongly overlapping electronic absorption spectra it is easily possible to prepare samples with an excess of either isomer of more than 80 %. The NAIP based switch thus combines the favorable photophysical properties of widely used non-polar switches like azobenzene with high solubility in polar solvents and mechanical control over a large dipole moment, which rotates by nearly 180 $\circ$ in the molecular frame upon isomerization.

In line with time-resolved UV-visible spectroscopy, transient vibrational spectra show signatures of a very short-lived electronically excited state, where the C=O stretch vibration of the carboxylate group is shifted and looses oscillator strength. The C=C stretch vibration of the isomerizing bond reports on the return of the excited population into the electronic ground state on a 200-300 fs timescale.

Small shifts and intensity changes of the C=O stretch mode are observed until 30 ps after excitation, when the solvation of the highly polar carboxylate group is complete. The reversal of the strong static dipole moment of ZW-NAIP may thus be fully controlled by light on an ultrafast timescale. This group keeps its local character even on excited state, making it an interesting probe of the structure change if we consider the anisotropy of the associated absorbing band.

Bi-directionality, rates and quantum yields of Z→E and E→Z isomerization give ZW-NAIP potential properties for one who wants to convert light into mechanical motion. The chiral framework of ZW-NAIP should involve a unidirectional isomerization [80–82], and constitutes an important step forward for application of ZW-NAIP as a rotor fuelled by light and the design of machines at the molecular level [83, 84]. The possibility to detect the unidirectional motion of ZW-NAIP with ultrafast IR spectroscopy is the topic of chapter 4.

Chapter 4

Outlook : Towards the real time detection of unidirectional rotation

4.1 Introduction

Nature provided already many examples of molecular machines like the linear motor myosin [85], which is responsible for muscle contraction or the ATP synthase, a rotating motor that catalyses the formation of ATP [86]. Retinal itself can be considered as a rotational motor [87], and the effect of rotation is the first step of phototransduction.

The light driven motors derived from overcrowded alkenes proposed in the group of Prof. Feringa in the University of Groningen already achieved the goal of unidirectional motion, but a thermal step is still needed between the two successive photo-isomerizations, slowing down the full cycle rotation of the motor [88, 89].

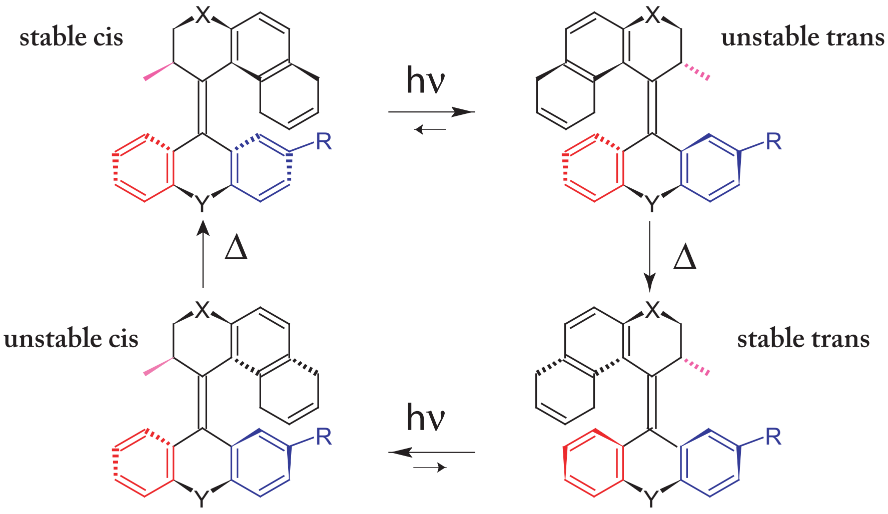

Figure 4.1: The four step rotatory cycle of Feringa's molecular motors. Two steps are photo-induced (hν) and two steps are thermal (Δ)

The rotating part of these motors are connected to a "stator" with a C=C bond, which acts as the axle of the rotor (See Fig. 4.1). The cis-trans isomerization steps are photoinduced, while there are two thermal helix inversion. These thermal steps require the crossing of a potential energy barrier, which is unidirectional and driven by a favourable difference in free energy due to a stereogenic center [88] (purple on the figure).

By varying the stereogenic substituent, as well as the X, Y and R groups, the rate and quantum yields can be optimized, the important factor being the length of the isomerizing C=C bond, the size of the rotor, and its steric hindrance with the stator [90].

With this, megahertz rotational frequency has been demonstrated on these compounds [91]. The unidirectionality in this case can be demonstrated using circular dichroism spectroscopy of the four intermediate state involved in the full 2π rotation, combined with transient absorption spectroscopy on the nanosecond time scale.

With the ZW-NAIP molecule, we are in possession of a photoswitch that achieves both Z→E and E→Z isomerizations in the femtosecond time scale. The chirality of the photoswitch is expected to induce unidirectional rotation, so that a full 2π rotation can take place by two successive isomerizations Z→E→Z (see Fig. 4.2). Equilibration after photoswitching occurs in a few tens of picoseconds, and the full 2π rotation, which requires the absorption of 2 photons, could be in principle achieved on the same time scale.

The aim of this outlook is to show that it is potentially possible to detect unidirectional motion during the photoisomerization process. We demonstrate that by tracking the anisotropy of a local vibrator which rotates during isomerization, it is in principle possible to decide whether a rotation is clockwise or anti-clockwise. The results shown here are preliminary in the sense that the anisotropy measurements were not reliable enough to get to any conclusion. We discuss the artefact that can alter the anisotropy, and the prerequisite to be able to detect unidirectional motion as an outlook, and a motivation for the work presented in the following chapters of this thesis, which aim in improving the sensitivity of ultrafast IR spectroscopies to structure.

4.2 Chirality and unidirectional rotation

First, we want to show how chirality induces unidirectional rotation during the cis to trans isomerization of the chiral NAIP photoswitches.

We can see in Fig 4.2 a chiral version of a NAIP photoswitch (ZW-NAIP presented before). We see that the chirality due to the R group will pre-twist the molecule in a preferential way. After photoisomerization, the product isomer will also be pre-twisted, and ready for the next isomerization in the same direction of rotation. This leads to unidirectional motion, and ZW-NAIP can be considered as a unidirectional rotor, achieving a complete 360° with two successive isomerizations (Z→E→Z), by absorption of two photons.

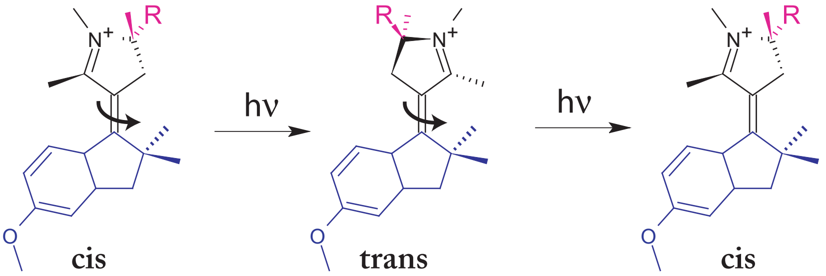

Figure 4.2: Two successive isomerizations of a chiral NAIP photoswitch. Chirality induces a preferential conformation that is pre-twisted. This leads to a preferential rotation direction which is the same for the Z→E and E→Z isomerizations.

If we are able to know the orientation of a transition dipole associated with a localized vibration rotating in time, in the molecular frame, we can be in principle sensitive to the rotation direction. This is what we described in the rest of this chapter.

4.3 Model

We describe here a simple model to understand how anisotropy changes during a cis-to-trans isomerization due to an internal rotation around a bond. The aim is to get a qualitative image of what occurs to the anisotropy from the signal of a localized mode, placed on a rotating moiety of a molecule. After electronic excitation of a UV or visible dipole triggering the isomerization mechanism, we make the hypothesis the molecules are fixed, i.e. we neglect any rotational diffusion that could affect the anisotropy on the time scale of the isomerization (isomerization occurs on the time scale of 100 fs, while rotational diffusion constant are typically on the order of tens of picoseconds).

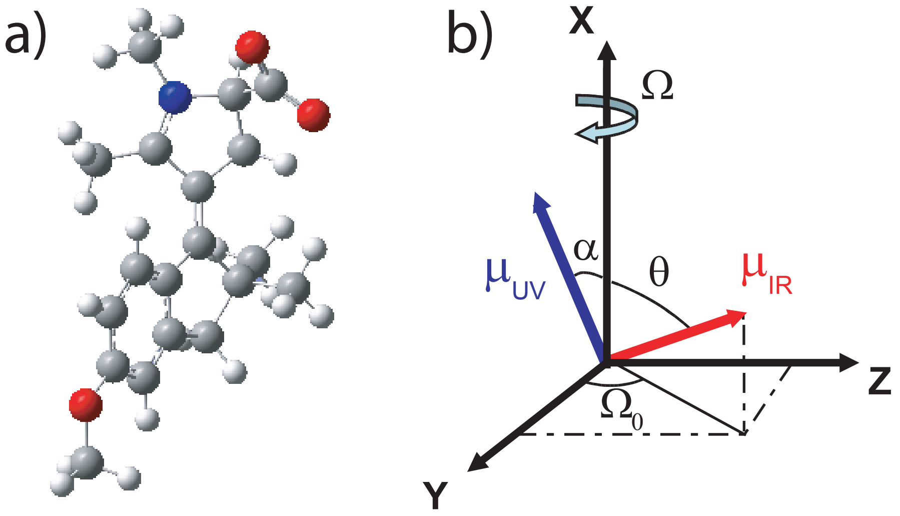

Figure 4.3: a) Structure of the Z isomer of ZW-NAIP b) Orientation of the UV (S_0-S_1)and IR (O=C=O stretch) transition dipole relative to the C1'=C4 bond axis)

The only movement considered here is the rotation of a transition dipole moment associated with the localized IR mode around the x axis (Fig.4.3). We denote Ω as the angle between the plane containing the rotation axis and the IR transition dipole μ_{IR} with the xy plane containing the electronic transition dipole μ_{UV}. This angle Ω, referred now as isomerization angle, will change during isomerization and vary from Ω_0, which correspond to the cis isomer (Z) to Ω_0+180, which corresponds now to the E isomer.

We define α and θ the angles made by μ_{UV} and μ_{IR} with the rotation axis x respectively. The angle between μ_{UV} and μ_{IR} is denoted ω (not shown in Fig. 4.3). The value of the anisotropy r between the electronic and infrared transition dipole is then:

$$r = \frac{1}{5}\left(3\cos^2\omega - 1\right) \tag{4.1}$$

This equation can be re-written in function of the isomerization angle $\Omega = \Delta\Omega + \Omega_0$ and the (fixed) azimuthal angles α and θ and takes the form :

$$r(\Omega) = \frac{1}{5}\left(3\cos^2\left(\arccos(\sin\alpha\sin\theta\cos(\Delta\Omega + \Omega_0) + \cos\alpha\cos\theta\right) - 1\right) \tag{4.2}$$

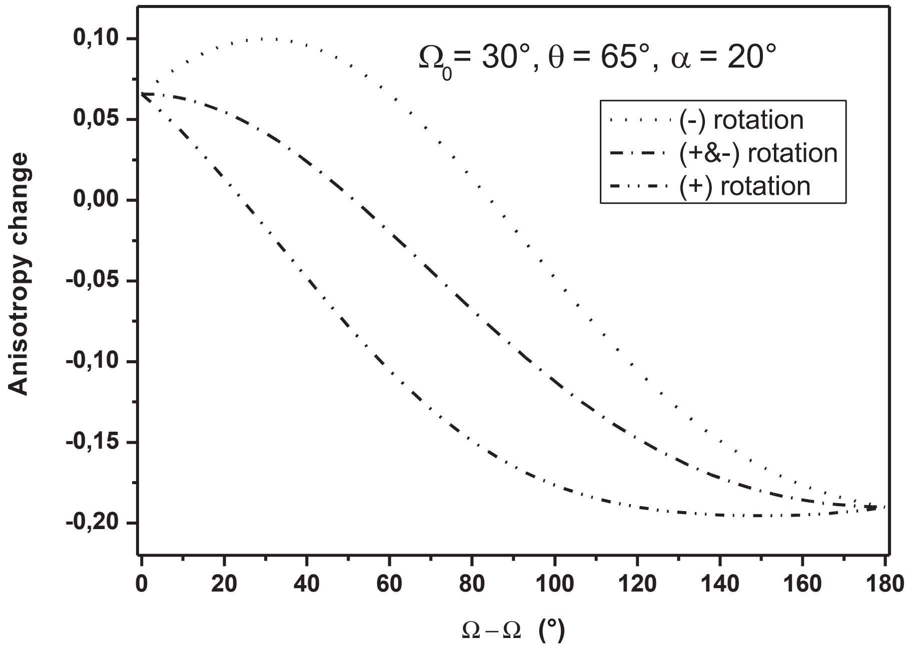

Figure 4.4: Anisotropy change in function of the isomerization angle Ω for clockwise (+) anti-clockwise (-) and mixed rotation.

We will see in the next section how we can determine this angles for a particular system, but we discuss first the different cases for different angle values. It is already interesting to see that r generally depends on the sign of $\Delta\Omega$, meaning that a clockwise (+) or anti-clockwise(-) rotation can be distinguished from the anisotropy signal. In our case described later, small values of α are assumed, meaning the electronic dipole will be oriented mostly along the rotation axis as the charge translocation due to UV excitation is responsible for the lowering of the order of the double bond around which the rotation occurs. If α or θ were null, then anisotropy would not change in function of $\Delta\Omega$, and no information about the rotation is contained in the anisotropy signal. In all other cases, the amplitude of the change depends on the relative values of α and θ. Then the distinction between (+) and (-) rotation depends on the initial value Ω_0 of the isomerization angle. For a Ω_0 of 0° or 180°, one can see that the anisotropy will be the same for clockwise or anti-clockwise rotations, as the angle between μ_{UV} and μ_{IR} will vary in the same way [1] (xy is then a symmetry plane for the system). For other angles Ω_0, the distinction between the 2 directions of rotation will be possible, the difference between (+) and (-) will then be maximal for angles Ω_0 around 45° depending slightly on the value of α).

Fig. 4.4 shows the anisotropy obtained for a set of angles (Ω_0=30°, θ=65°,α=20°) for $\Delta\Omega$ varying from 0° to 180° What we observe is that we can get a large change of anisotropy, and that the signal from clockwise and anti-clockwise rotation or a mixing of both directions of rotation can be clearly distinguish. The amplitude and absolute value of anisotropy depend on the relative values of α and θ, but the shape of the anisotropy in function of the isomerization angle depends clearly on the direction of rotation.

4.4 Molecular parameters

In the case of ZW-NAIP, the moment of inertia of the pyrroline moiety is 2.4 times smaller than that of the indanylidene group, and we expect the indanylidene orientation to change only little in the coordinate system defined by the transition dipole moments at the start of the

---

[1] cos is an even function

isomerization reaction (Fig. 4.3).

The electronic transition dipole is expected to form only a small angle α with the $C1' = C4$ double bond, due to significant charge translocation across the isomerizing C=C double bond upon S_1 excitation, and we use this double bond as the effective rotation axis. The orientation of the carboxylic group provides a good estimate for the orientation of the COO^- asymmetric stretch transition dipole moment, which we use as our mid-infrared probe.

In order to obtain more precise information on the transition dipole orientations we rely on the mixed quantum-classical minimum energy path calculations of ZW-NAIP in methanol solution reported in [26]. They reveal that the main structural changes affecting ZW-NAIP during the evolution on the excited state are the concomitant flip of the 2 methyl groups at C2' with that of C3 carbon atom See movie in [26]), while the COO^- orientation relative to the initial $C1' = C4$ double bond is essentially fixed on the way to the conical intersection. Almost the entire dipole reorientation thus happens in the electronic ground state, There are two important consequences of this theoretical prediction:

- First, those molecules (as many as 65%) which return to the initial trans conformation after excitation will contribute very little to the anisotropy changes of the O=C=O stretch band, as its orientation hardly changes along the non-reactive path.
- Second, the main reorientation of the IR-chromophore on the reactive path to E will occur after the crossing of the conical intersection, which takes place about 200 fs after excitation according to electronic transient absorption data [73].

The quantum chemistry calculations predict the orientation of the electronic transition dipole for the Z equilibrium structure to lie in the indanylidene plane, forming an angle of 12° with the isomerizing $C1' = C4$ bond. Assuming that the indanylidene is essentially fixed during the photoisomerization processes, we thus aligned all structures in the same way, with the C1' and C4 carbon atoms along the x axis, and carbon atom C9' in the xz plane. This assumption is supported by the QM/MM calculations reported before [26]. Also, they show that both the phenyl ring and the highly solvated COO^- and N(Me)+ groups remain substantially fixed during the entire motion on excited state, meaning that most of the rotation of these group are done on the ground state, after the crossing of the conical intersection. This observation is important here, are we expect the anisotropy of the COO^- to change mainly after about 200 fs (see chapter 3). The COO^- stretch transition dipole orientations for the Z and E isomers in this molecular coordinate system were then obtained by computing dipole derivatives along the normal mode coordinate in the electronic ground state. For the CI structure, we simply compared the orientation of the carboxylic group to that of the Z and E structures.

4.5 Preliminary Results : determination of the relevant angles

In order to check the reliability of the calculated transition dipole orientations, we determined the angle between the C=C stretch and the O=C=O asymmetric stretch transition dipole by polarization dependent 2D-IR spectroscopy . The angles between UV dipole and IR dipole was previously obtained from UV-pump IR-probe spectra. Both in the E and the Z conformation the measured angles are significantly smaller than the predicted ones (see table 4.1).

The determination of these angles is a priori sufficient to apply our model, as all angles needed for the model can be deduced from these results. The simulations presented above (Fig. 4.4) are qualitatively consistent with the measured angles and the rotation direction should be possible to determine with anisotropy.

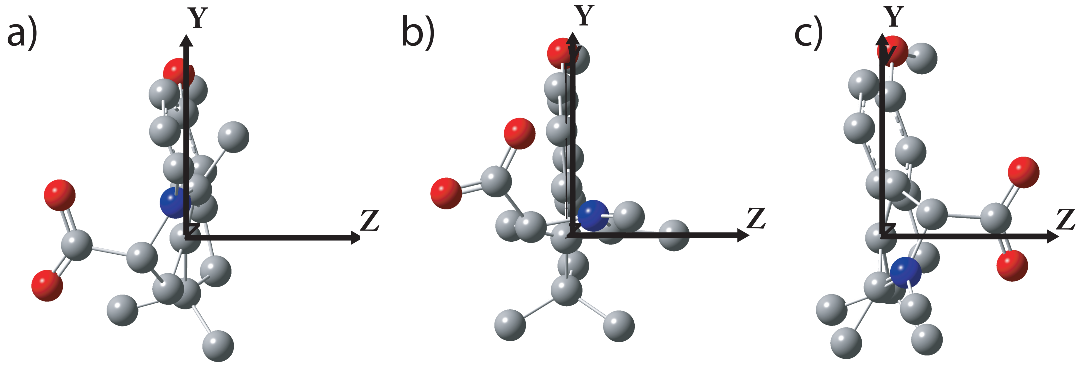

Figure 4.5: Structure of ZW-NAIP of a) Z isomer, b) at conical intersection and c) E isomer. The isomerizing C=C double bond points towards the X axis (not seen here)

Structures	Z		CI(Z)		E	
Angles in °	Exp	Th.	Exp	Th.	Exp	Th.
$\mu_{UV}, \mu_{IR(C=O)}$	50 ± 5 *	86.5	66 ± 5 *	69	78 ± 5 *	86.5
$\mu_{UV}, \mu_{IR(C=C)}$	17 ± 2 *	12.5	/	/	24 ± 5 *	14.1
$\mu_{IR(CO)}, \mu_{IR(C=O)}$	55 ± 5 †	74	/	/	55 ± 5 †	81

Table 4.1: Table of angles determined with ∗ UV-IR pump-probe spectroscopy, † 2D-IR spectroscopy

Some measurements of the anisotropy were carried out, but we made the choice to not present them here, as they were not reproducible and not convincing enough to draw any conclusions.

There are different reasons that might alter the anisotropy data. First, different background contributions for parallel and perpendicular probing are affecting the data at short delays, due to the overlap of pump and probe pulses. Then, slightly different structures of ZW-NAIP might be present in solution, as the COO^- group is free to rotate around the bond that links it to C2, this would lead to a distribution of transition dipole directions, and our simple model would not apply in that case. Also, the spectral overlap of the C=O mode with another mode involving the 6-membered ring that might contribute to the signal is possible. The relatively low quantum yield is also a limitation to the signal.

This is where we decided to improve the sensitivity of the experiments to the structure, in order to get a more precise picture of the anisotropy changes in time.

4.6 Conclusion and Outlook

We showed that it is in principle possible to detect unidirectional rotation by following anisotropy in time. The three curves of Fig.4.4 are in fact distinct, and it is reasonable to think that we could distinguish between them. We were in fact limited by the reliability of our anisotropy measurements to really have enough confidence and draw conclusion on the directionality of rotation of the ZW-NAIP photoswitch.

Although we used racemic mixture of ZW-NAIP, the two enantiomer are in fact expected to give rise to the same signal. The model presented here depends only on internal angles, and they will move relatively to each other in the same way for the R or S isomer. Even if the two are rotating in opposite directions, they will display the same time dependence in function of the anisotropy.

The ZW-NAIP photoswitch is still a promising system which has the potential to achieve unidirectional motion and could be used as a light-fuelled rotor in the nanoscale [92].

Anisotropy can be affected by different artefact such as baseline, kerr effect during pump and probe pulse overlap, fluctuations of the laser between the acquisition of parallel and perpendicular pump-probe polarizations. This observation motivated the following chapters, where we show that we can significantly increase the signal to noise of ultrafast spectroscopy experiment and particularly amplify the anisotropic component of the signal, keeping the possibility to measure angles with better accuracy.

Part III

Linear dichroism enhancement

Measuring the linear dichroism (LD) in a time resolved experiment can provide a lot of structural and dynamic information about photoinduced processes [93, 94]. The near-crossed polarizer technique has proven to be useful to improve signals and to measure circular dichroism [56, 95] and circular birefringence [96]. It was also applied to the measurement of LD in time resolved measurements in the nanosecond time scales [97], with impressive improvements in sensitivity. In their article, Che et al., from the group of Prof. D. Kliger , applied the near-crossed polarizer technique on Bacterio-Rhodopsin, a protein of the purple membrane of Halobacterium Halobium. They demonstrate an amplification of more than a hundred in the visible transient absorption signal 10.5 ms after photoexcitation. This is possible because reorientation, which is the principal reason of the decrease of linear dichroism in time, occurs on a time scale of 100 ms.

The application of this technique in the infrared requires very high quality polarizers that where not available until recently, no application of this technique to femtosecond pump-probe spectroscopy was found in literature, even in the visible, where polarizers have typically very high extinction ratios.

Anisotropy or linear dichroism measured in pump-probe spectroscopy can be calculated when pump and probe pulses have different polarizations. In a few words, the pump pulse is polarized and as it interacts with the sample induces dichroism. This dichroism is a consequence of the fact that the electric field of the light interacts with the molecule through the electric dipole moment of transition, which has a well defined orientation in the molecular frame. When the pump light hits the sample, only a subset of molecule with a certain orientation are excited (with transition dipoles aligned with the pump polarization). Then, the anisotropy can be translated into an angle between the pumped and probed transition dipoles, and is in this regard the most direct structural information one can get from pump-probe spectra. The connection between the anisotropy values and transition dipole angles has been derived earlier [44, 53] and is given in the first part of this thesis.

In the context of this work, we use the properties of LD and manipulate the pump and probe polarizations to increase the signal to noise ratio of our experiment [29] using the near-crossed polarizer geometry. The use of polarizers in the probe beam permits to use intense fields at the sample and to amplify the LD component of the signal. In chapter 5, the equations for the amplified signals are derived for the particular problem of linear dichroism (LD) enhancement using nearly crossed polarizers in the probe beam. For this purpose, Müller matrix calculus is used, but the details of this computation are found in appendix C. Then, the application of the method to the amplification of LD and to the calculation of angles between transition dipole moments is given. The signals are analysed and the influence of unwanted contribution like birefringence, or non-ideal polarization are taken into account. In chapter 6 we demonstrate the amplification principle to a photoswitch of the NAIP family introduced earlier. One great advantage of the technique is that the transition dipole angles can be determined more accurately. Also, we analyse our signal and make use of fast modulation techniques to increase the sensitivity and shorten the measurement time. We also examine the experimental limitations of this set-up.

We demonstrate in chapter 7 that the method can be extended to 2D-IR spectroscopy with very little modifications. With 2D-IR spectroscopy, we study the structures and conformational changes of molecules with the additional information of coupling between normal modes of vibration. We perform 2D-IR spectroscopy in the pump-probe geometry in the time domain, which has become one of the easiest way to implement 2D-IR spectroscopy [38–40]. The purpose of 2D-IR is to build two dimensional maps of the spectra consisting of a pump and a probe axis, which means we resolve the pump axis in frequency. This allows us to disentangle features in the spectra that are not accessible with 1D transient spectroscopy. The diagonal and cross peaks are better separated and use of polarization allows one to manipulate their relative intensities. The determination of coupling between normal modes of vibration as well as the relative orientation between their transition dipole moment makes 2D-IR spectroscopy a sensitive tool for the determination of structures [37,42,43,45,98,99]. The same advantages as in UV-pump IR-probe spectroscopy are demonstrated for the 2D signals. Other advantages like peak elimination or scattering suppression make this technique attractive for implementation in 2D spectroscopy.

Additionally, we demonstrate another new implementation of the experimental set-up which allows us to measure dispersive 2D-IR spectra instead of absorptive. Lastly, we show that we can easily deduce the rephasing and non-rephasing spectra that were not obtainable before with this set-up.

Chapter 5

Linear dichroism enhancement with the near-crossed polarizer technique

5.1 Introduction

In this thesis, we built a set-up that enhances S/N in UV-pump IR-probe spectroscopy and 2D-IR spectroscopy in the pump-probe geometry. This is done by placing the sample between nearly crossed polarizers, which allows one to have an intense field on the sample, but a weak field on the detector (see 1.10). We will see that this amplifies the anisotropic component of the molecular response. The mathematics needed to understand the signal measured with this set-up are described here. The advantages and limitations of this geometry are then discussed.

5.2 Linear dichroism and anisotropy

Linear dichroism (LD) and anisotropy are essentially two metrics of the same quantity. LD is usually defined as [50] :

$$LD = \frac{\Delta A_{\parallel} - \Delta A_{\perp}}{2} \ln(10) \tag{5.1}$$

while anisotropy is defined by the ratio:

$$a = \frac{\Delta A_{\parallel} - \Delta A_{\perp}}{\Delta A_{\parallel} + 2\Delta A_{\perp}} \tag{5.2}$$

with $\Delta A_{\parallel}$ and $\Delta A_{\perp}$ being the transient absorption changes measured for parallel and perpendicular polarization of pump and probe pulses, respectively:

$$\Delta A_{\parallel} = \log_{10}\left(\frac{I_{\parallel}^{\text{pumpon}}}{I^{\text{pumpoff}}}\right) \quad , \quad \Delta A_{\perp} = \log_{10}\left(\frac{I_{\perp}^{\text{pumpon}}}{I^{\text{pumpoff}}}\right) \tag{5.3}$$

Where the I's are the intensities measured on the detector. In each of these equations, we are mostly interested in the orientational dependence of the absorbance or the intensities.
The intensities in Eq. 5.3 are proportional to the orientational pre-factor:

$$I_{\parallel}^{\text{pumpon}} \propto \langle XXXX \rangle \tag{5.4}$$

$$I_{\perp}^{\text{pumpon}} \propto \langle XXYY \rangle \tag{5.5}$$

$$I^{\text{pumpoff}} \propto \langle XX \rangle \tag{5.6}$$

where I^{pumpoff} is the intensity of the probe without previous excitation by the pump pulse, which is affected only by the linear absorption.

5.3 The near-crossed polarizer technique

In Fig.5.1 is depicted the experimental scheme we use for linear dichroism enhancement measurements. A first polarizer in the probe beam is set to a small angle β relative to the X axis, it passes the sample which is photoexcited with a pump pulse set at ±45° relative to the X axis. Then a second polarizer is set along Y.

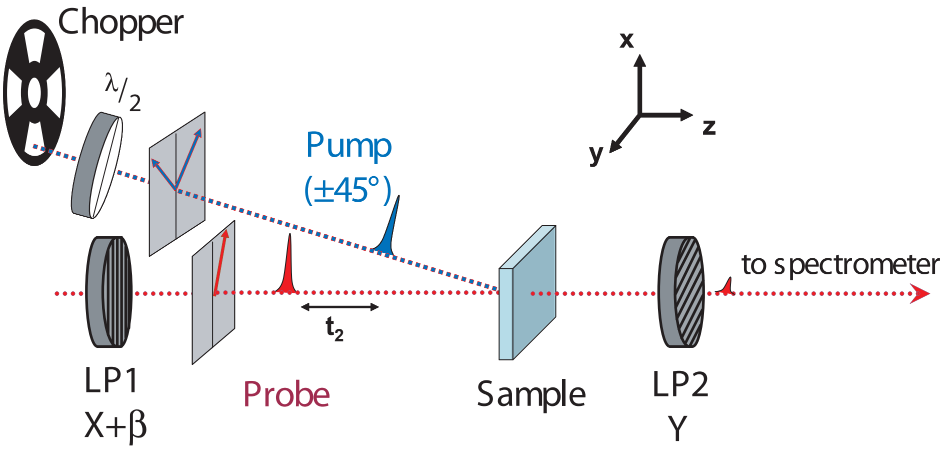

Figure 5.1: Set-up for LD enhancement. The intense probe at the sample is attenuated with polarizer LP2 to generate a weak heterodyning field. Pump pulses are set alternatively to + or - 45° with a half-wave plate $\lambda/2$.

When pump is off, the intensity I_0 of detected light is:

$$I_0 \propto \langle Y(X\cos(\beta) + Y\sin\beta)\rangle \tag{5.7}$$
$$I_0 \propto \langle YY\rangle \sin(\beta) \tag{5.8}$$

as the tensor $\langle XY\rangle$ vanishes (Appendix B).

A chopper synchronized with the laser alternatively blocks on pump pulse over two. When pump is on, with a polarization of $\pm 45\ \circ$, the detected intensity becomes:

$$I_{\pm}^{pumpon} \propto \langle Y\left(X\cos(\beta) + Y\sin\beta\right)\frac{1}{2}(X \pm Y)\rangle\rangle \tag{5.9}$$
$$\propto (\langle YYYY\rangle + \langle YYXX\rangle)\sin(\beta) \pm (\langle YXYX\rangle + \langle YXXY\rangle)\cos(\beta) \tag{5.10}$$

which with the relation (Eq. 1.22) gives:

$$\langle XYXY\rangle + \langle YXXY\rangle = \langle YYYY\rangle - \langle YYXX\rangle \tag{5.11}$$

and finally, the absorption change, which is the ratio of the intensity measured with the pump and the intensity measured without pump :

$$\begin{aligned}\Delta A_{\pm} &\propto \frac{\langle Y(X\cos\beta + Y\sin\beta)\frac{1}{2}(X\pm Y)^2\rangle}{\langle Y(X\cos\beta + Y\sin\beta)\rangle} \\ &\propto (\langle YYYY\rangle + \langle YYXX\rangle) \\ &\quad \pm(\langle YXYX\rangle + \langle YXXY\rangle)\cot\beta \\ &\propto (\langle YYYY\rangle + \langle YYXX\rangle) \\ &\quad \pm(\underbrace{\langle YYYY\rangle}_{\propto\Delta A_{\parallel}} - \underbrace{\langle YYXX\rangle}_{\propto\Delta A_{\perp}})\cot\beta\end{aligned} \tag{5.12}$$

which we can re-write:

$$\Delta A_{\pm} = \frac{1}{2}(\Delta A_{\parallel} + \Delta A_{\perp}) + \frac{1}{2}(\Delta A_{\parallel} - \Delta A_{\perp})\cot(\beta) \tag{5.13}$$

or, with $\overline{A}$ the average absorption between parallel and perpendicular probing:

$$\overline{A} = \frac{1}{2}(\Delta A_{\parallel} + \Delta A_{\perp})\ln(10) \tag{5.14}$$

and with the definition of the linear dichroism from Eq. 5.1, we finally obtain the expression of the absorption:

$$\boxed{\Delta A_{\pm} = \frac{1}{\ln(10)}\left(\overline{A} \pm LD\cot\beta\right)} \tag{5.15}$$

This is an important equation that shows that with the set-up of Fig.5.1 we can amplify the linear dichroism by decreasing β.

The important advantage of this configuration is that the polarizer LP2 in Fig. 5.1 acts as an intensity filter for the LO, so that the heterodyning field can be attenuated relative to the probe field. It means that the signal amplitude is now not limited by the dynamic range of our detector, but by the intensity of the probe field. However, we will see in the paragraph 5.5, that the extinction ratio of the polarizers and the amplitude of the dichroism have also an importance and can limit the amplification.

The difference between the two transient absorptions measured at $\pm\beta$ is also useful. The signal s calculated this way leads to:

$$\begin{aligned}s &= \Delta A_{+} - \Delta A_{-} \\ &= \frac{2}{ln(10)}LD\cot\beta\end{aligned} \tag{5.16}$$

The signal here depends only on the LD and the amplification. The isotropic contribution are completely suppressed from s. Background or temperature signals are usually isotropic and are then suppressed by this subtraction. We will see also that when applied to pump-probe spectroscopy in the UV, we can calculate s without the need to measure the individual $\Delta A_{\pm}$, but only the intensities $I_{\pm}^{pumpon}$, without the need of measuring a reference. (we can then remove the chopper in Fig. 5.1).

According to Malus'law, the intensity of perfectly linearly polarized light going through a perfect polarizer is:

$$I = I_0 \cos^2 \beta \tag{5.17}$$

with β the angle between the light polarization axis and the polarizer axis. This relation can be extended for the fields with $I = E^2$. In our set-up, the field before the second polarizer is E_{probe} while the field after it is E_{LO}. We get:

$$E_{LO} = E_{probe} \cos \beta \tag{5.18}$$

so that for the same intensity E^2_{LO} on the detector, the signal is amplified by $\cot \beta$. The table below shows how the amplification $\cot \beta$ and the relative intensity between E_{probe} and E_{LO} scale with decreasing β:

$\beta(°)$	45	20	10	7	5	3	2
$\cot \beta$	1	2.7	5.7	8.1	11.4	19.1	28.6
$1/\cos \beta$	1.4	2.9	5.8	8.2	11.4	19.1	28.6

5.4 Angle determination

The dependence of the different signals on the angle ω between the transition dipoles interacting with pump and probe beam are now readily found from well known expressions for orientational averages [44](see table 1.1):

$$\begin{aligned} \Delta A_{\parallel} + \Delta A_{\perp} &\propto \frac{2P_2[\cos(\omega)] + 10}{45} \\ \Delta A_{\parallel} - \Delta A_{\perp} &\propto \frac{2P_2[\cos(\omega)]}{15} \end{aligned} \tag{5.19}$$

where the same proportionality constant applies in both lines, and where P_2 is the second order Legendre polynomial ($P_2(\cos(2\omega)) = \frac{1}{2}(3\cos^2(2\omega) - 1)$).

From 5.20, we can see that LD is related to the intramolecular angle ω by the relation:

$$LD = \overline{A}(\omega) \frac{1 + 3\cos(2\omega)}{7 + 2\cos(2\omega)} \tag{5.20}$$

We define $|\beta_0|$ as the probe polarization angle at which one of the two signals ($\Delta A_{\parallel}$ or $\Delta A_{\perp}$) can be eliminated (Fig. 5.2):

$$\tan \beta_0 = \frac{\Delta A_{\parallel} - \Delta A_{\perp}}{\Delta A_{\parallel} + \Delta A_{\perp}} = \frac{1 + 3\cos(2\omega)}{7 + \cos(2\omega)} \tag{5.21}$$

Combining with Eq. 5.15, we can connect the amplified signals with the internal angle ω through the knowledge of β_0 :

$$\Delta A_{\pm} = \frac{\overline{A}}{\ln(10)} \left(1 \pm \frac{\tan \beta_0}{\tan \beta} \right) \tag{5.22}$$

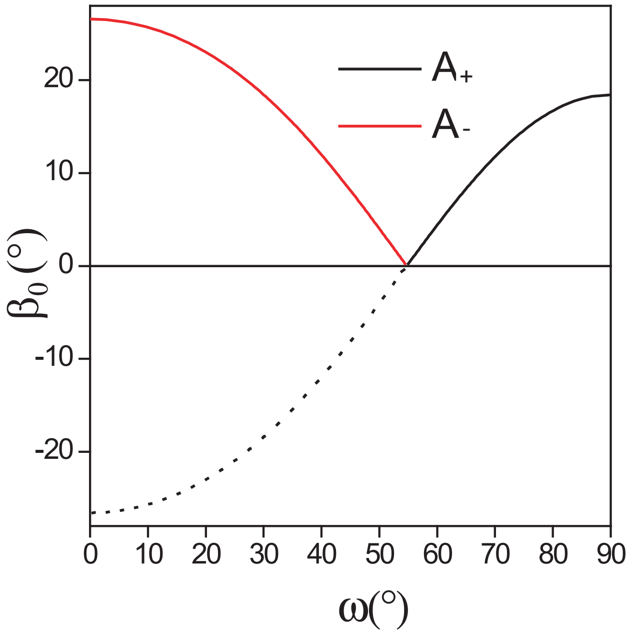

Figure 5.2: Polarizer angle β_0 for peak elimination in the 2D-spectra as a function of the intramolecular angle ω between excited and probed transition dipoles. Peaks with positive anisotropy are eliminated in the ΔA_- signal, those with negative anisotropy in the ΔA_+ signal. When the pump polarization is fixed at +45° and β is varied instead of distinguishing between $\Delta A_\pm$, the dashed line is obtained.

Now we will see that with the amplified signals ΔA_+ and ΔA_-, we can determine β_0 and ω with a better accuracy.

Angle accuracy

The usual method to determine angles between transition dipole moments is to compare the absorption with parallel and perpendicular probing, at short delay time between pump and probe, to avoid the reorientation effect due to rotational diffusion[1]. The anisotropy calculated with the formulae 5.2 leads directly to ω as:

$$\cos^2\omega = \frac{1}{3}(5\alpha + 1). \tag{5.23}$$

so that an anisotropy of $\alpha = 0.4$ corresponds to an angle $\omega = 0$; $\alpha = 0$ to the magic angle $\omega = 54.7°$ and $\alpha = -0.2$ is associated to a perpendicular angle $\omega = 90°$.

For better comparison with the polarization-enhanced measurements we introduce a slightly different 'anisotropy' metric α':

$$\alpha' = \frac{\Delta A_\parallel - \Delta A_\perp}{\Delta A_\parallel + \Delta A_\perp} = \frac{3\alpha}{2+\alpha} \tag{5.24}$$

The angle between transition dipoles is now given by:

$$\cos^2\omega = \frac{3\alpha' + 1}{3 - \alpha'}. \tag{5.25}$$

and this metric can be generalized to

---

[1] This delay as to be short relative to the rotational diffusion constant

$$\alpha'' = \frac{\Delta A_+ - \Delta A_-}{\Delta A_+ + \Delta A_-} = \alpha' \cot|\beta| \tag{5.26}$$

with the special case $\Delta A_- = \Delta A_\perp$ and $\Delta A_+ = \Delta A_\parallel$ when $\beta = 45°$. Since the difference between ΔA_+ and ΔA_- can be made larger by a factor $\cot\beta$ with respect to conventional measurements without increasing noise, α'' and thus α' and ω can in principle be determined with much better accuracy for small polarizer angles β. This requires, however, that β must be set and known precisely.

Advantages and limitations of intramolecular angle determination in polarization enhanced measurements are best illustrated with the help of a graphical evaluation: according to equation 5.15, the signals $\Delta A_\pm$ recorded with different polarizer angles all lie on the same straight line when plotted against $\cot\beta$. In order to symmetrize the problem we use positive and negative values of β instead of distinguishing between ΔA_- ($\beta < 0$) and ΔA_+ ($\beta > 0$). The conventional signals $\Delta A_\perp$ and $\Delta A_\parallel$ then correspond to $\cot\beta = -1$ and $\cot\beta = +1$, respectively. The smaller $|\beta|$ the further the signals $\Delta A_\pm$ lie apart, and the more accurately we can determine the intercept of the line connecting them with the horizontal axis (see Fig. 5.3b). This intersection defines the angle β_0 at which either the ΔA_+ or the ΔA_- signal vanishes.

With $\alpha' = -\frac{1}{\cot\beta_0}$ determined graphically, we can calculate the intramolecular angle using :

$$\cos^2\omega = \frac{1 - 3\tan\beta_0}{3 + \tan\beta_0}, \tag{5.27}$$

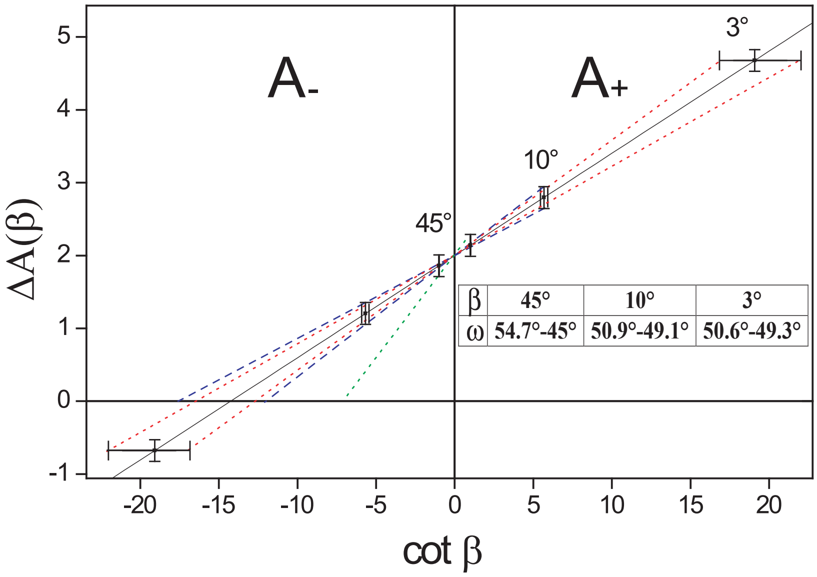

β	45°	10°	3°
ω	54.7°-45°	50.9°-49.1°	50.6°-49.3°

Figure 5.3: Graphical illustration of the determination of intramolecular angle, assuming $\omega = 50°$, 20% noise and a ±0.2° uncertainty of β. The lines joining the signals $\Delta A_\pm$ cross the horizontal axis at $\cot\beta_0 \le -2$ for positive anisotropy and $\cot\beta_0 \ge 3$ for negative anisotropy. Inset: possible values of ω determined for β.

There are two sources of error in the determination of β_0: one is the noise on the measured signals $\Delta A_\pm$, represented by vertical error bars, the second is the accuracy in setting the pump and probe polarization angles, which gives rise to horizontal error bars in Fig. 5.3. The vertical error bars are approximately constant at all angles β, and therefore become less and less important as the signals are enhanced and move further apart in the plot. For a very small polarizer angle, however, the uncertainty in $\cot\beta$ is so large that the line joining the signals becomes again ill-defined. With the parameters used in Fig. 5.3b, the intramolecular angle ω can hardly be defined from the conventional measurements ($\beta = 45°$). For $\beta = 10°$ boundaries can be found (blue dashed lines), which are still limited by the vertical error bars, i. e. the noise of the signals. For $\beta = 3°$, on the other hand, the uncertainty of β is determining the range of possible values of $\cot\beta_0$ (red dashed lines). Measurements at smaller polarizer angles with even larger horizontal error bars will not lead to further improvement. For nearly parallel or perpendicular transition dipoles the line joining the signals is much steeper and the horizontal uncertainty becomes dominant already for much smaller values of $\cot\beta$. The best choice of β for intramolecular angle determination thus strongly depends on the specific experimental conditions (noise, waveplate quality and alignment) as well as the transitions investigated. The largest improvement over conventional measurements can be expected for relative transition dipole orientations near magic angle, i. e. when the signals with parallel and perpendicular pump and probe polarizations are almost identical.

5.5 Limitations and Müller matrices analysis

The expressions derived above are idealised and if we want to have a realistic vision of the experiment's output, we need to consider the effects of imperfect polarizers, as well as the influence of pump-induced linear birefringence. This will lead to expressions which are slightly different from above, and the signal's dependence over β will become different.

The equation for the LD amplification (Eq. 5.15) can also be derived using Müller matrices, and this will help to analyse our set-up. At each optical element is associated a 4×4 matrix and the polarization of the light is described with the Stokes vector (see Appendix C). The advantage of Müller matrices description is that we can take easily into account the imperfection of polarizers in the equation, as well as other optical phenomena like linear birefringence.

5.5.1 Set-up characterisation with Müller matrices: ideal signal

The full matrix for the set-up of Fig. 5.1 is given by:

$$M^{\pm} = M_{LP}(\frac{\pi}{2}).M^{\pm}_{sample}.M_{LP}(\beta) \tag{5.28}$$

where $M_{LP}(\theta)$ is the matrix for a linear polarizer at an angle θ, and $M^{\pm}_{sample}$ is the sample matrix, equivalent in our case to the matrix for linear dichroism at 45°. The ± signs indicates that we have two possibilities of measurement with the pump beam polarized at ±45°.

The intensity measured on the detector is given by the scalar product of the first row of M with the Stokes vector ($\overrightarrow{V}_{in}$)of the incoming light:

$$I_{\pm} = \left(M^{\pm}.\overrightarrow{V}_{in}\right)_1 \tag{5.29}$$

With the matrices described in Appendix C, in the limit of perfect polarizers and to a linear order of $\overline{A}$ and LD we get:

$$\frac{I_{\pm}^{pumpon}}{I_{\pm}^{pumpoff}} = 1 - \overline{A} \mp LD\cot\beta \tag{5.30}$$

or after taking the decadic logarithm:

$$\Delta A_{\pm} = \frac{1}{ln(10}(\overline{A} \pm LD\cot\beta) \tag{5.31}$$

$$= \frac{1}{2}((\Delta\overline{A}_{\parallel} + \Delta\overline{A}_{\perp}) \pm (\Delta\overline{A}_{\parallel} - \Delta\overline{A}_{\perp})\cot\beta) \tag{5.32}$$

Which is the same as Eq. 5.15 derived earlier.

5.5.2 Set-up characterisation with Müller matrices: realistic signal

When using matrices of non-perfect polarizer, with extinction ratio r, and taking into account the effect of linear birefringence in the sample, we get the general equation for s (see Eq. 5.16):

$$s = \frac{(1-r^2)\sin(2\beta)\sinh(LD)}{(1+r)^2\cosh(LD) - (1-r)^2\cos(2\beta)\cos(LB)} \tag{5.33}$$

In the next sections, we analyse the consequence of the expression 5.33 to understand the influences of r, LB and large LD on the measured signal.

5.5.3 Limitations due to polarizer extinction ratio

The polarizer extinction ratio can be a limitation when β is getting small. Using the matrix for non perfect polarizers, and assuming no LB and a small LD, we get to the expression of the signal below:

$$s \approx \frac{LD}{\beta + (2r/\beta)} \tag{5.34}$$

so that the signal as a limit when $\beta \approx \sqrt{2r}$, corresponding to an enhanced LD signal $s_{max} \approx LD/2\sqrt{2r}$.In Fig. 5.4), we can see the calculated signal for different polarizer extinction ratio, .

r	10^{-2}	10^{-3}	10^{-4}	10^{-5}
$\beta_{max}(°)$	8.1	2.6	0.8	0.26
Amplification	7.2	22.3	70.7	223.6

In the visible, polarizers with extinction ratio smaller than 10^{-5} are usual, while in infrared, polarizers with such extinction are rare and expensive. Standard wire-grid polarizers have a extinction ratio of the order of 10^{-2}, while Brewster angle polarizers [51] made of germanium can have extinction ratio lower than 10^{-6}, but these are bulky, expensive and have a low transmission of the desired polarization. Here, we will use free standing wire-grid polarizers with an extinction ratio better than 10^{-4}, described in the experimental chapter.

5.5.4 Limitations due to LD amplitude

When the polarizers are sufficiently good, the possible signal enhancement may depend on the size of the LD itself, as can be seen by evaluating Eq. 5.33. For example, a (unamplified) LD of 10^{-2} could be magnified at most by a factor of approximately 200 ($\beta = 0.2°$) and the signal would change linearly with $\cot\beta$ only up to about 0.5° (see Fig. 5.5). This may distort spectra,

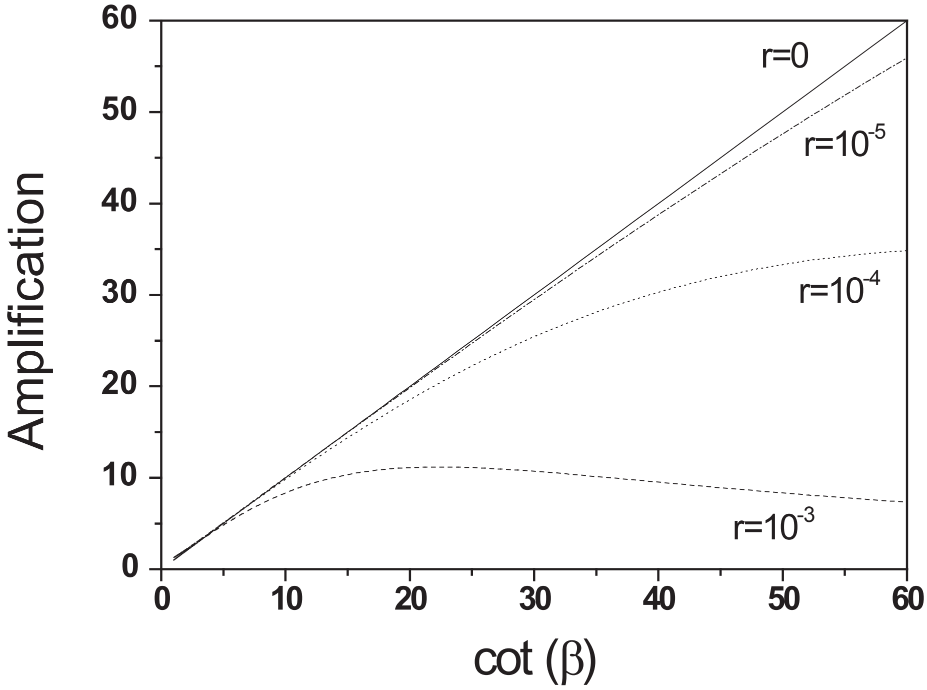

Figure 5.4: Plot of the expected absorption, with LD=1 mOD for different extinction ratio of the polarizers. In this case, LD is not the limiting factor for amplification (see next section).

in particular in electronic spectroscopy, but will rarely be the limiting factor in the mid-IR, where transient absorption changes are typically much smaller.

In this case also, the relative contribution of Linear Birefringence (LB) with respect to the isotropic (not amplified) signals in the $\Delta A_{+\beta}$ and $\Delta A_{-\beta}$ spectra grows.

5.5.5 Linear Birefringence

The linear birefringence is also a possible artefact we have to take into account [96]. Linear birefringence (now LB) is related to the pump-induced change of index of refraction which is indissociable from a change in absorption, and LB and absorption changes are related through the Kramers-Kronig relation. LB is defined as follows [50]:

$$LB = 2\pi \frac{L}{\lambda}(\Delta n_{\parallel} - \Delta n_{\perp}) \tag{5.35}$$

with $\Delta n_{\parallel}$ and $\Delta n_{\perp}$ the refractive index change induced, L the pathlength and λ the wavelength. The effects of LB can be included in the matrix describing the sample (See appendix C), and it gives, to the lowest order of LB and LD:

$$\Delta A_{\pm} \approx \frac{1}{ln(10)} \left[\overline{A} \pm LD \cot\beta \left(1 - \frac{\cot^2(\beta - 1)}{4} LB^2 \right) \right] \tag{5.36}$$

which means LB has an effect <1% as long as β>5LB.
The contributions from LB are anyway totally suppressed when we take the difference between ΔA_+ and ΔA_-.

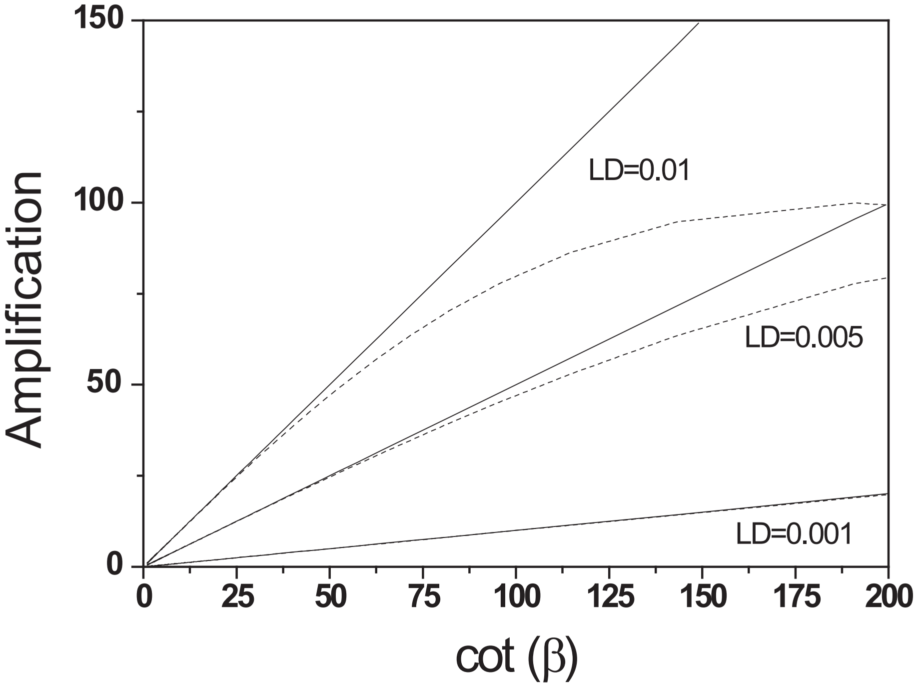

Figure 5.5: Dotted : Plot of the real signal for different LD assuming perfect polarizers. Plain : the theoretical linear amplification in $\cot\beta$

5.5.6 Mystic angle measurements

For delays delays between pump and probe pulse when the rotational diffusion effect can not be neglected, the anisotropy decays due to the isotropic reorientation of the transition dipoles. The dependence on pump-probe delay t for molecules that behave like spherical diffusors is readily obtained by multiplying the second order Legendre polynomial P_2 by e^{-6Dt}, where D is the diffusion constant [44].

In the same way magic angle measurements allow to get rid of the rotational diffusion in a usual pump-probe measurement, it is possible to define an angle β_M called mystic angle [52] and corresponding to the isotropic signal with our set-up. Combining Eq. 5.15 and Eq. 5.20, we arrive at :

$$\tan(\beta_M) = \frac{1}{3} \qquad\qquad \beta_M \approx 18.43^\circ \tag{5.37}$$

5.5.7 Including a small angle between pump and probe beams

It is possible to evaluate the signals when pump and probe beams intersect at the sample at an angle δ and therefore have different planes of polarization [53]. The pump will have a small projection of its polarization in the Z directions, and with the substitutions :

$$\begin{aligned}
X_{pump} &= X_{probe} \\
Y_{pump} &= Y_{probe}\cos(\delta) - Z_{probe}\sin(\delta) \\
Z_{pump} &= Y_{probe}\sin(\delta) + Z_{probe}\cos(\delta)
\end{aligned} \tag{5.38}$$

the pump-induced absorption changes become:

$$\begin{aligned}
\Delta A_{\pm} &\propto \frac{\langle Y(X\cos\beta + Y\sin\beta)\frac{1}{2}(X + [Y\cos\delta - Z\sin\delta])^2\rangle}{\langle Y(X\cos\beta + Y\sin\beta)\rangle} \\
&\propto \left(\langle YYYY\rangle\cos^2\delta + \langle YYXX\rangle + \langle YYZZ\rangle\sin^2\delta\right) \\
&\quad \pm \cot\beta\left(\langle YXYX\rangle + \langle YXXY\rangle\right)\cos\delta \\
&\propto \left(\Delta A_{\parallel}\cos^2(\delta) + \Delta A_{\perp}(1 + \sin^2(\delta))\right) \\
&\quad \pm \cot(\beta)\left(\Delta A_{\parallel} - \Delta A_{\perp}\right)\cos(\delta).
\end{aligned} \tag{5.39}$$

So that δ lowers the signal of $\cos(\delta)$. This angle is evaluated to be around 5° in our experiment, which corresponds to an attenuation of approximately 0.5% on the signal.

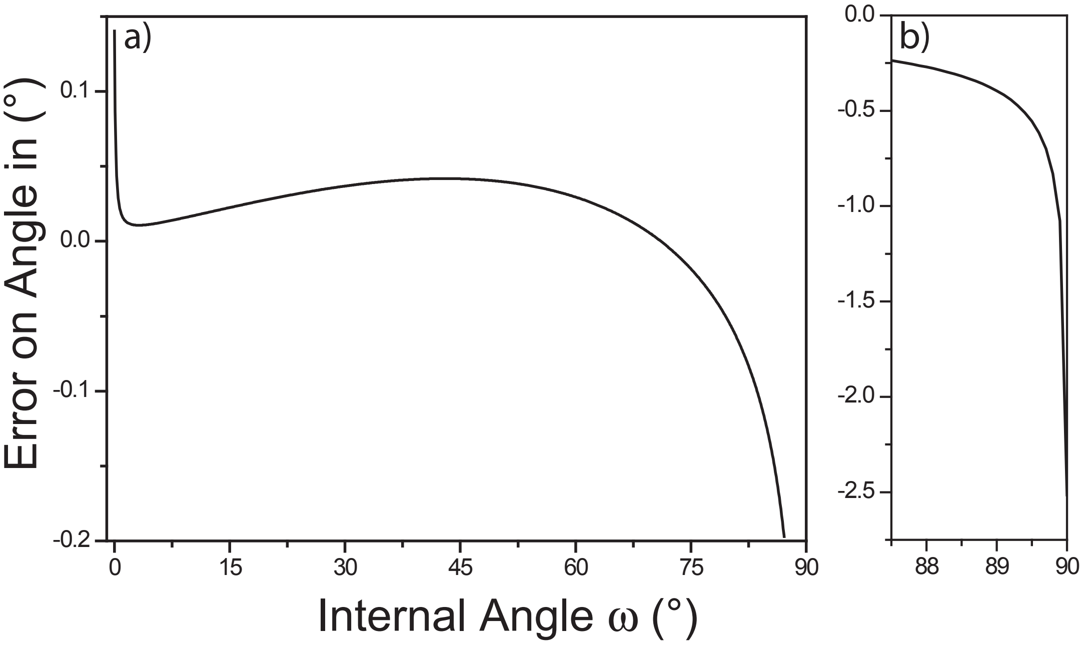

Figure 5.6: a) Estimated error on angle ω in function of ω considering an angle $\delta = 5°$ b) zoom for angles ω near 90°.

To take into account the effect of δ on the determination of ω, we plotted in Fig. 5.6 the error made on ω considering an angle $\delta = 5°$. We can see that the inaccuracy is small ($< 0.2°$) in most of the curve. Only for ω near 90°, there is an underestimation which is not negligible and on the order of 2°. This effect scales with δ.

Chapter 6

Linear dichroism enhancement in UV-pump IR-probe spectroscopy

In this chapter, we demonstrate strong amplification of polarization-sensitive transient IR-signals using the crossed polarizer technique first proposed by Keston et al. [100] and applied for nanosecond flash photolysis in the visible by Che et al. [97]. The equations explaining the amplification processes are derived in chapter 5. We adapted the technique to ultrafast pulsed laser spectroscopy in the infrared using photoelastic modulators, which allow us to measure amplified linear dichroism at kilohertz repetition rates. The method was applied to a photoswitch of the N-alkylated Schiff base family (see Fig. 6.3) in order to demonstrate its potential of strongly enhancing sensitivity and signal to noise in ultrafast transient IR experiments, to simplify spectra and to determine intramolecular transition dipole orientations. The basic principle of the method is illustrated in Fig. 6.1.

Transient absorption signals $\Delta A_{\|}$ and $\Delta A_{\perp}$ can be measured by changing the probe light polarization (red, Fig. 6.1) from parallel to perpendicular with respect to the pump-pulse polarization (blue, Fig. 6.1). In order to calculate each of the two transient signals $\Delta A_{\|}$ and $\Delta A_{\perp}$, the light intensity $I_{\|}$ or $I_{\perp}$ measured by the detector in the presence of the pump-pulse is divided by the intensity with the pump-pulse blocked. Because of this normalization, the same transient absorption and linear dichroism signals are obtained when parallel and perpendicular polarized pulses are attenuated behind the sample by the same amount, for example by inserting a horizontally oriented polarizer at 45° with respect to the pump-polarization direction (see Fig. 6.1b). Che et al. [97] showed that the LD signal can be significantly enhanced, when the angle between the two probe polarizations is now reduced from 90° to a small angle 2β as indicated in Fig. 6.1c. Explicitly, they showed that :

$$s = \frac{I_{+\beta} - I_{-\beta}}{I_{+\beta} + I_{-\beta}} \approx \frac{LD}{\tan\beta}. \tag{6.1}$$

Linear dichroism measurements in picosecond time-resolved electronic spectroscopy were originally carried out with exactly crossed polarizers (β=0) [94, 96], in which case the pump-induced transmission of the probe light depends quadratically on LD, but also on linear birefringence(LB). When one of the two polarizers is slightly tilted, a small fraction of the probe light leaks to the detector and can selectively heterodyne the additional field due to pump-induced linear dichroism [52]. If we use this language, the signal of Eq. 6.1 is the difference of two measurements with opposite phases of the heterodyning field, a common technique in modern time-resolved IR spectroscopy.

Here, we show how to reliably use this principle in ultrafast pump-probe experiments in the mid-IR. The formalism we derived earlier in chapter 5 can be used to describe the transient absorption signals for individual angles β (In [97], Che et al. used only the difference between

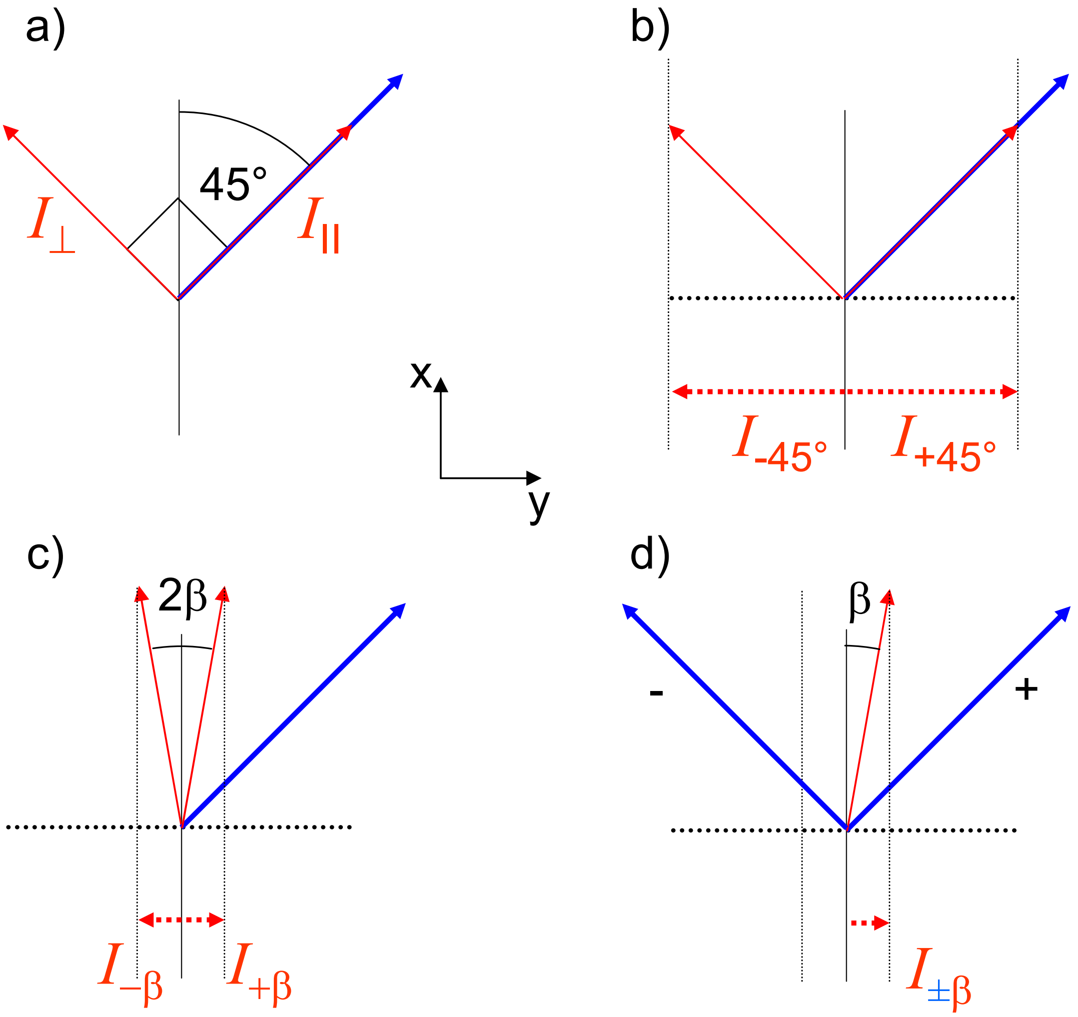

Figure 6.1: Polarizations of pump (blue) and probe (red) beams in conventional LD and anisotropy measurements (a). The same LD and anisotropy signals can be measured when the horizontal projections of the probe beam is singled out by a polarizer (dotted line) behind the sample (b). They are enhanced when the angle β between the vertical axis and the probe polarizations is made smaller(c). Alternatively, the probe polarization can be fixed at an angle β, and the pump polarization can be varied between ±45° (d).

intensities measured at $\pm\beta$). We found that :

$$\Delta A_{\pm} = \frac{1}{\ln(10)} \left(\overline{A} \pm LD \cot \beta \right) \tag{6.2}$$

and :

$$\begin{aligned} s &= \Delta A_{+} - \Delta A_{-} \\ &= \frac{2}{ln(10)} LD \cot \beta \end{aligned} \tag{6.3}$$

In contrast to earlier implementations of the technique in electronic spectroscopy, which involved separate measurements for each probe polarization, we use fast polarization modulation in order to continuously switch between angles $\pm\beta$ with the help of a photoelastic modulator (PEM, see section 2.4.3), and we explore different experimental arrangements. The advantages of using a PEM to modulate polarization of ultrashort mid-IR laser pulses have been demonstrated earlier in our group in the context of transient vibrational circular dichroism spectroscopy [56]. Here it allows us to change the linear polarization state of the probe or pump beam at the kHz repetition rate of our set-up and to measure within two successive shots the amplified LD signal. We demonstrate that we can amplify the LD signal by more than one order of magnitude without increasing noise. Furthermore we discuss the possibility to separate overlapping vibrational bands with different anisotropy by recording transient spectra at different polarizer angles . The method also allows us to record highly amplified transient absorption data on timescales shorter than the rotational diffusion time. Angles between transition dipoles can also be measured with a better accuracy. This makes the crossed polarizer method particularly well-suited for ultrafast vibrational spectroscopy where tiny signals are very common.

6.1 Experimental

The experimental configuration used is the one described in section 2.4.1. The probe light polarization in the spectrometer was set perpendicular to the lines of the grating, to ensure a better transmission. In this regard, the spectrometer acts as an additional but low extinction ratio polarizer(r>0.5) and its effect on the signals was neglected.

Three equivalent experimental arrangements of polarizers and PEM are shown in Fig 6.2. Arrangement 6.2a is a direct adaptation of the method used in ref. [97] and corresponds exactly to the polarization scheme of Fig. 6.1c. The UV-pump pulse with linear polarization at 45° with respect to the laboratory x-axis, given by the optical axis of the PEM, excites the sample. It is followed by a mid-IR probe pulse, whose polarization is initially set at an angle β by the first polarizer LP1. For every second laser pulse the PEM acts as a $\lambda/2$ plate and rotates the plane of polarization to $-\beta$. When the sample is isotropic, identical small projections of these probe pulses are transmitted by the second linear polarizer LP2 that is oriented perpendicular to the PEM axis. In practice, it is however of advantage to use the arrangement shown in Fig 6.2b, where the order of optical elements in the probe beam is reversed.

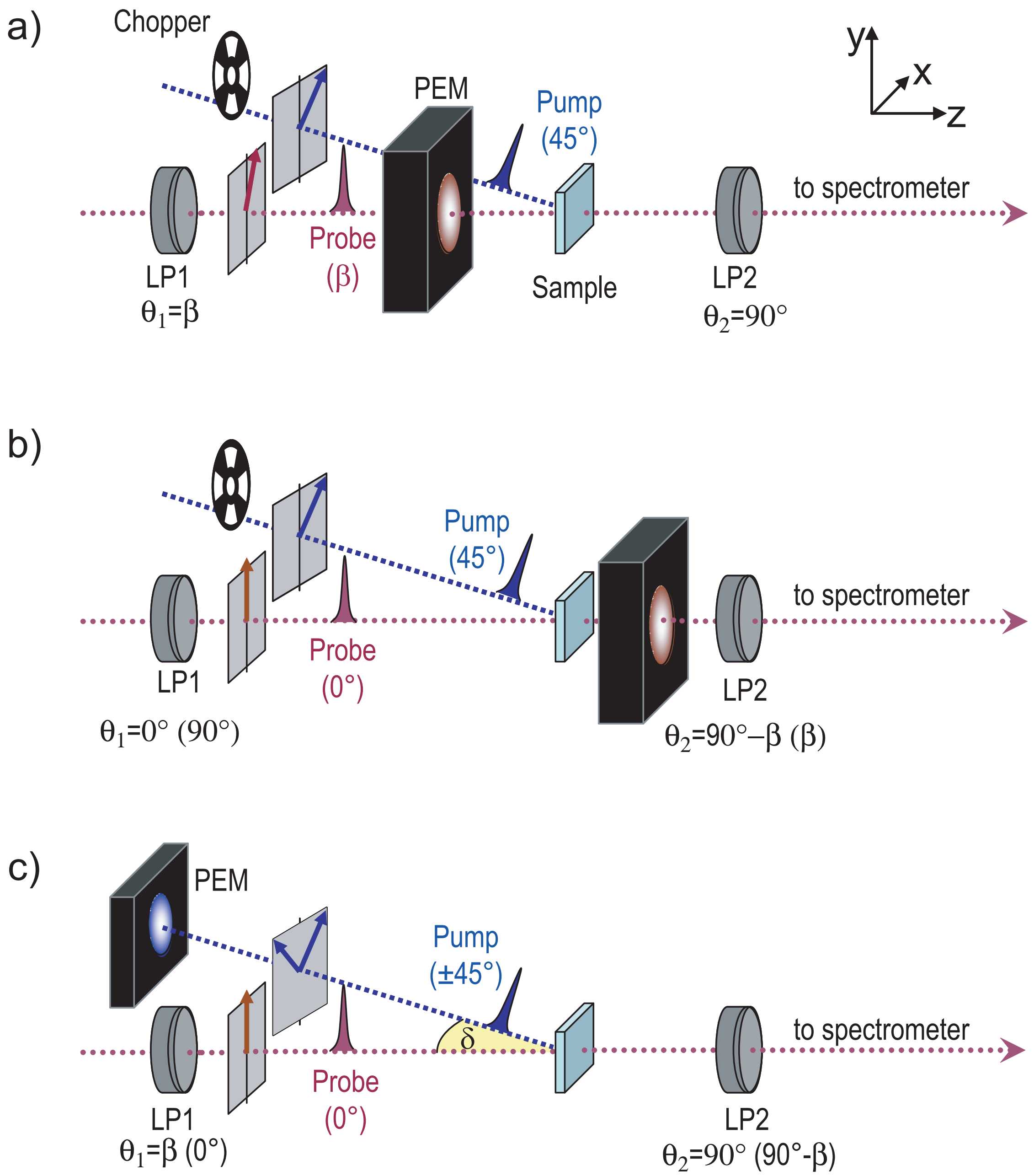

Figure 6.2: Three equivalent experimental arrangements for the recording of the enhanced transient linear dichroism signals using photo elastic modulators (PEM). a) Probe beam polarization modulation before the sample, b) Probe beam polarization modulation behind the sample, c) Pump-beam polarization modulation. The axis orientation of linear polarizers LP1 and LP2 is indicated below the polarizers, the values in parenthesis correspond to equivalent alternative of orientations. The angle δ between pump and probe beams can be taken into account in the response (see section 5.5.7)

This leads to identical transient absorption signals and linear dichroism enhancement. Method b) facilitates the alignment of LP1 (the polarizer is rotated until the probe pulse polarization coincides exactly with the optical axis of the PEM, i.e. the transmitted intensities for all modulator states in the absence of the pump beam are equal). It also allows us to place the PEM very close to the focal spot of the probe beam (immediately behind the sample), which strongly reduces artefacts arising from lensing effects.

As a third alternative we have also used a PEM for UV and visible light to modulate the pump pulse polarization between ±45°, keeping the probe-polarization fixed as shown in Fig. 6.2c. This further reduces noise and simplifies the alignment of the probe beam.

6.2 Sample

The sample we used for demonstrating the method is a photoswitch of the N-alkylated Schiff base family [27,76] [4-(6-Methoxy-2,2-dimethyl-3,4-dihydro-2H-naphthalen-1-ylidene)-1,5 dimethyl-3,4-dihydro-2H-pyrrolium see Fig. 6.3]. The details of its synthesis can be found in the supplementary information of [29]. These photoswitches isomerize from cis (Z) to trans (E) after excitation in the near UV, and isomerizes back to trans in a few seconds at room temperature. Isomerization is ultrafast (return to the ground state in less than 1 ps), efficient ($\geq 20\%$) and the switches are robust under illumination [101].

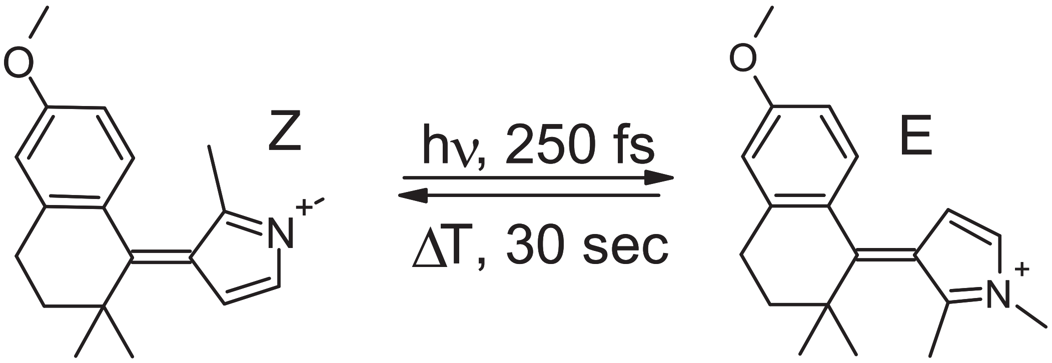

Figure 6.3: The cis and trans form of the MeO-NAIP photoswitch.

We choose this N-alkylated Schiff base switch because the E isomers generated by the pump pulse relax within a few seconds back to Z at room temperature, as he ground state barrier is only 22. 4 (+/-2) kcal. mol^{-1}. We could therefore use this molecule dissolved in deuterated methanol in a flow cell over long time-periods without a change in the composition of the sample (nearly 100% Z).

The FTIR spectrum shows two main bands in the spectral range between 1500 cm^{-1} and 1700 cm^{-1}. The first one centred at 1566 cm^{-1} is related to a mode involving mainly stretching of the isomerizing C=C bond, and the second one around 1604 cm^{-1} involves ring modes on the benzene ring (from normal mode calculations on the B3LYP level, Gaussian program suite [75]). The shoulders near 1550 cm^{-1} and 1620 cm^{-1} could not be uniquely assigned but are probably related to delocalized modes involving CH_3 bending.

6.3 Results

In Fig. 6.4b we present transient absorption spectra $\Delta A_{\parallel}$ and $\Delta A_{\perp}$ from a conventional (no polarizer in probe beam) measurement with parallel and perpendicular pump and probe pulses at a delay of 500 fs. At this delay artefacts due to pulse overlap or a Kerr effect can be excluded. A fraction of the molecules has already decayed back to the (hot)electronic ground state, but

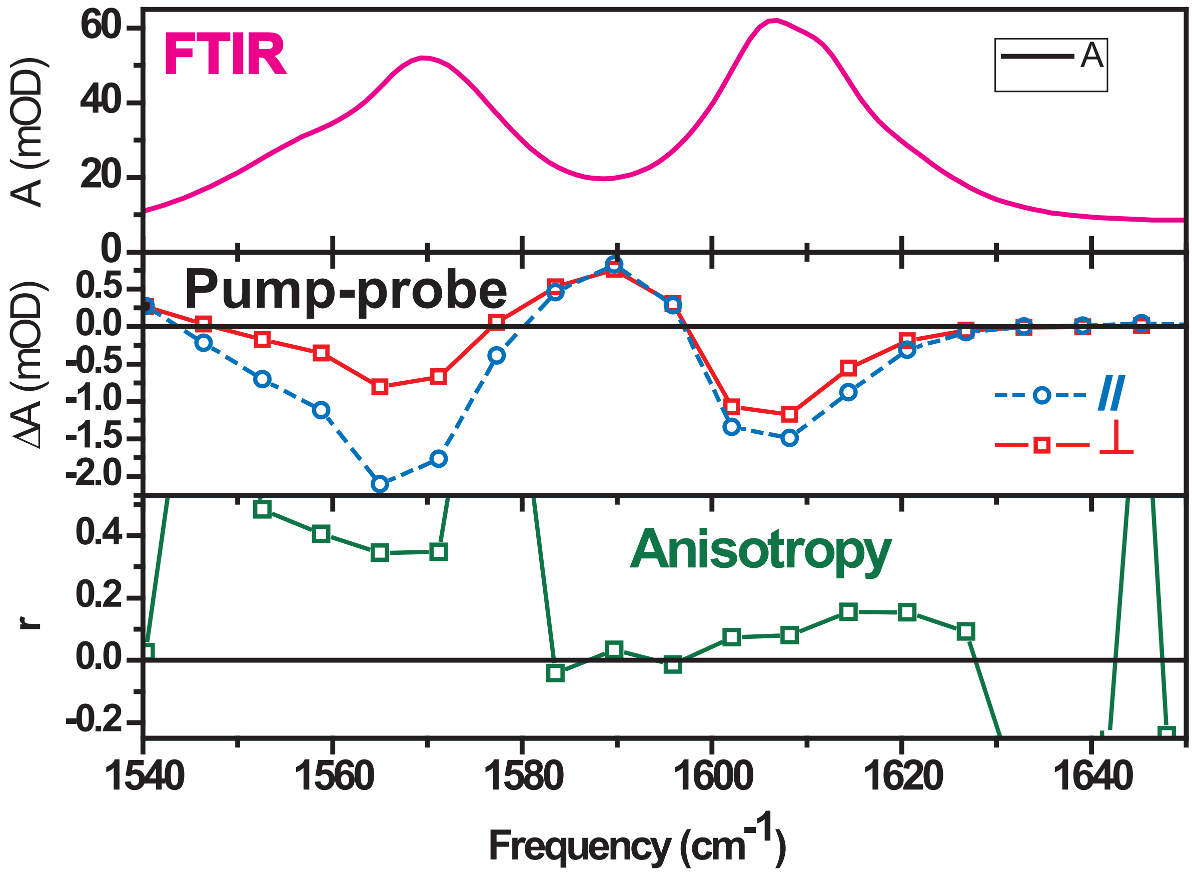

Figure 6.4: a) FTIR spectrum of the Z-isomer of the N-alkylated Schiff base photoswitch. b) Transient absorption changes 500fs after excitation at 400 nm for parallel and perpendicular pump and probe polarizations. c) Anisotropy calculated from the two spectra in b).

the bleach of the Z-isomer vibrational bands is almost identical to that seen at earlier delays. Part c) of the same figure shows the corresponding anisotropies (using Eq. 5.2). From these we can calculate the angles between the electronic transition dipole and the IR transition dipole of the individual modes, which are summarized in Table 6.1.

Mode	C=C	ESA	Ring mode
Frequency	1566 cm^{-1}	1585 cm^{-1}	1604 cm^{-1}
Anisotropy	0. 35-0. 4	-0. 05-0. 05	0. 06-0. 16
Angles	0°-15°	50°-60°	39°-49°
$\|\beta_0\|$	23°-25°	6°-9°	11.5°-12.5°
Angles	14°-19°	44°-48°	36°-40°

Table 6.1: Experimental anisotropies, polarizer angles $|\beta_0|$, and corresponding intramolecular angles ω between the electronic transition dipole moment and the vibrational transition dipole moments.

The vibrational transition dipole of the C=C stretch mode is nearly parallel to the electronic transition dipole, as expected for a charge translocation across the isomerizing C=C bond [27]. The benzene ring mode has a much smaller anisotropy, yielding an angle around 39-49°. The positive signal around 1585 cm^{-1} is due to ring modes of molecules in the S_1 excited state as well as molecules which have already returned to the hot ground state in either the original Z or the E configuration. The anisotropy of this signal appears to be approximately zero corresponding to an angle near 55°. The anisotropy is increasing between 1590 cm^{-1} and 1620 cm^{-1} due to the overlap between this signal and ground state bleaching of the ring mode at 1604 cm^{-1}. Indeed, when 2 bands with different anisotropies overlap, the anisotropy in the overlapping region is varying between the anisotropy values of the 2 bands.

In Fig. 6.5a and b we show the transient signals $\Delta A_{\pm}$ (defined in section 5) at the same pump-probe delay, recorded with the set-up of Fig. 6.2b for four different analyzer angles between 3° and 45°. The pump polarization was fixed and pairs of spectra for $\pm\beta$ were measured quasi simultaneously with fast modulation of the probe polarization. The signals for $\beta = \pm 45°$ (blue) are very similar to the ones in Fig. 6.4, obtained with the standard method without polarizers. For smaller analyzer angles, on the other hand, there are significant deviations, due to a different amplification of the different bands as discussed below. In particular, the signal ΔA_+ in Fig. 6.5a changes sign, and the higher frequency bands are almost completely eliminated near $\beta = 10°$ (red). For all angles except 3°, the light intensities on the detector were kept similar by removing filters from the probe beam. For 3°, however, it was approximately two times smaller, leading to a similar signal to noise ratio as for $\beta = 5°$. Fig. 6.5c shows the normalized LD signals, given by the difference of the spectra shown in parts a) and b). As predicted by Eq. 6.3 they are identical up to a scaling factor $\cot\beta$.

When only the enhanced LD signal s is needed, it can be measured with even higher sensitivity when the chopper is removed from the pump beam and Eq. 6.1 is evaluated directly from consecutive measurements with alternating pump or probe polarizations. This is illustrated in Fig. 6.6, where we show data obtained with the set-up of Fig. 6.2c, i. e. by modulating the pump-pulse polarization between ±45° with a fixed horizontal orientation of analyzer LP2 and an incident probe polarization angle β. For simplicity we still label the corresponding intensities $I_{\pm\beta}$ as defined in Fig. 6.1d. Sample and pump-probe delay are the same as in Figs. 6.4 and 6.5, but the UV-pump beam was approximately 20 times weaker, in order to minimize saturation effects and reduce the (unamplified) LD close to our noise limit. Without the additional attenuation by the PEM in the mid-IR probe beam, smaller angles β between polarizers are possible before the light level at the detector becomes limiting.

The plot of the normalized signal to noise ratio at the peak of the main bleach signal near 1566 cm^{-1} in Fig. 6.6b shows that the data quality could now be improved up to signal amplification factors close to 15 ($\beta = 3°$).

6.3.1 Background suppression

To illustrate the ability of our set-up to suppress isotropic background, we show in Fig. 6.7b) the pump-probe spectra of the CN stretch bound to myoglobin in heavy water, previously recorded in our laboratory [102]. The spectra are affected by a strong time dependent background, which perturbs the analysis of the signals. This isotropic background is attributed to a temperature rise in the solvent, due to the energy transfer from the solute to the surrounding solvent molecule.

In Fig. 6.7a), we show the spectra obtained using our set-up with fast modulation of the pump polarization (set-up 6.2c)). The background contribution are suppressed by our methods, which facilitate the interpretation of the spectra and leads to better dynamics.

6.4 Discussion

6.4.1 Information Content

When $\Delta A_{\pm}$ is measured at different relative polarizer orientations, the intramolecular angle ω can thus be determined from the angle at which the signal vanishes, which is independent of

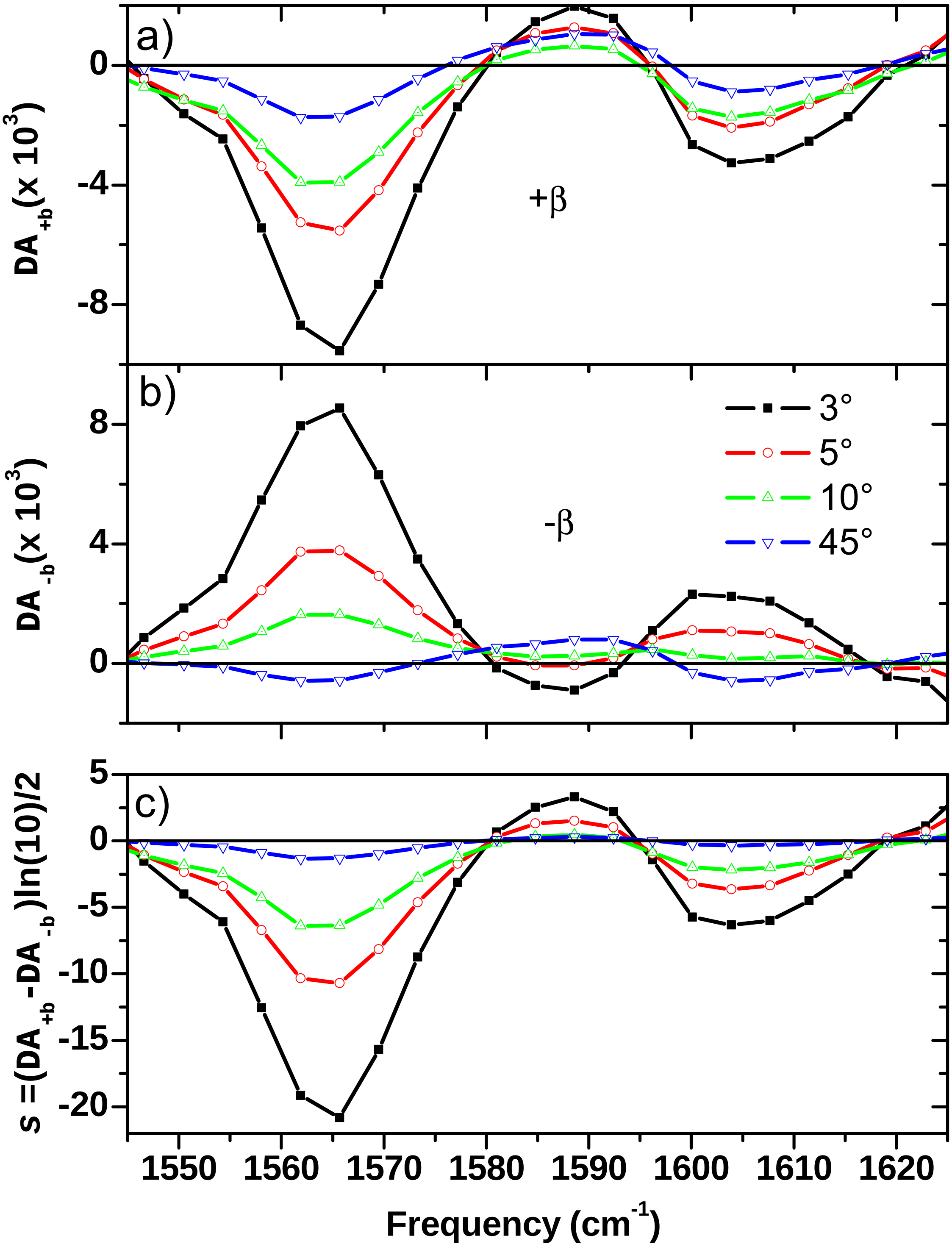

Figure 6.5: a) and b) Amplified transient absorption signals $\Delta A_\pm$ for different probe angles (polarizer orientations) β, recorded using set-up Fig. 6.6b, 500 fs after 400 nm excitation. c) Enhanced LD signal s.

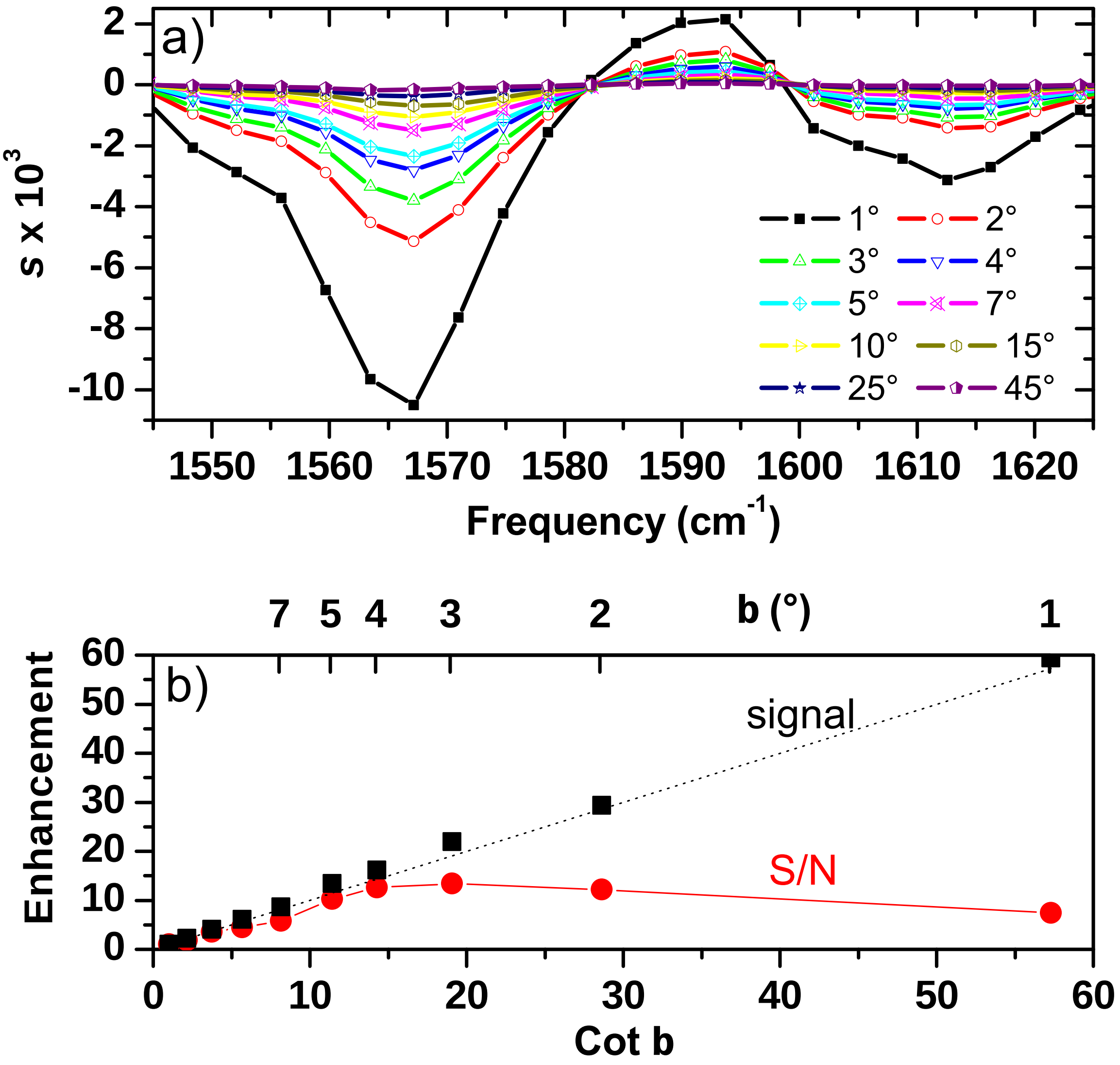

Figure 6.6: a) Enhanced LD signal s recorded by fast modulation of the UV-pump pulse polarization (setup Fig. 6.6c), 500 fs after 400 nm excitation. b) Enhancement of the signal (squares) and signal to noise ratio S/N (circles) as a function of polarizer orientation β. Both are normalized to 1 at $\beta = 45°$.

the absorbance change. We presented already in 5.4 how to deduce ω from the signals. Fig. 6.8 shows the linear fits (Eq. 5.26) to the peak signals in Fig. 6.5 as a function of $\cot\beta$; the extracted angles are compared to the analysis of the conventional anisotropy measurements in Table 6.1. When the average absorption change $\overline{A}$ is negative (bleach or stimulated emission) the ΔA_+ signal changes sign and grows positive if the angle between transition dipoles is smaller than magic angle $\omega_{mag} \approx 54.7°$; if $\omega > \omega_{mag}$, on the other hand, ΔA_- changes sign. For a positive absorption change, it is the other way round. Consequently, signals arising from vibrations with a transition dipole moment at magic angle with respect to the electronic transition dipole

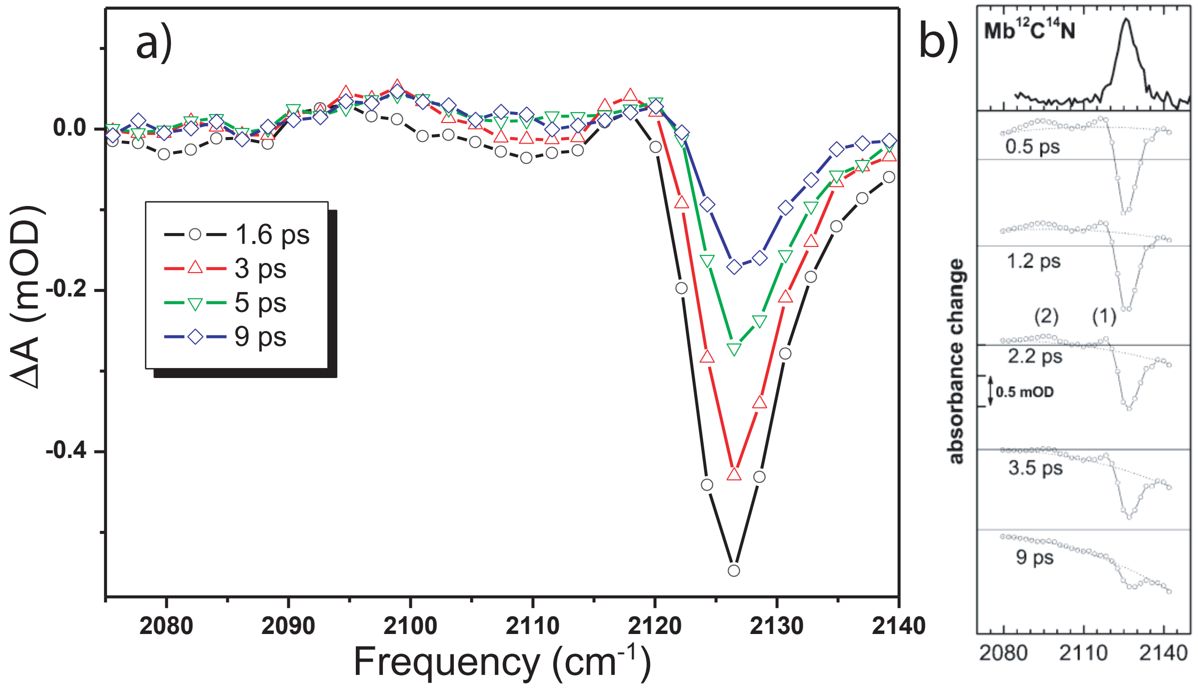

Figure 6.7: Pump-probe spectra of the CN stretch in myoglobin using a) set-up 6.2c) and b) old pump-probe set-up.

moment are not enhanced when β is reduced. This is also the case for isotropic background signals, for example due to pump-induced temperature changes in the solvent.

Angles can this way be determined more accurately than with the conventional anisotropy measurements, as discussed in section 5.4. It is interesting to notice that we can now determine angles even with samples which exhibit very low absorbance. By scanning β is also possible to gain accuracy, in a way similar to Lee et al. [48] in 2D IR spectroscopy [1].

Furthermore, for a suitable choice of $\beta = \beta_0$, specific absorption bands can be eliminated from the transient spectra ΔA_+ or ΔA_-, yielding a clearer view of neighbouring spectral features or resolving overlapping bands with different anisotropies. This can of course also be achieved by a weighted subtraction of spectra recorded for parallel and perpendicular polarization in conventional anisotropy measurements. With the crossed polarizer techniques, however, band elimination is possible in a single measurement, thereby significantly reducing uncertainties due to noise and background. Also note that fast polarization modulation is not necessary in this case.

To our opinion, however, the most useful signal for ultrafast vibrational spectroscopy is the enhanced linear dichroism signal s itself, which carries most of the information of regular pump-probe data, but can be measured with more than one order of magnitude better signal to noise (or a hundred times faster). While this signal decays to zero with rotational diffusion, many of the interesting processes addressed by ultrafast spectroscopy like photoisomerization,

---

[1] Note that in our discussion in ref [29] we neglected the symmetry of the problem. Considering $\Delta A_\pm$ signals separately, we wrongly stated that measurements with only little amplification were always necessary in order to reliably determine β_0. We therefore concluded that our approach constituted only a modest improvement when compared to conventional anisotropy method of comparing parallel and perpendicular probing. This is actually not true and this method can be in fact much more precise for the determination of angles, especially when signal to noise is small or near magic angle, where the usual anisotropy measurements fail because of the term $A_\parallel - A_\perp$.

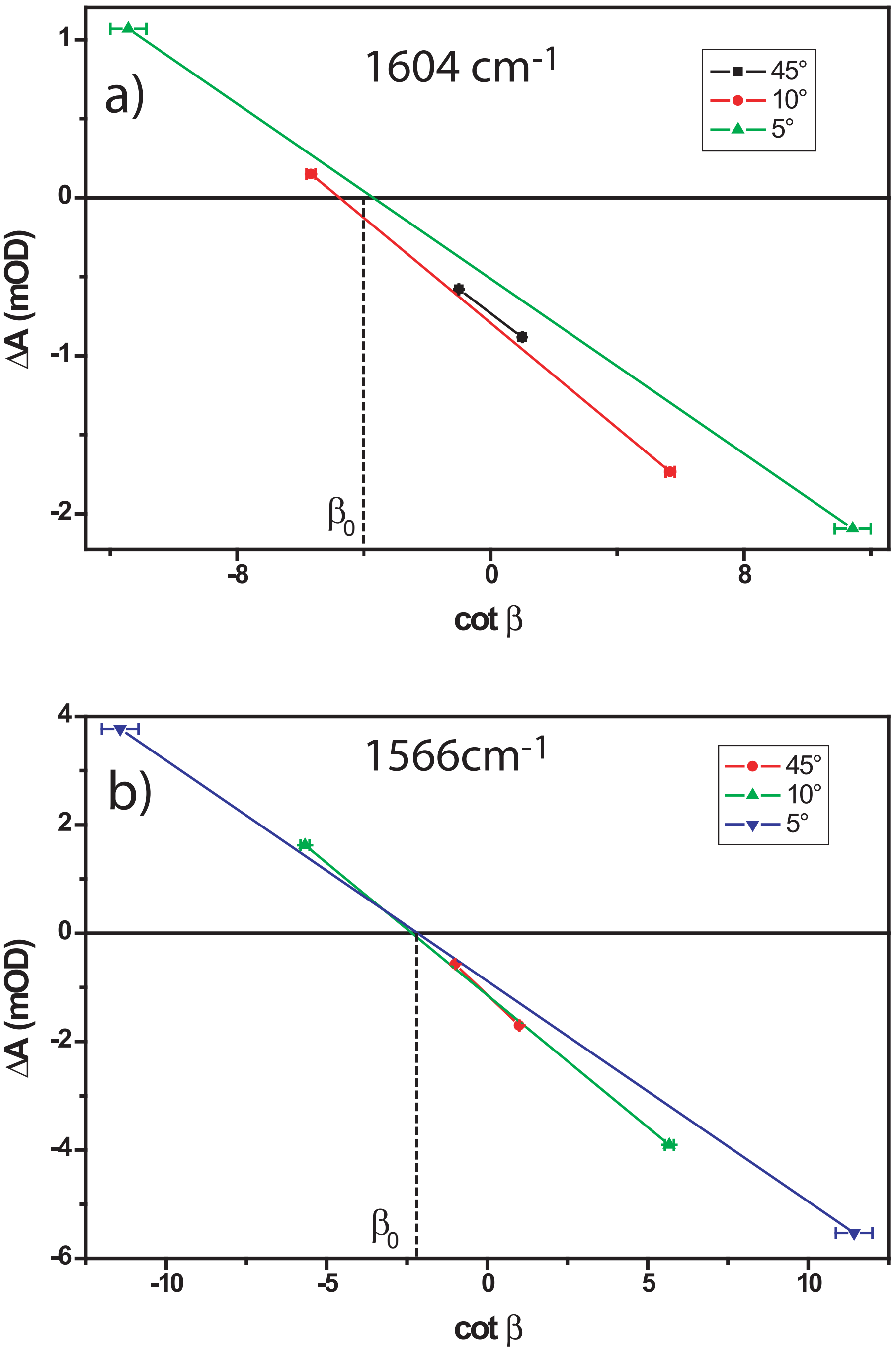

Figure 6.8: β-dependence of the transient absorption signals $\Delta A_{\pm}$, shown in Fig. 6.5 for the bleach signals around a) 1604 cm^{-1} and b) 1566 nm^{-1} for the bleach. The value of β_0 from the different linear lines connecting two points with opposite amplification are used to determine ω in table 6.1. The data with more amplification (β=3°) are affected by a too important uncertainty on β and are not shown here.

bond-breaking and intramolecular energy transport take place on a much faster timescale and can be fully captured by the enhanced LD signal. Even much slower processes can be studied in proteins, membranes or other media that slow down the anisotropy decay. The enhanced LD signal can also be evaluated directly from two consecutive intensity measurements without the need of a chopper in the pump beam. This doubles the effective number of averages in a given time interval, and allows us to fully exploit correlations in laser intensity fluctuations. Indeed, we found that the quality of the LD data recorded without chopper is significantly better than the equivalent difference of the signals ΔA_+ and ΔA_-, measured quasi simultaneously with a chopper repeatedly blocking and transmitting four consecutive pump-pulses, even when the latter data set is averaged twice as long.

6.4.2 Limitations

We already identified different reason that can limit the amplification of the signals (section 5.5), which are the intensity of the probe light,the extinction ratio of the polarizers, and the size of the LD and LB.

The implementation of enhanced LD spectroscopy in the mid-IR has so far probably been held back by the poor performance of detectors and the need for sufficiently good polarizers. Detector efficiency is important because the probe light transmitted by the second polarizer is only a small fraction of the incoming light, decreasing from ideally 50% to 0.3% when β is reduced from 45° to 3°. In our set-up, despite probe pulse energies close to 2 μJ, even lower transmission can no longer be compensated by the removal of filters from the probe beam. Low light intensity at the detector leads to a significant increase in noise and currently limits the signal enhancement factor we can achieve to approximately 20-40, depending also on the solvent absorption.

A second limitation in the mid-IR can be the quality of polarizers. Our free-standing wire-grid polarizers (Infraspecs, PO3 model) have an extinction ratio of 10^{-4} but suffer from spatial inhomogeneity, which can lead to artefacts. With home-built polarizers based on Brewster angle reflection [51] we reach an extinction ratio of $\approx 10^{-7}$ but these are bulky and have a maximum transmission of only 38%. More common substrate supported wire grid polarizers with $r = 10^{-2}$, on the other hand, severely limit the maximum possible signal amplification, which occurs at an angle between polarizers $\beta_{max} \approx \sqrt{2r}$, corresponding to an enhanced LD signal [97] $s_{max} \approx LD/(2\sqrt{2r})$ (see section 5.5).

The effect of Linear Birefringence (LB) induced by the pump is not taken into account in the development of our signal. Indeed, as the pump changes the absorption, it also affect the refractive index and induces a LB that contributes to the signal. With the analysis with Jones matrices, we found out that the LB is affecting the spectra taken at +/-45°, but cancels out when we subtract these 2 signals (see 5.36). Moreover,in our case (absorbance changes of about 1 mOD), it has a significant incidence only on signals which are not amplified (i. e. with anisotropy zero) and for amplification angle of less than 2 degrees.

Here, the LD size ($\approx 10^{-3}$) is too small to see the saturation effect discussed in section 5.5.4.

The amplified LD signals can not distinguish between population relaxation and reorientation dynamics (when magic angle measurements and anisotropy do). However, when population dynamics and reorientation dynamics occur on different timescales, the ability to amplify signals for example long after vibrational cooling processes could be taken as an advantage to measure the reorientation constant with better accuracy on small signals.

6.4.3 Fast polarization modulation

The measurements presented here do not necessarily require the fast switching of pump or probe polarization states by a PEM and can be realized with much less experimental effort without it. Nevertheless, fast polarization modulation affords a significant signal to noise improvement already in conventional anisotropy measurements. At the same time, however, a PEM can lead to additional artefact signals, in particular when placed into the probe beam as in set-ups a and b of Fig. 6.2.

First, a retardation of $\lambda/2$ can be produced by the PEM only for one specific wavelength, at higher or lower frequencies the polarization state will be slightly elliptical. This is less critical for the visible or UV-pump pulses which typically have a much narrower relative bandwidth. Second, a small static birefringence of the PEM breaks the symmetry between $\pm\lambda/2$ modulation, corresponding to maximum expansion or contraction of the modulator crystal. Since in both states the PEM ideally rotates an incoming polarization into the same plane, we compensate for this effect by averaging the corresponding signals. This reduces the chopper frequency for measurements of $\Delta A_{\pm}$ to one eighth of the laser repetition rate, as four signals (PEM inactive, expanded, contracted, inactive, see Fig. 6.2d) have to be recorded consecutively. Since the refractive index changes in a PEM crystal peak at the center and drop to zero at the edges, at maximum expansion and contraction the PEM also acts as a positive, respectively negative lens with a focal length of 60-80 meters (depending on the size of the crystal). The size of the beam at the array detector is thereby modulated, which can lead to intensity changes and spectral shifts. Placing the PEM close to the focal point of the mid-IR probe beam strongly reduces this effect (one of the main advantages of the arrangement in Fig. 6.2b over that in Fig. 6.2a). In contrast, the corresponding modulation of the focal spot size of the UV-pump beam at the sample in the experimental arrangement shown in Fig. 6.2c has a negligible effect on the data, especially after averaging the signals recorded with $\pm\lambda/2$ modulation.

In summary, fast modulation of the pump-pulse polarization is clearly superior to modulating the mid-IR probe light in crossed-polarizer enhanced ultrafast LD spectroscopy. On the other hand, the set-up b in Fig. 6.2 can be directly used for (transient) vibrational circular birefringence measurements [103, 104] (for which it was originally designed) by aligning the planes of polarization of pump and probe beams.

6.5 Conclusion

In this chapter, we have demonstrated different experimental arrangements for measuring transient absorption changes and LD in ultrafast mid-IR pump-probe experiments with highly improved sensitivity, using a crossed polarizer method. Signal amplification by more than one order of magnitude was achieved at constant noise. Even larger amplification factors, as have been previously reported for electronic spectroscopy, are possible but require both better detectors or higher probe pulse intensities and polarizers with extinction ratios better than 10^{-4}.

The crossed polarizer technique is particularly powerful when combined with fast polarization modulation using photo elastic modulators. Equivalent signals can be measured with either pump or probe polarization modulation, however, the latter is more sensitive to artefacts. Here we used both to detect enhanced LD signals after the photoexcitation of a photoswitch of the N-alkylated Schiff base family and determined the angles between electronic and vibrational transition dipole moments with improved accuracy. It was equally possible to eliminate individual spectral features at certain relative polarizer angles in a single measurement.

The technique is expected to become most useful for the amplification of transient signals from samples exhibiting very low absorbance changes. Since signal amplification is proportional to the pump-induced linear dichroism, only bands with a well defined orientation of their transition dipole moment are significantly enhanced, while solvent and other background signals as well as birefringence contribution are suppressed. This will strongly facilitate the study of light-induced structural changes at much lower concentrations than typically required in conventional transient mid-IR spectroscopy, a perspective particularly attractive for biological samples. Recently, Donaldson et al. have demonstrated similar amplification of pump-probe signals with a UV/Visible transient grating spectrometer that uses a heterodyne detected infrared probe [105]. This technique requires a customized optical layout to handle phase locked pairs of pump and IR pulses, which make it more challenging to set-up, whereas our method can be implemented easily in any pump-probe set-up. The amplification in the transient grating method does however not rely on the anisotropic component of the signal, as it measures also amplified isotropic signals, so it is applicable to a wider range of measurements compared to our technique.

The possibility to measure angles with better accuracy is also attracting for those who want to compare experimental results and theoretical predictions. The possibility to follow angle change in time is also attractive, as the gain of sensitivity in angle values could lead to more detailed structure changes (see chapter 4).

Our technique for modulating the polarization of mid-IR pulses will also be useful in analogous all-IR pump-probe or 2D-IR experiments [106]. A closely related experiment has in fact already been performed by Xiong and Zanni, who could enhance signals significantly by placing a polarizer into the probe beam in a 2D-IR experiment with collinear pump-beams of perpendicular polarization [107]. The extension of the same measurement principle to 2D-IR spectroscopy is the purpose of chapter 7. The application to other frequencies or higher order spectroscopies is possible and will be discussed in the outline of this thesis.

Chapter 7

Linear dichroism enhancement in 2D-IR spectroscopy

We already demonstrated that the quasi crossed polarizer technique is useful to increase S/N and angle determination in a pump probe experiment. Here we apply the same principle to 2D-IR spectroscopy in the pump-probe geometry, which is one of the most easy way to perform 2D spectroscopy. The pump-probe geometry was used for the first demonstration of 2D-IR spectroscopy in the frequency domain [108]. In the time domain, this geometry is also interesting [38], and has become popular also with the use of pulse shapers in the pump beam to record 2D-IR spectra [39, 98] as well as 2D visible spectra [109].

The idea of placing a polarizer in the probe beam after sample to increase signal to noise ratio in 2D-IR spectroscopy was first published by the group of Prof. Zanni [107]. They showed that they can suppress background contribution from 2D spectra by using perpendicular pump pulses and a polarizer in the probe beam, measuring the polarization sequences of the type $< XYXY >$ or $< YXXY >$.

In this chapter, we develop this idea further and outline the close relationship between this form of 2D-IR signal amplification and linear dichroism experiments. For the latter, the explicit dependence of the signal on experimental parameters (polarizer alignment and quality, signal size, etc.) has already been derived in detail in chapter 1. We build on those results to demonstrate the full potential and some limitations of the method in 2D-IR spectroscopy. In particular, we discuss the complete suppression of scattering contributions and the precise determination of angles between transition dipole moment. Also, the flexibility of the technique is demonstrated by measuring dispersive spectra and by being able to deduce rephasing and non-rephasing spectra, that were obtainable before only with the four wave mixing geometry.

7.1 Experiment

We used the 2D-IR set-up presented in chapter 2 and described in detail in [40]. The pump-pulse pair goes through a computer-controlled $\lambda/2$ plate, changing the polarisation between ±45° with respect to the laboratory X-Axis (vertical) every 20 scans of the interferometer (≈ 1 second/ scan). In order to reach maximum signal amplification, an intense probe beam, centred at the same frequency, was produced by a second optical parametric amplifier (OPA), which doubled the available laser power ($\approx 2 \times 2\mu$J per pulse. Before reaching the sample, the pump beam passed a wiregrid polariser (LP1) with extinction ratio $\approx 10^{-4}$, oriented at an angle β from the X-axis. An identical wire grid polariser (LP2), oriented in the Y-direction, attenuated the probe beam before the spectrometer and the detector. We used a waveplate in front of LP1 to maintain constant light intensity at the sample for all angles β. Changing β thus only modified the amplitude of E_{LO}, while E_3 and the signal field E_S^y intensity remained constant. For large angles β, and when the LO was too large and saturated the detector, we used neutral

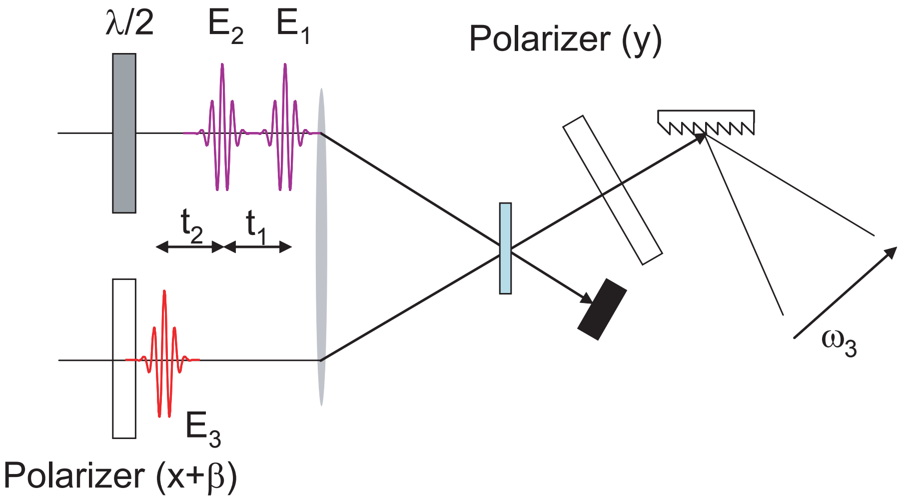

Figure 7.1: Schematic representation of the set-up. The probe beam passes through a first polariser LP1 set at an angle β relative to the X axis, behind the sample it passes through the second polariser LP2 oriented along the Y axis. The polarisation of the pair of pump pulses is changed with a half wave plate $\frac{\lambda}{2}$ between ±45°.

density filter to lower its intensity, affecting the signal field E_S^y at the same time.

To illustrate the method, we measured the 2D spectra of Rhenium-carbonyl complex [Re(CO$_3$)(dmpby)Br], in the region where the C=O stretching modes absorb (1860-2060 cm^{-1}) (Fig. 7.2). The ground state bands at 1889 cm^{-1}, 1910 cm^{-1}, and 2018 cm^{-1} have been assigned to a'(2) antisymmetric stretching of axial CO and equatorial COs, a" antisymmetric stretching of equatorial COs and a'(1) symmetric stretching of all COs modes, respectively. For the spectra of Fig. 7.3, the population time was t$_2$ =20 ps and we scanned coherence time to t$_1$ = 4000 fs.In the spectra of Fig. 7.7 and Fig. 7.6, the population time was 1 ps.

7.2 Amplification and angle determination

In Fig. 7.3 we represent a selection of 2D-IR spectra of the individual signals $\Delta A_{\pm}$ and their difference, taken at the four different angles $\beta = 2°, 5°, 10°$ and 45°. First, the 2D spectra measured at ±45° correspond to the usual parallel A$_{\|}$ and perpendicular A$_{\perp}$ signals. As expected, they are more intense than their difference S. The cross peaks are also more intense in the perpendicular case, as expected for an angle close to 90°.

From the scale and the spectra S at different β angles, we observe first that the spectra are - as expected from Eq.(5.15) - amplified when β is decreased. In particular, the difference spectra S do not change shape and are only amplified. The amplification factors match well the expected ones from Eq.(5.15) on except for $\beta = 2°$, where it is lower than expected (25 instead of 28). This is due to imperfect polariser and is expected to happen when angles are smaller than 3° in our case [29]. We can already observe that the cross peaks in S have reversed sign in comparison to A$_+$ and A$_-$. This is already an indication that these cross peak have a negative anisotropy, and involve dipoles with angles greater than magic angle.

We see that for A$_+$ at $\beta \approx 10°$, the cross peaks vanish from the spectra. This happens when $\overline{A} = LDcot\beta$. At this population time of 20 ps, rotational diffusion has already occurred, and we can not conclude anything about angles between transition dipoles. This fact will be later exploited for shorter population time (see Fig. 7.4).

The cross peak then reappear when β gets smaller, but with reversed sign. This is seen in

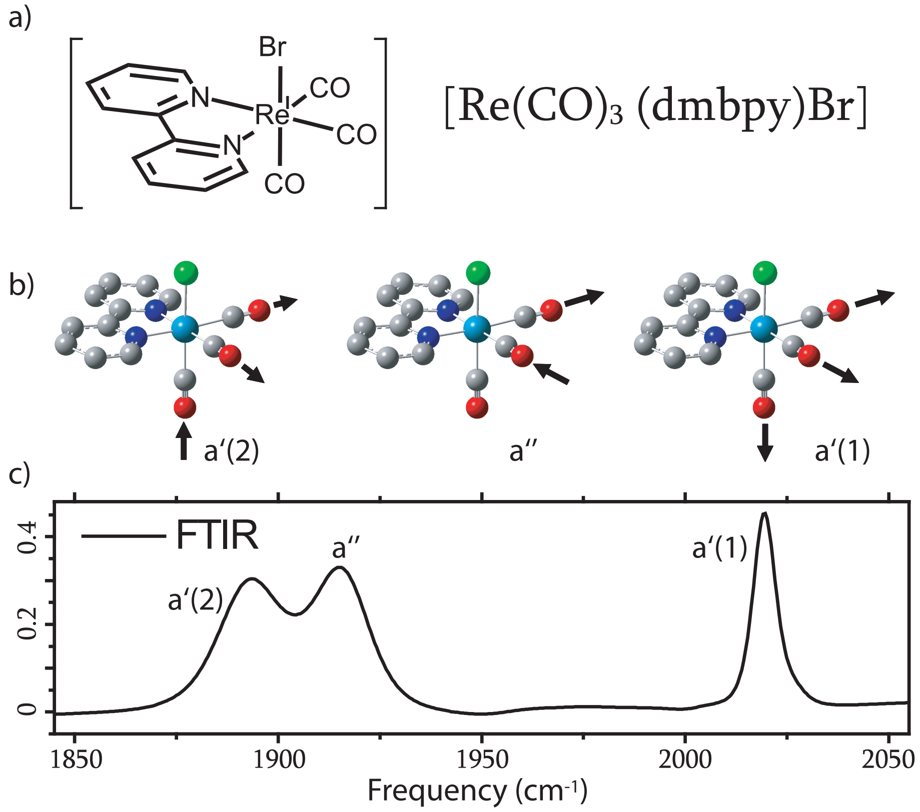

Figure 7.2: a)Chemical structure of the [Re(CO_3) (dmpby)Br] complex. b)The 3 normal mode of CO stretch c) FTIR spectra in DMSO.

the spectra at A_+ for $\beta = 5°$ and $\beta = 2°$. This effect is also present in the A$_-$ spectra for the diagonal peaks, which are reversed when passing from $\beta = 45°$ to $\beta = 10°$.This is an indication that $LD \cot \beta$ is now greater than $\overline{A}$.

Another application of the method is that we can eliminate cross or diagonal peak selectively from A$_\pm$ with only one measurement, by simply setting an appropriate angle β. In Fig. 5.3, we calculated the angle β_0 at which we can eliminate peaks which have a certain anisotropy, or the corresponding internal angle ω. Only isotropic signals can not be suppressed from the individual $A_\pm$, but those are subtracted when calculating their difference. We illustrate this fact in Fig. 7.7a by eliminating the cross peaks from the spectra. We observe first that all cross peaks disappear at the same angle, around 10°, corresponding a calculated angle between normal mode of about 68°. This value is lower than expected due to some rotational diffusion which lowers the anisotropy in time. This elimination can be useful when studying for example diagonal peak lineshapes, or spectral diffusion. In Fig. 7.7b, we also eliminated diagonal peak from spectra. We could not completely eliminate these peaks, as it turned out that eliminating bleaching contribution and excited state absorption did not happen at the same β_0. This can be explain the overlapping with cross peaks on the diagonal, or by slightly different dipole orientation when the vibrator is excited. These peak elimination allows to get cross peak independently from overlapping diagonal peaks, like in the entangled region around 1900 cm^{-1}.

In Fig. 7.4, we plotted the absorption in function of β for different peaks of the measured 2D spectra. The line connecting the measured absorption at $\pm\beta$ crosses the horizontal axis at β_0, that we can use to determine ω. The accuracy on β_0 depends then on the S/N of the measured absorption. The signal to noise increases as β decreases, and the values of β_0 and thus ω are obviously more precise, as the linear fit of two distant point is more accurate than

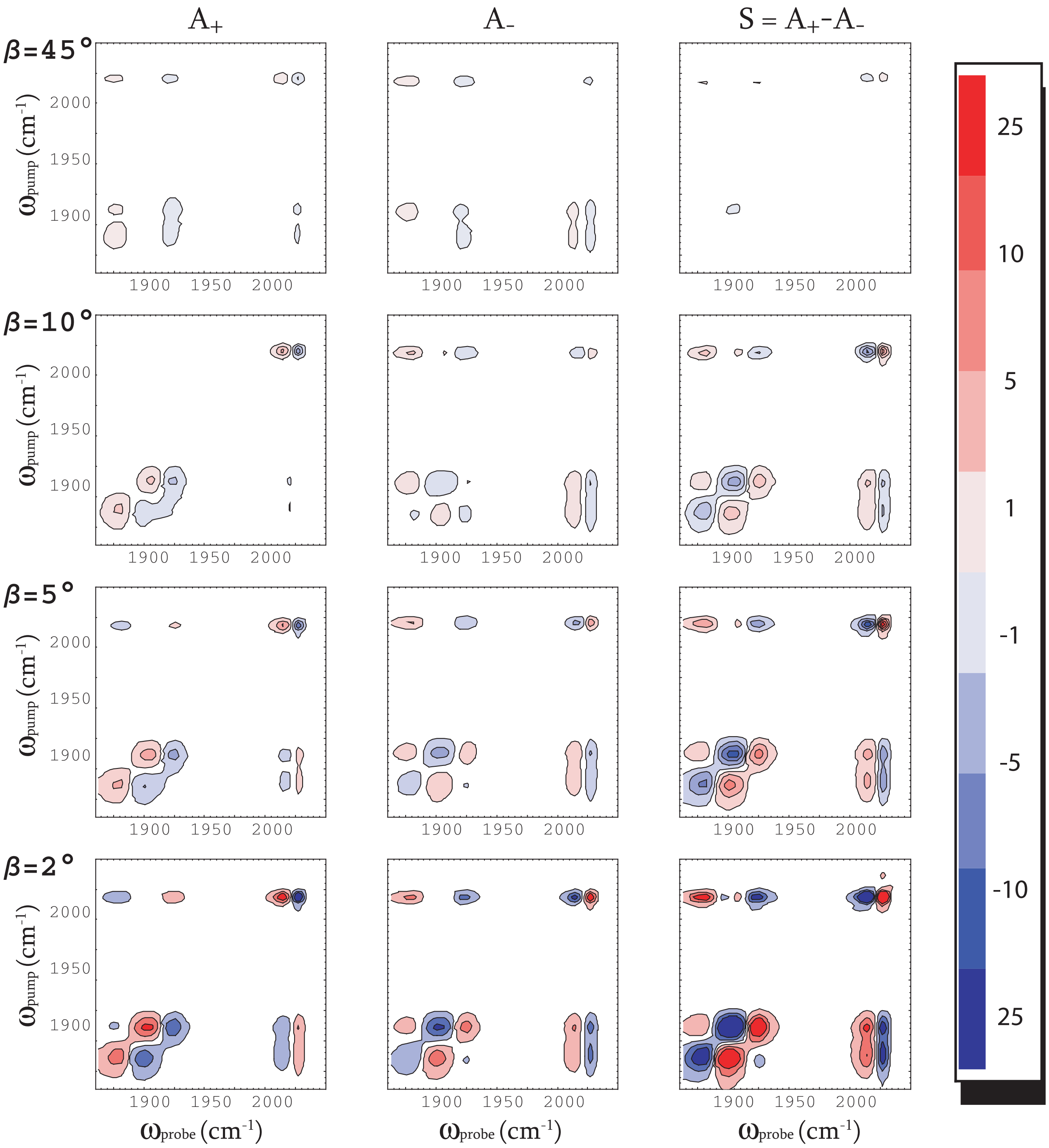

Figure 7.3: 2D spectra of [Re(CO$_3$) (dmpby)Br] for different angles β, at a population time of 20 ps. The first column of spectra represents the absorption ΔA_+, the middle one is the absorption ΔA_- and the right one is the LD component.The scale on the right is normalized to S at $\beta = 2°$, and is shared by spectra of $\Delta A_\pm$. The horizontal axis is the probe axis, while the vertical one is the pump axis.

the same line fitting with two points close to each other and affected by the same noise. The angle found for the diagonal peak 1 is 66°, when the angles for the 2 cross peak gives a value which does not fall into the range of the graph of Fig. 7.7, but is close to $\cot\beta = 3$, which is consistent with an angle $\omega = 90°$.

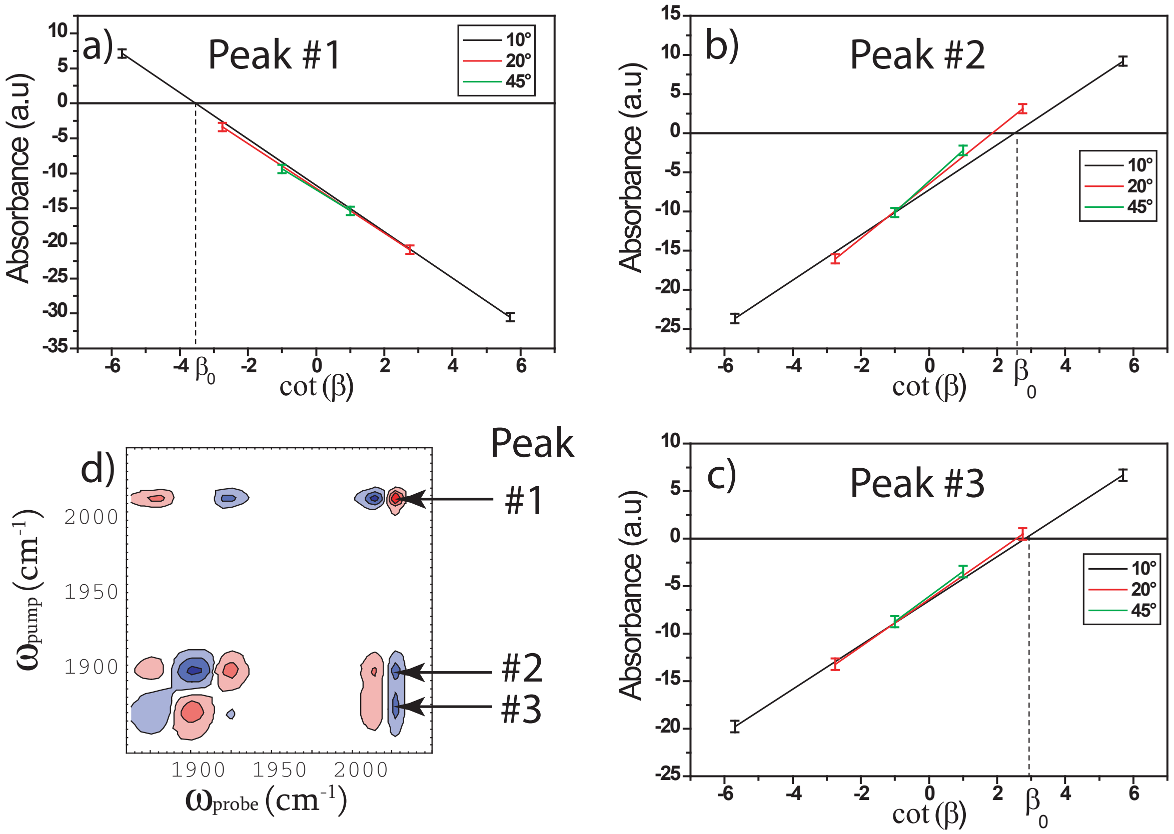

Figure 7.4: In a),b) and c) are displayed the maximum of absorbance of peaks 1,2 and 3 of *d*), for $\beta = \pm 10^{circ}, \pm 20^{circ} and \pm 45^{circ}$. The points with opposite β are connected with a line intersecting the horizontal axis in β_0, used to determine ω

7.3 Scattering suppression

When scattered light from different laser pulses reaches the detector, delay dependent interference patterns arise, which can be much larger than the desired signal (due to interference between local oscillator and signal field). The dominant scattering signal is usually caused by interference between E_{LO} and the pump fields E_1 and E_2, but interference of the two pump beams may also contribute significantly.

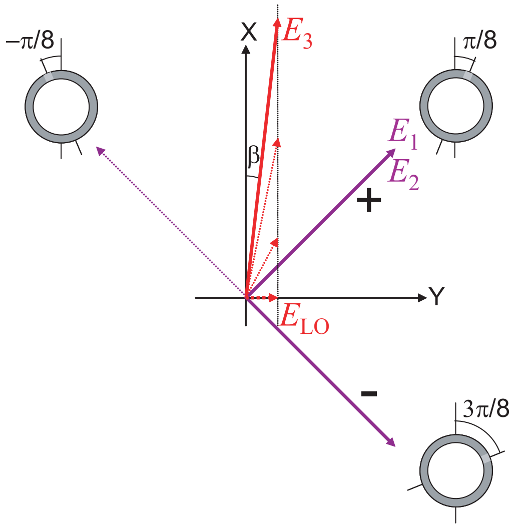

Figure 7.5: Two different arrangements of the half wave plate give scattering contributions opposite values. $\vec{E}_{in}$ represents de pump polarisation before half-wave plate while $\vec{E}_{\pm\beta}$ are the output polarisation for the orientation of the $\frac{\lambda}{2}$ for the 2 orientations depicted by dashed lines at angle $\theta_{\pm\beta}$. $\vec{E}^{\pm\beta}_{scatt}$ are the projection of the pump vector of the y axis. $\vec{E}_{probe}$ is the vector field of probe before polariser, while $\vec{E}_{LO}$ is the heterodyning field, which is a projection of $\vec{E}_{probe}$ on y axis. $\vec{E}_{scatt}$ and $\vec{E}_{LO}$ can interfere and produce scattering signal. In a), as $\vec{E}_{LO}$ and $\vec{E}^{\pm\beta}_{scatt}$ have opposite orientation, the scattering at $\pm\beta$ will sum up with the subtraction of signals while on b) it will be cancel out.

The quasi-crossed polarizer scheme offers an elegant way to suppress these scattering contributions. The idea is similar to a scheme recently proposed for the complete scatter suppression in 2D-IR measurements in the photon-echo geometry [110], but much easier to implement: The different laser fields must be manipulated in a way to reverse the sign of the signal field E_S, without changing the delays between the other laser fields that may interfere on the detector. In this case, two independent measurements can be carried out with identical scattering contributions but inverted 2D-IR signals. Taking the difference between these two measurements yields scatter-free data.

According to equation 5.15 we can achieve the inversion of the LD-component of the signal field in the pump-probe geometry by changing the pump-polarization from 45° to 135°, as indicated in Fig. 7.5. If the waveplate is rotated in the proper direction, it induces a $\lambda/2$ delay of the X-components of the pump beams, without affecting their Y-components. Only the Y-components of the fields are transmitted by the polarizer that is placed behind the sample, so all scattering signals are constant.

As a result, the difference between the two measurements $\Delta A_{+} - \Delta A_{-}$ not only isolates (and amplifies) the well-defined LD-component of the signal, but also fully eliminates background contributions. The LD signal may of course also be measured by rotating the waveplate in the opposite direction, thus selectively delaying the Y-components of the pump fields (dotted arrow in Fig. 7.5). In this case, however, the scattering signal also changes sign and becomes stronger in the difference signal.

To illustrate the ability of our set-up to eliminate scattering signals, we measured 2D-IR spectra on a highly scattered sample (see Fig. 7.6). We observe in the 2D-IR spectra that for the individual signals acquired at $\pm\beta$, scattering signal along the diagonal perturbs the 2D-IR spectra, hiding somehow the diagonal peaks. Subtracting those two contributions results in the spectra in Fig. 7.6 c, where the scattering is suppressed by the subtraction.

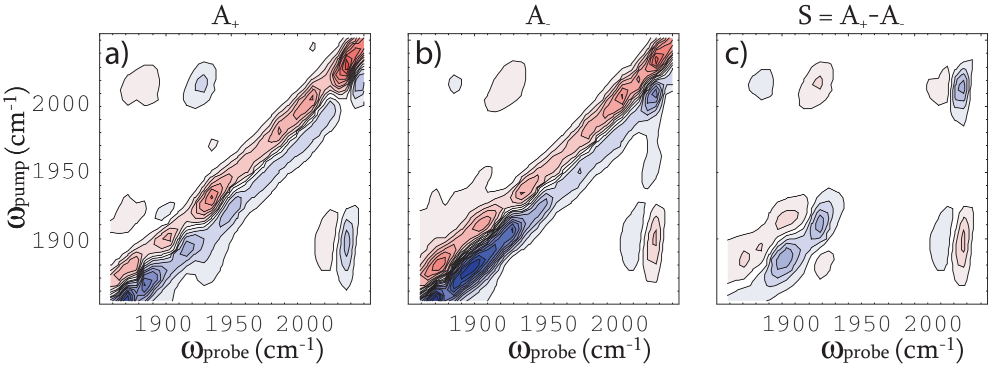

Figure 7.6: a) Scattering signals appearing along the diagonal for ΔA_+ has the same sign as for ΔA_- in b).c) The subtraction of those two signals results in the LD signal free of scattering and background contributions.

7.4 Discussion

Two of the main limiting factors to perform reliable 2D-IR spectra are the size of the signals and the unwanted scattering signals. The scheme presented here greatly enhances the sensitivity of the 2D-IR technique, while suppressing the scattering contribution to the signal. This way, amplification of the signals permits to study weaker absorber or low concentrated samples.

The scattering contribution that often blurs the interesting signals can be suppressed completely by a simple subtraction of datasets. It is interesting to compare this method of scattering suppression to other schemes used in the pump-probe geometry. The most common technique being delay dithering, or in a more defined way, the variation of the waiting time t_2 between the pump pulse(s) and the probe pulse in units of π/ω_0, the center frequency of the pulses. The result is a pseudo inversion of the relative phase between pump(s) and probe [111], which inverts the scattering contribution at ω_0, without modifying the 2D-IR or pump-probe signal significantly [40]. By summing over data recorded at three different delays, scattering can thus be suppressed by more than two orders of magnitude over a bandwidth of 10% [40]. In interferometer-based 2D-IR spectroscopy it is also possible to chop the pump-beam (E_2)in the static arm of the interferometer [38]. This allows one to fully eliminate interference terms between E_1 and the local oscillator, while the Fourier transform along t_1 suppresses the static scattering contribution [38]. Both techniques do not suppress interference terms between E_1 and E_2, but they can be employed in combination with our polarizer method to compensate for imperfect alignment of the waveplate in the pump beam. The principle of scatter suppression by our polarization method is probably most closely related to pulse shaping techniques. When the pump-pulse pair is generated by a pulse shaper [39], the relative sign of the two pump beams can be inverted without changing their delay (true inversion), provoking an inversion of the signal. Full scattering suppression (including interference between E_1 and E_2) nevertheless requires four measurements [32]. Ideally, the different measurements required to acquire the scatter-free signal should be carried out within the shortest possible time in order to reduce noise and minimize the effect of intensity drifts. In our crossed-polarizer scheme the pump pulse polarization can in principle be changed on a shot-to-shot basis using a photoelastic modulator (PEM) [29] instead of rotating a waveplate on a second to minute timescale. However, commercially available mid-IR modulators simultaneously change the refractive index for the X and Y components of the incident light, compromising the possibility to maintain a constant delay between scattered fields. A possible future improvement of our method could thus be the combination of fast delay modulation (by a wobbling Brewster window [110]and polarization modulation(by a PEM), which can lead to an effective delay change of only the X-components of the pump beams.

Suppressing isotropic signal is also an interesting feature of this method which is not illustrated here, but which can have an application when thermalization effects rise in time and overlap interesting signals, and affecting anisotropy data for example [13, 112–115].

Removing signals arising from transition with well defined dipole orientation is another application of this technique that could be used for example for the mapping of the anisotropy of broad inhomogeneous features around the diagonal. Cancelling the signal on one side of a spectral band will for example leave a small absorption of the other side for example, and the anisotropy can then be mapped with only one measurement. This could also reveal different anisotropy relaxation from one side of the spectrum relative to the other, as it is for example when hydrogen bonding is responsible for spectral shift in the spectrum and also alters diffusion relaxation [115, 116].

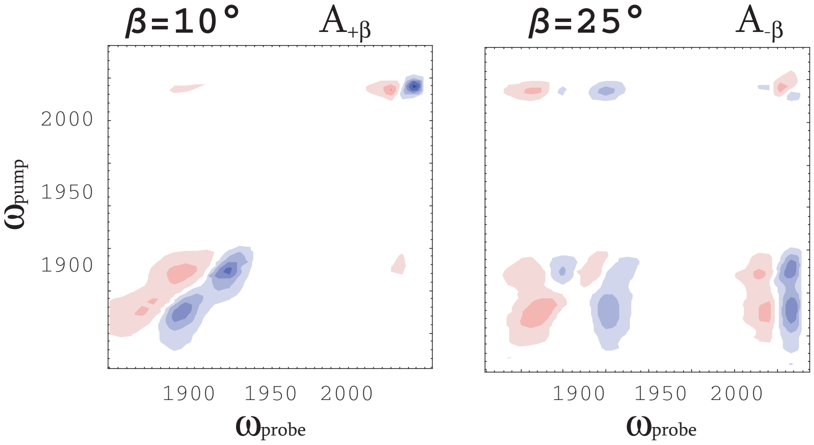

Figure 7.7: a) Elimination of cross peak at an angle of 10°. b) Elimination of diagonal peak with an angle of 25°

The increased accuracy in the determination of angles between transitions dipoles is also an important feature of this technique. In this particular case, the angle calculated from Fig 7.4 are not totally consistent with what is expected, but what we want to emphasize here is the improvement when compared with the conventional used of parallel and perpendicular measurements. This technique suffers from the same drawback as the traditional method do, such as the sensitivity to isotropic background (that shift up the points of Fig. 7.4 and shift the of the value of β_0), but the precision of the measure can be improved by more than 20 according to Fig. 5.3. We applied here the technique on quasi perpendicular transition dipoles, but as shown in section 5.4, the improvement in accuracy is best when transition dipoles angle is near magic angle, where the usual method fails. We also believe that our method will allow one to determine angle between transition dipoles of weak absorbers in condition when it was not possible before, because of the impossibility to get enough signal for parallel and perpendicular probing.

7.5 Dispersive measurements

7.5.1 Kramers-Kronig and causality

The Kramers-Kronig transformation relates the absorption and dispersion spectra and is a consequence of causality. It means that any causal and real response function R(t) will lead to a complex spectra, whose real and imaginary part are related through Kramers-Kronig transformation.

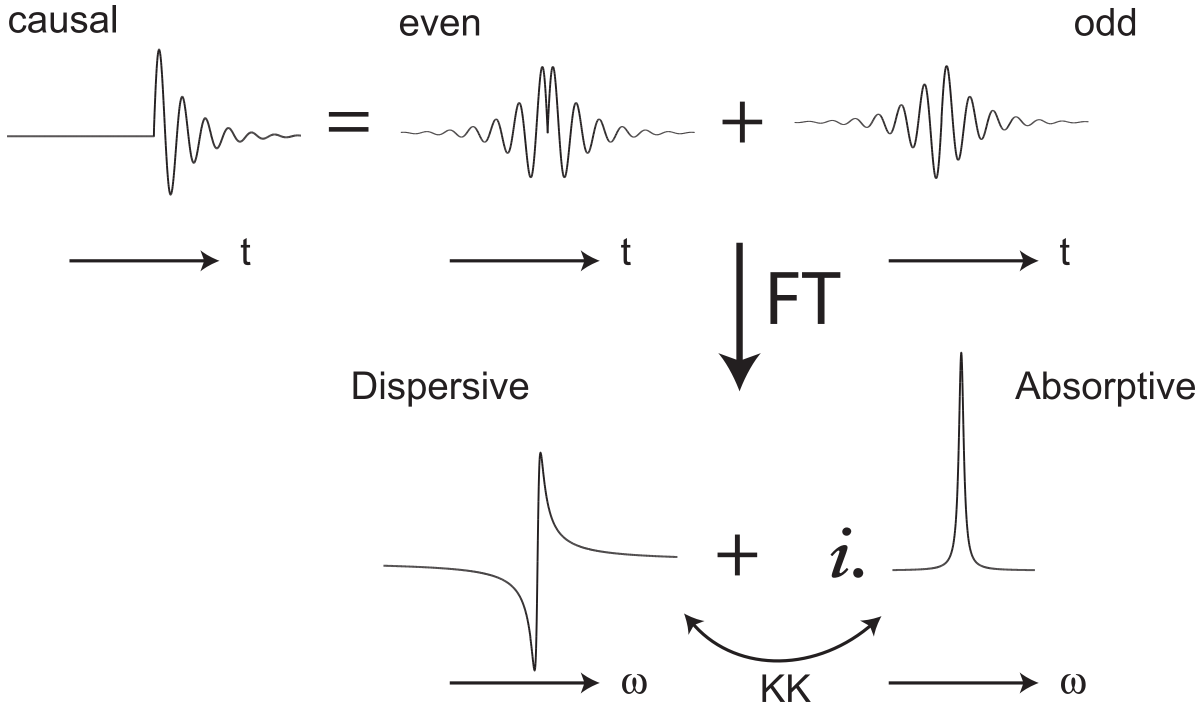

Figure 7.8: A causal response function can be decomposed into the sum of a odd and even function. Each of them leads, after fourier transform (FT), to the absorptive and dispersive lineshapes in frequency, which are related through the Kramers-Kronig relation (KK).

From the property of the Fourier transform, we know that any odd function results in a pure imaginary transform, while any even function gives a purely real function. In fact, in linear spectroscopy, the odd part of the response function is the one which is $\frac{\pi}{2}$ phase shifted relative to the excitation field, while the even part of the response is in phase with the excitation field. The field emitted, of free induction decay, is proportional to the derivative of the polarization and has an additional phase $\frac{\pi}{2}$ phase shift. The odd part of the response function gives rise to a field which is π shifted relative to excitation and interferes destructively with it, causing an absorption (see Fig. 7.8). In a same way, the even part of the response gives rise to a field with a $\frac{\pi}{2}$ phase shift relative to excitation but is not accessible as it does not modulate the measured intensity.

Usually, the third order signals measured in the pump-probe geometry are purely absorptive [38, 40], the only difference with linear spectroscopy is that now probe fields is now also affected by transient species. This is not the case in the four wave mixing geometry, where rephasing and non-rephasing signals are measured independently, and then combined to lead to an absorptive spectrum [34]. Because they are emitted in the same direction in the pump-probe geometry, they sum-up directly on the detector and lead to the absorptive lineshape. It is then possible to do the same manipulation described above to determine a dispersive spectrum from an absorptive one.

In fact, performing the inverse Fourier transform on the absorptive signal leads to an odd function (see Fig. 7.8) in the time domain. Enforcing causality by zeroing negative times results in a causal response function. Transforming back this causal function gives rise to the complex spectrum consisting of real dispersive and imaginary absorptive spectra. Calculating the dispersive spectrum this way is equivalent to do a pseudo Kramers-Kronig transformation of the absorptive signal [109, 111].

Here, we show that it is possible, with little modification of our set-up, to measure dispersive spectra directly, this is possible by phase-shifting the LO by $\frac{\pi}{2}$.

We saw in chapter 1, that the time-domain signal can be written as :

$$S(t) \propto \Re\left(E_{LO}E_{sig}(t)\right) \tag{7.1}$$

if we add up a phase factor of $\frac{\pi}{2}$ to the LO, we obtain :

$$S(t) \propto \Re\left(e^{i\frac{\pi}{2}}E_{LO}E_{sig}(t)\right) \tag{7.2}$$

Or in the frequency domain :

$$\begin{aligned} \Re S(\omega) &\propto \Re\left(e^{i\frac{\pi}{2}}E_{LO}E_{sig}(\omega)\right) \\ \Re S(\omega) &\propto \Im\left(E_{LO}E_{sig}(\omega)\right) \end{aligned} \tag{7.3}$$

This way, we exchange the real part and the imaginary part of the signal and measure now a dispersive spectrum instead of an absorptive one.

7.5.2 Obtaining rephasing and non-rephasing spectra

In pump-probe spectroscopy, and in particular in 2D-IR, the rephasing $\mathbf{R^R}$ and the non rephasing $\mathbf{R^{NR}}$ responses contribute to the signal. They are usually not accessible individually in the pump probe geometry, as they are emitted in the same direction. Rephasing and non-rephasing diagrams have a different phase dependence regarding the pump pulses relative phase, and can be isolated by manipulating this phase [32, 39, 109]. In our 2D-IR set-up, the probe axis is directly given by the spectrometer and the array detector. The pump axis is obtained from the Fourier transform of the measured time domain signal. If we rewrite the response functions as a sum of rephasing ($R^R(t)$) and non-rephasing ($R^{NR}(t)$) contributions :

$$\mathbf{R}(t_1, t_3) = \mathbf{R^R}(t_1, t_3) + \mathbf{R^{NR}}(t_1, t_3) \tag{7.4}$$

Now, the polarization, which is the triple convolution of the response functions with the three excitation pulses can be written, in the impulsive limit, as :

$$P^{(3)}(t_1, \omega_3) \propto i^3 \int e^{(i\omega_3 t_3)+\phi_3}\left(e^{-\Delta\phi_{1,2}}\mathbf{R^R}(t_1, t_3) + e^{\Delta\phi_{1,2}}\mathbf{R^{NR}}(t_1, t_3)\right) dt_3 \tag{7.5}$$

The rephasing response functions depend on $-\Delta\phi_{1,2}+\Delta\phi_{3,LO})$ while the non-rephasing ones depend on $\Delta\phi_{1,2}+\Delta\phi_{3,LO})$. The heterodyne signal, after Fourier transform along t_3 is :

$$S^{\Delta\phi_{1,2},\Delta\phi_{3,LO}}(t_1,\omega_3) \propto \Re\left(e^{i(\Delta\phi_{3,LO})}\left(e^{i(-\Delta\phi_{1,2})}\mathbf{R}^{\mathbf{R}}(t_1,\omega_3) + e^{i(+\Delta\phi_{1,2})}\mathbf{R}^{\mathbf{NR}}(t_1,\omega_3)\right)\right) \tag{7.6}$$

which reflects the signal that we actually measure, as the spectrometer does the Fourier transformation along t_3, and the t_1 time is scanned directly by the interferometer. We plot the signal with two frequency axis, and have to perform a Fourier transformation along t_1, which finally gives the expressions :

$$\Re S^{0,0}(\omega_1,\omega_3) \propto \Re\left(\mathbf{R}^{\mathbf{R}}(\omega_1,\omega_3) + \mathbf{R}^{\mathbf{NR}}(\omega_1,\omega_3)\right) \tag{7.7}$$

$$\Re S^{0,\frac{\pi}{2}}(\omega_1,\omega_3) \propto \Im\left(-\mathbf{R}^{\mathbf{R}}(\omega_1,\omega_3) - \mathbf{R}^{\mathbf{NR}}(\omega_1,\omega_3)\right) \tag{7.8}$$

$$\Re S^{\frac{\pi}{2},0}(\omega_1,\omega_3) \propto \Im\left(\mathbf{R}^{\mathbf{R}}(\omega_1,\omega_3) - \mathbf{R}^{\mathbf{NR}}(\omega_1,\omega_3)\right) \tag{7.9}$$

$$\Re S^{\frac{\pi}{2},\frac{\pi}{2}}(\omega_1,\omega_3) \propto \Re\left(\mathbf{R}^{\mathbf{R}}(\omega_1,\omega_3) - \mathbf{R}^{\mathbf{NR}}(\omega_1,\omega_3)\right) \tag{7.10}$$

The first two signals correspond to the absorptive and dispersive spectra discussed above, both can be obtained experimentally, or calculated one from the other with a pseudo Kramers-Kronig transformation.

The last two can not be measured directly in our case, because they require to be able to modify the pump pulses relative phase. This can be done with the use of a pulse shaper and has been demonstrated before [39, 109]. There is a way to obtained them mathematically by applying the pseudo Kramers-Kronig transformation along the pump axis t_1. By doing so, we calculate $S^{\frac{\pi}{2},0}$ from $S^{0,0}$ and $S^{\frac{\pi}{2},\frac{\pi}{2}}$ from $S^{0,\frac{\pi}{2}}$. Then the combination of the different signals $S^{\Delta\phi_{1,2},\Delta\phi_{3,LO}}$ leads to the complex rephasing and non-rephasing spectra :

$$\begin{aligned}\mathbf{R}^{\mathbf{R}}(\omega_1,\omega_3) &\propto \Re\left(S^{0,0}(\omega_1,\omega_3) + S^{\frac{\pi}{2},\frac{\pi}{2}}(\omega_1,\omega_3)\right) + i\Im\left(S^{\frac{\pi}{2},0}(\omega_1,\omega_3) - S^{0,\frac{\pi}{2}}(\omega_1,\omega_3)\right)\\ \mathbf{R}^{\mathbf{NR}}(\omega_1,\omega_3) &\propto \Re\left(S^{0,0}(\omega_1,\omega_3) - S^{\frac{\pi}{2},\frac{\pi}{2}}(\omega_1,\omega_3)\right) - i\Im\left(S^{\frac{\pi}{2},0}(\omega_1,\omega_3) + S^{0,\frac{\pi}{2}}(\omega_1,\omega_3)\right)\end{aligned} \tag{7.11}$$

Usually, when measured with the four wave mixing technique, only the real part of the rephasing and non-rephasing spectra are shown, and the dispersive is ignored.

In this section, we show that we can measure absorptive or dispersive spectra experimentally with only very little modification of the crossed polarizer set-up. Additionally, we demonstrate experimentally how to obtain the rephasing and non-rephasing part of the response function, knowing the absorptive and dispersive spectra.

7.5.3 Experimental set-up

We used here the 2D-IR set-up used before and modified it to the purpose of measuring dispersive spectra.

First, for the probe beam, the two polarisers are now crossed, and a glass plate (stress plate SP on Fig 7.9) is placed with the principal axis at 45° relative to the probe polarization. Without stress on the plate, no light goes through the second polariser and no signal is detected.

When adding stress on the plate, the linearly X-polarized incoming field becomes slightly elliptical. The long axis of the ellipse (X) is the intense probe field, while the short axis is the $\frac{\pi}{2}$ phase shifted field E_{LO} in the Y direction, which will heterodyne the signal field. Now, we create a Y-polarized heterodyning field with a $\frac{\pi}{2}$ phase shift relative to the probe field, whose intensity depends on the amount of stress applied on SP. This will lead to the measurement of a dispersive lineshape.

Second, we used crossed polarisers instead of beamsplitters in the interferometer that creates a pair of perpendicular pump pulses (see Fig 7.9). This way, we measure either the $\langle XYXY\rangle$ or the $\langle YXXY\rangle$ polarisation tensors, depending on the orientation of the half-wave plate in

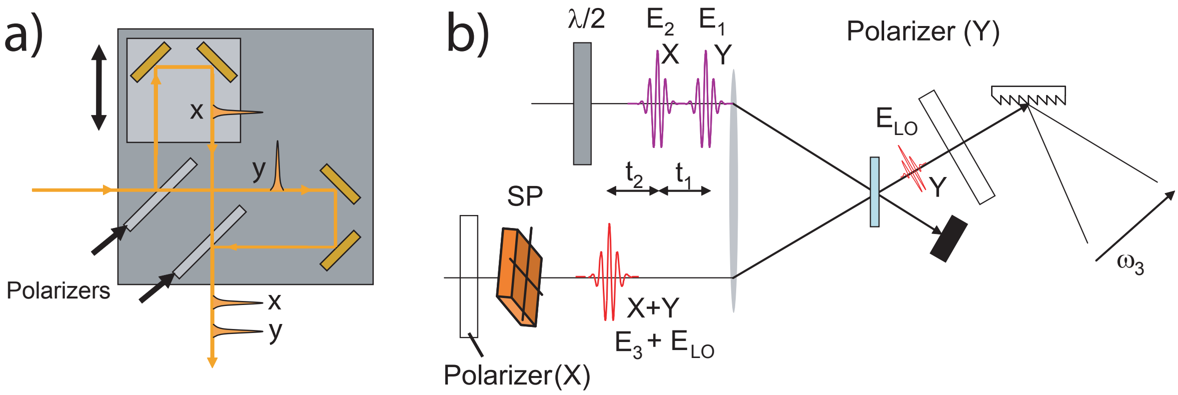

Figure 7.9: a) Interferometer with polarizers instead of beamsplitters is used to generate a pair of perpendicular pump pulses b) The pair of perpendicularly polarised pump pulses can be rotated with a half-wave plate. The two polarisers in the probe beam are crossed, and the stress plate SP at 45° allows to create a $\frac{\pi}{2}$ phase shifted field E_{LO} perpendicularly polarized relative to the probe E_3.

the pump beam [1].

---

[1] We could use the previous polarisation for the pump pulses, i.e. at 45°, which would create the sum of tensors $\langle XYXY\rangle + \langle XXXY\rangle$, but the latter cancels in the dipole approximation and does not contribute to the signal.

7.5.4 Results

We measured first the absorptive and dispersive spectra of azide in water using our technique. The asymmetric stretch of azide in water absorbs around 2050 cm^{-1} and is well isolated from other absorption bands. Azide is a probe of its environment and has been studied before in water [119].

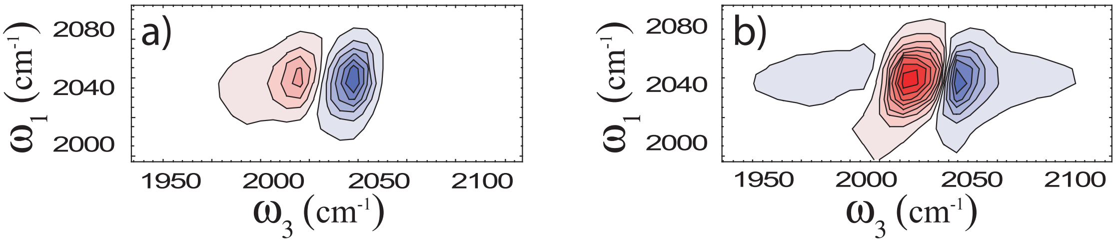

Figure 7.10: a) absorptive and b) dispersive spectra of azide in water, taken in the same polarisation condition $\langle XYXY \rangle$.

The absorptive spectrum was measured without stress on the waveplate, and with a small angle between the probe beam polarisers. The dispersive one was measured with completely crossed polarisers, and with some stress applied on SP. We took care that the amount of light on the detector was the same in the two cases. The two spectra are depicted in Fig.7.10.

From the measured absorptive and dispersive spectra of Fig. 7.10, we calculated the respective dispersive and absorptive spectra, by applying the pseudo Kramers-Kronig relation as described before. These spectra are shown on Fig. 7.11.

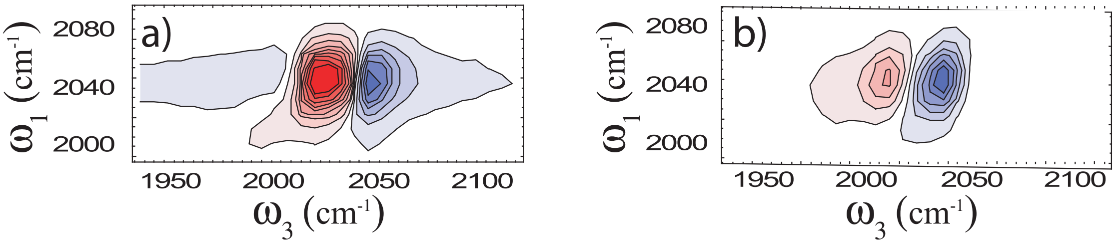

Figure 7.11: a) dispersive and b) absorptive spectra of azide in water, calculated from the measured spectra of Fig. 7.10.

From these spectra, we calculated the real part of the rephasing and non-rephasing spectra, by applying relation 7.11. This lead to the spectra in Fig. 7.12.

7.5.5 Discussion

Dispersive spectra, if directly measured (Fig 7.10) or calculated from the absorptive spectra (Fig 7.11) are very similar. It is the same for the measured and calculated absorptive spectra. It shows that the pseudo Kramers-Kronig transformation gives reliable results in that particular case.

To our opinion, the fact that the pseudo Kramers-Kronig transformation works so well in this case is twofold :

- First, the asymmetric stretch of azide is well isolated from other absorption bands, that could induce a dispersive contribution in the spectral window considered here.

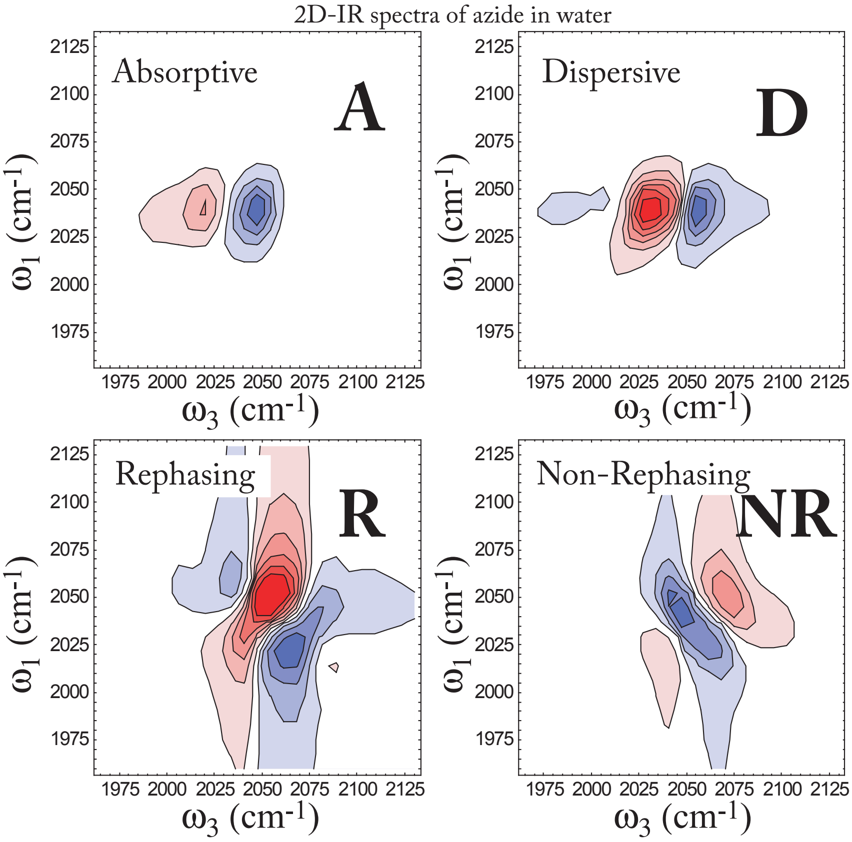

Figure 7.12: Real parts of the measured absorptive (A) and dispersive (D),and calculated rephasing (R) and non-rephasing (NR) spectra using Eq. 7.11.

- Second, the positive and negative features of the absorption contribute to opposite dispersion in a similar amplitude, so that the dispersive spectra has all its amplitude in the spectral range captured by our spectrometer.

In general, dispersive spectra are more extended in frequency than absorptive spectra (they decay in $\frac{1}{\omega}$ when absorptive spectra decay in $\frac{1}{\omega^2}$). Acquiring an absorptive spectrum requires to measure on a smaller spectral window. It is consequently easier to acquire an absorptive spectrum and deduce the dispersive spectrum than the other way around. We can see this effect for one single transition in Fig. 7.13a, where we show an absorptive lineshape similar to the azide's linear spectrum. The corresponding dispersive spectrum extends much more in frequency and requires to measure on a wider spectral range.

This is different if we consider a transient spectrum, where ground and excited state contribute to the signal. This is seen in Fig. 7.13b, where we considered a bleaching, matching the lineshape of Fig. 7.13a and the excited state absorption with a larger lineshape and displaced in frequency to match the anharmonic shift of azide. We see here that the contribution to the dispersion comes from both positive and negative features of the absorption. Those two contributions cancel out away from the absorption, and the dispersive spectrum converges to zero in a similar manner as the absorptive one. Also, the asymmetry of the dispersive spectrum reproduces well the 2D-IR spectrum of azide in Fig. 7.10b or Fig. 7.11a, and is due to the different broadness of the ground state and excited state bands.

The interest of measuring directly a dispersive spectrum is somehow reduce given the fact

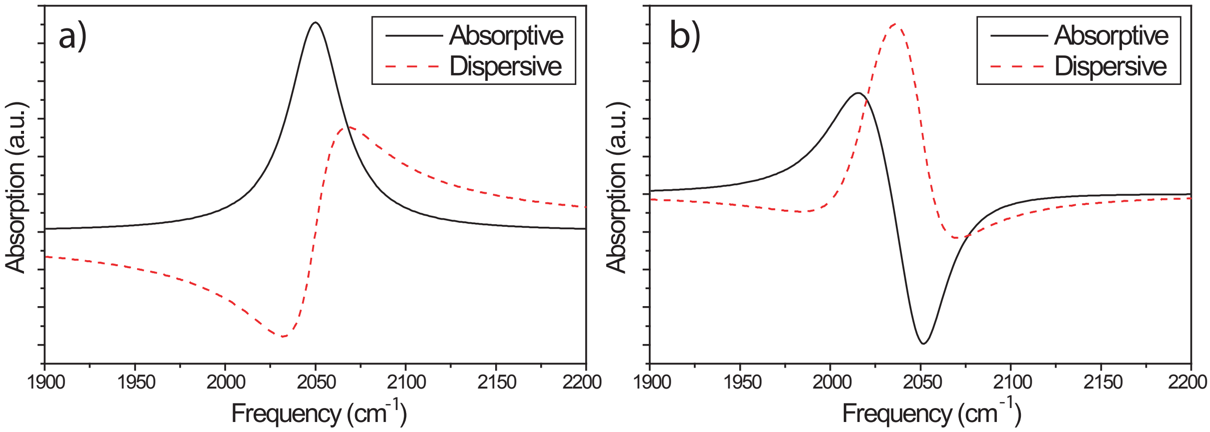

Figure 7.13: a) Absorptive and dispersive lineshapes of a single positive band (Lorentzian, centred at 2040 cm^{-1} with FWHM 36 cm^{-1}). b) Absorptive and dispersive lineshapes when considering two absorption bands with opposite sign and different line broadness.(Lorentzian, negative and positive centred at 2040 cm^{-1} and 2070 cm^{-1} and with FWHM 36 cm^{-1} and 40 cm^{-1} respectively)

that we can obtain it through the Kramers-Kronig relation. But it is interesting to use this technique in order to obtain the rephasing and non-rephasing spectra (or more Feynman pathways), which carry different information, as some more peaks contribute in the non-rephasing spectra [32, 120].

The peak shape of rephasing and non-rephasing spectra is a combination of absorptive and dispersive features. This is seen from the spectra of Fig. 7.12, where the peaks extends in frequency along both axis. This is also evident from Eq. 7.11, where we see that the determination of the rephasing and non-rephasing spectra requires to sum absorptive and dispersive spectra together.

7.6 Conclusion

Using polarizers, the different fields of a third order experiment in the pump probe geometry can be controlled independently, which makes it possible to boost anisotropic signals to levels that can otherwise only be reached in non-collinear experimental geometries. In a certain sense, polarization takes on the role of directional phase matching. At first sight, this seems to "consume" the polarization degree of freedom of the experiment, which is usually used for the determination of intramolecular angles. Here we have shown how this measurement can be carried out with even better precision when recording two amplified spectra with opposite polarizer orientations. This method also offers an elegant way of suppressing scattering signals and selected peaks in the 2D-IR spectrum, making it a very simple, versatile and powerful implementation of 2D-IR spectroscopy.

The possibility to measure dispersive spectra adds up flexibility to the technique. The further determination of rephasing and non-rephasing contribution is also an interesting feature. Here, the acquisition of absorptive and dispersive spectra necessitate to rotate a polarizer and add stress to the tunable waveplate. This takes time, and the noise affecting each spectrum can be different due to the slow laser fluctuations. It is in principle possible to acquire absorptive and dispersive spectra alternatively on a shot to shot basis by using a PEM. With crossed polarizers, the PEM could alternatively act as an half-wave plate or a small retardation wave plate, with the laser synchronized to it, as illustrated in chapter 6.

Polarization enhancement is also promising for fifth order experiments like transient 2D-IR spectroscopy, where dichroism can be even larger [124]. Even when the delay between the first (electronic) excitation and the subsequent IR excitations becomes longer than the rotational diffusion time, amplification would still possible because the IR excitation restores the linear dichroism, which can be exploited in the way presented in this article.

Conclusion

In this thesis, we have explored ultrafast UV-IR and 2D-IR spectroscopies with the aim of studying molecular structure with better accuracy. By manipulating the polarizations of the light pulses in the experiment, we developed methods to improve their sensitivity to the molecular structure. We applied these methods on novel photoswitches that are promising prototypes for achieving molecular rotors.

We have studied a biomimetic molecule, based of the NAIP scheme proposed by Olivucci and co-workers. This ZW-NAIP molecule is a potentially unidirectional rotor which completes half a cycle on the picosecond time scale. The rotation is achieved with a *cis/trans* isomerization along a double bond. We showed with our techniques of ultrafast spectroscopy, that we can gain a direct insight into the isomerization mechanism and access structural parameters over the course of the rotation.

We developed new strategies for improving the sensitivity of ultrafast UV-IR and 2D-IR spectroscopies to molecular structure. For the case of UV-IR experiment, we first showed that a fast modulation of the polarisation improves the quality of the anisotropy data. Second, amplifying the LD component of the molecular response, we showed that we can improve significantly the signal to noise ratio of a pump-probe spectrum, leading to an improvement in the determination of the angles between transition dipoles. The simplicity of the set-up, combined with high quality polarizers, proved that it is possible to acquire spectra of samples with weak oscillator strengths or at low concentrations, with the possibility of removing isotropic backgrounds, and increasing the accuracy of angle determination.

The extension of our method to 2D-IR spectroscopy leads to the same advantages of accuracy in angle determination and improved signal to noise ratio. It is additionally possible to completely eliminate scattering contributions. Usually the signal size competes with scattering when one wants to measure low absorbance samples. In our case, we combine the signal increase with the scattering suppression and the background reduction. This gives the pump-probe geometry new strengths that makes it a more attractive choice when compared with a four wave mixing geometry.

As an extension of the technique, we showed the possibility of improving the flexibility of the set-up by measuring dispersive spectra, from which rephasing and non-rephasing spectra could be deduced. These findings have motivated further investigations, now in progress, into the relationship between rephasing, non-rephasing, absorptive and dispersive spectra. The experimental comparison of the four wave mixing set-up with the crossed polarizer technique in collinear geometry should also be investigated. In addition, the methods mentioned above would benefit from higher energies of the incident light pulses, and also from an improvement in the infrared polarizers, in terms of extinction ratio and transmission.

We are confident that the improvement in structure determination presented in this thesis will find interest in the community of time-resolved spectroscopy. The technique can be applied to many problems where molecular structure needs to be determined. The study of larger systems like proteins, which experience structural changes during folding or unfolding could gain from the application of the techniques developed here.

Building synthetic molecular motors powered by light is a challenging task. The biomimetic approach described here is an interesting way to explore this objective, as nature has already provided many examples of molecular machines. The NAIP-type photoswitches are still under development, and there is room for improvement of the quantum yield and the speed of the isomerization process. Also, the ultrafast study presented here will help to understand the link between the mechanism of the isomerization process, its rate and quantum yield. The aim is to reach the quantum yield and rate of isomerization of retinal in rhodopsin. Further synthesis of chiral photoswitches is also of great interest in the context of unidirectional molecular rotation. This will rely on input from computational and organic chemists.

We demonstrated that the detection of unidirectional motion during *cis/trans* isomerization using anisotropy is possible. There are several prerequisites for unidirectional detection which are not yet all completed by the ZW-NAIP molecule presented in this thesis. First we need a high quantum yield of isomerization and large transient absorption signals. Moreover, the time resolution of the experiment must be better than the isomerization time. It is necessary to have an IR vibrational mode with a high degree of localization and preferably spectrally isolated from the other mid-IR modes. This particular vibrational mode has to be part of the rotating moiety of the molecule. It is also better if the non-rotating moiety of the molecule is attached to a heavy chemical group, which can be considered fixed during the rotation. ZW-NAIP also still suffers from limited quantum yield, especially when compared to retinal. However, the study presented here is relevant for further development of photoswitches with improved properties.

The NAIP based photoswitches constitute an interesting alternative to the widely used azobenzene type of photoswitches. Azobenzene photoswitches are linked to peptides to modulate their properties [125, 126] or study the mechanism of energy transport [127] in peptides. Azobenzene suffers from low solubility, and NAIPs are in this regard attractive. Some work is already in progress to incorporate NAIPs into DNA. ZW-NAIP is a good candidate, as the large dipole change accompanying isomerization could also be used to modulate the fluorescence properties of DNA.

Two-dimensional infrared spectroscopy and anisotropy measurements are interesting tools for chemists to follow fundamental chemical processes, like bond breaking and formation, or *cis/trans* isomerization. The measurement principle proposed in this thesis was applied only to third order spectroscopies. The extension of the technique to higher order spectroscopies is possible. The fifth order transient 2D-IR (T2DIR) spectroscopy for example could benefit from the ideas exposed in this thesis, as the value of the anisotropy can be even larger in this experiment [124].

In conclusion, the techniques developed here constitute a new contribution to the application of ultrafast spectroscopies for transient structure determination. The study of processes such as *cis/trans* isomerization and ultrafast rotation give insights that will inform the development of faster and more efficient molecular machines.

Appendix A

Double sided Feynman diagrams and the evolution of the density matrix

The expression of the 3^{Rd} order polarisation in Eq. 1.1 involves a commutator that gives rise, with some approximations mentioned in section A.1, to a sum of 8 different terms that describe different pathways for the evolution of the density matrix, considering we are dealing with a isolated 2-level system[1]. More pathways have to be considered when dealing with a set of coupled transitions, which will give rise to cross peaks and the 2D-IR spectra [32]. To each of this pathway corresponds a response function R_n, that constitute mathematical representation of the molecular response. This appendix aims to introduce a graphical representation of the response functions with the use of double sided Feynman diagrams, made popular by Mukamel [31] and intensively used in the literature [14, 130–132]. These diagrams allow an intuitive representation of the response function, and in the case of third order spectroscopy, will connect the response functions to the usual terminology used in pump-probe spectroscopy like bleaching, excited state absorption (ESA) and stimulated emission (SE). There are different conventions for drawing those Feynman diagrams [133–135], and here is presented one adopted in particular by Hamm and Zanni [32].

A.1 Third order non-linear Polarisation

Making use of the Rotating Wave Approximation (RWA) and the time-ordering of the light pulses [32, 130], and for a two-level system, the commutator of Eq. 1.1 will develop in a sum of height terms that we can write as follows :

$$\begin{aligned}
R^{(3)} &= \langle \hat{\mu}(t_3+t_2+t_1)\,[\hat{\mu}(t_2+t_1),[\hat{\mu}(t_1),[\hat{\mu}(0),\rho(-\infty)]]]\rangle \\
&= \langle \hat{\mu}(t_3+t_2+t_1)\hat{\mu}(t_1)\rho(-\infty)\hat{\mu}(0)\hat{\mu}(t_2+t_1)\rangle \quad \Rightarrow \quad R_1 \\
&+ \langle \hat{\mu}(t_3+t_2+t_1)\hat{\mu}(t_2+t_1)\rho(-\infty)\hat{\mu}(0)\hat{\mu}(t_1)\rangle \quad \Rightarrow \quad R_2 \\
&+ \langle \hat{\mu}(t_3+t_2+t_1)\hat{\mu}(0)\rho(-\infty)\hat{\mu}(t_1)\hat{\mu}(t_2+t_1)\rangle \quad \Rightarrow \quad R_3 \\
&+ \langle \hat{\mu}(t_3+t_2+t_1)\hat{\mu}(t_2+t_1)\hat{\mu}(t_1)\hat{\mu}(0)\rho(-\infty)\rangle \quad \Rightarrow \quad R_4 \\
&- \langle \hat{\mu}(t_3+t_2+t_1)\hat{\mu}(t_2+t_1)\hat{\mu}(0)\rho(-\infty)\hat{\mu}(t_1)\rangle \quad \Rightarrow \quad R_5 = R_1^* \\
&- \langle \hat{\mu}(t_3+t_2+t_1)\hat{\mu}(t_1)\hat{\mu}(0)\rho(-\infty)\hat{\mu}(t_2+t_1)\rangle \quad \Rightarrow \quad R_6 = R_2^* \\
&- \langle \hat{\mu}(t_3+t_2+t_1)\hat{\mu}(t_2+t_1)\hat{\mu}(t_1)\rho(-\infty)\hat{\mu}(0)\rangle \quad \Rightarrow \quad R_7 = R_3^* \\
&- \langle \hat{\mu}(t_3+t_2+t_1)\rho(-\infty)\hat{\mu}(0)\hat{\mu}(t_1)\hat{\mu}(t_2+t_1)\rangle \quad \Rightarrow \quad R_8 = R_4^*
\end{aligned} \tag{A.1}$$

---

[1] For a 3-level systems, the expression will give rise to 12 terms [130]

The star refers to complex conjugate and R and NR refer to rephasing and non-rephasing diagrams. The terms rephasing and non-rephasing describe the sign of the first and second coherences.(Opposite sign lead to rephasing diagram, same sign gives non-rephasing diagrams).

The corresponding Feynman diagrams for each response function are :

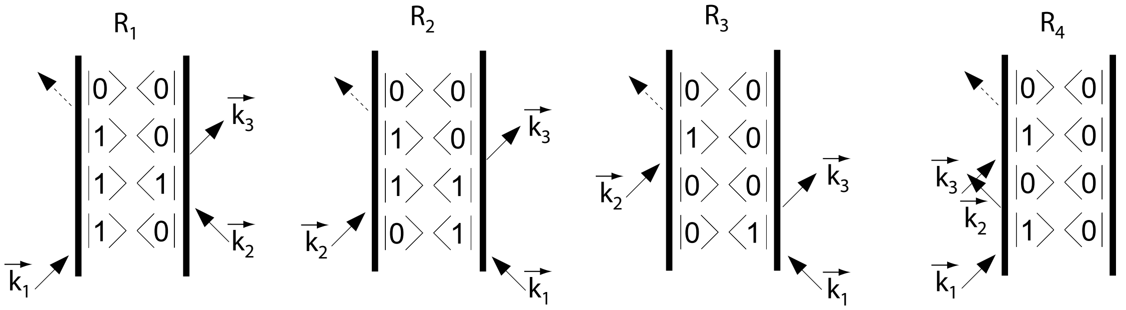

Figure A.1: Feynman diagrams for a two level system.R$_1$ and R$_4$ are non-rephasing diagrams, while R$_2$ and R$_3$ are rephasing diagrams.

Following the rule described in [32,136] we can calculate the response function corresponding to each Feynman diagram. For example, we have :

$$R_2 = \imath\mu_{01}^4 e^{+\imath\omega_{01}t_1} e^{-t_1/T_2} e^{-t_2/T_1} e^{-\imath\omega_{01}t_3} e^{-t_3/T_2} \tag{A.2}$$

where T$_1$ and T$_2$ are the population relaxation time and homogeneous lifetimes respectively. R$_2$ is a rephasing diagram, as the complex exponential terms in t$_1$ and t$_3$ have opposite signs.

A.2 Double sided Feynman diagrams : rules

Double sided Feynman diagrams represents the evolution of the density matrix including the interaction with the light field. To each of the response functions of Eq.A.2 correspond a a Double Sided Feynman Diagram, that are constructed following the set of rules described below.

A.2.1 Rules

The construction of double sided feynman diagrams requires to apply the set of following rules :

- The left and right vertical lines represent the time evolution of the ket $|...\rangle$ and the bra $\langle...|$ of the density matrix.
- Time runs from bottom to top.
- Interactions with the dipole operator are represented by arrows. The last interaction, which originates from the trace $P^{(n)}(t) = \langle\hat{\mu}(t)\rho^{(n)}(t)\rangle$, is emission and hence indicated using a dotted arrow.
- Each diagram has a sign $(-1)^n$, where n is the number of interactions from the right.
- An arrow pointing towards the system represents an up-climbing of bra or ket of the density matrix, while an arrow pointing away represents a de-excitation.

- An arrow pointing to the right represents an electric field with $e^{-i\omega t+i\overrightarrow{k}\cdot\overrightarrow{r}}$, while an arrow pointing to the left represents an electric field with $e^{+i\omega t-i\overrightarrow{k}\cdot\overrightarrow{r}}$. This rule expresses the fact that the real electric field

$$E(t) = 2E'(t)\cdot\cos(\omega t - \overrightarrow{k}\cdot\overrightarrow{r} - \phi)$$

  can be separated into positive and negative frequencies

$$E(t) = E'(t)\cdot\left(e^{-i\omega t+i\overrightarrow{k}\cdot\overrightarrow{r}+i\phi} + e^{+i\omega t-i\overrightarrow{k}\cdot\overrightarrow{r}-i\phi}\right).$$

- The emitted light, i.e. the last interaction, has a frequency and a wavevector which is the sum of the input frequencies and wavevectors (considering the appropriate signs).
- The system must end in a population state.

Also, by convention, only the diagrams with the last interaction emitting from the ket (left side of density matrix) are considered [2].

A.2.2 Interpretation

First, Feynman diagrams are separated in two categories : rephasing and non-rephasing diagrams. This terminology comes from the photon-echo experiments, as only rephasing diagrams creates an echo signal. The distinction is made looking at the sign of the coherences in the expression of the different R_i. If coherences oscillates with the opposite sign, we have a rephasing diagram, and a non-rephasing diagram otherwise. It is easy to determine is a diagram is a rephasing or a non-rephasing one graphically : if the arrow k_1 and k_3 are in the same direction, we have a non-rephasing diagram, if the are pointing in opposite direction, we have a rephasing diagram.

From the rules described above, we can see that rephasing diagrams are all all emitted in the $k_s = k_1 - k_2 + k_3$ direction, while rephasing diagrams are emitted in the $k_s = -k_1 + k_2 + k_3$. This is a way to measure independently R and NR spectra in a photon-echo geometry. In pump probe, as $k_1 = k_2$, so we get $k_s = k_3$ and we measure simultaneously all Feynman diagrams.

The sum of rephasing and non-rephasing spectra leads to an absorptive spectra which are usually preferably displayed in literature, as they are more intuitive to interpret (see section 7.5).

---

[2] The symmetric diagram ending with an emission from the bra is the complex conjugate of the one emitting from ket

Appendix B

Isotropic averages and direction cosines

In the condensed phase, molecules are randomly distributed over all possible orientation in the 3-dimensional space. The media is said to be isotropic. Calculating the signal emitted from such an assembly of molecules requires to average over the contribution of every possible orientation of the molecules. In the case of spectroscopy, the important quantity is the transition dipole moment, which interacts with the polarised electric field. To perform this averaging, we will use the properties of direction cosines, detailed below, and apply it to the particular problem of 3^{rd} order spectroscopy.

B.1 Direction cosines

Direction cosines are useful when one needs to know the relative orientation of two set of axes. In the case of spectroscopy, we need to know the relation between an electric field, which polarisation is expressed in the laboratory frame, and a transition dipole operator, which orientation is expressed in the molecular frame. The connection between those two set of axis can be done using direction cosines, which will be very useful afterwards to perform isotropic averages [137–139]. We need to define the rotation matrix that will transform on set of axes into the other :

$$\mathbf{R} = \begin{pmatrix} l_{xx} & l_{xY} & l_{xZ} \\ l_{yx} & l_{yY} & l_{yZ} \\ l_{zx} & l_{zY} & l_{zZ} \end{pmatrix} \tag{B.1}$$

where the $l_{ii'}$ terms are defined as the angles between the i $(i = x, yorz)$ axis of the molecular frame and the i' $(i' = X, Y or Z)$ axis of the laboratory frame :

$$l_{xX} = cos(\widehat{x, X}) \tag{B.2}$$

as is shown in Fig.B.1.

If we take for example the laboratory frame as a reference, and a transition dipole moment with a certain orientation in the molecular frame $\overrightarrow{\nu}_{m}ol$, its new coordinates in the lab frame $\overrightarrow{\mu}_{l}ab$ is :

$$\overrightarrow{\mu}_{lab} = \mathbf{R}.\overrightarrow{\mu}_{mol} \tag{B.3}$$

B.2 Isotropic averages of direction cosines

Now, if we need to get some isotropic averages, instead of calculating space integrals, we can just take the tabulated values of direction cosines and direction cosine products :

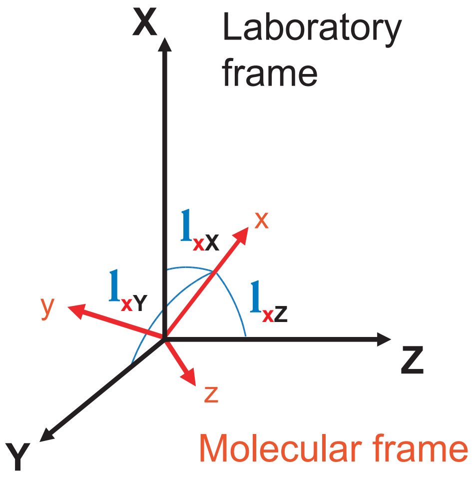

[H]

$$\langle l_{ii'} \rangle = 0 \tag{B.4}$$

$$\langle l_{ii'} l_{jj'} \rangle = \frac{1}{3}\delta_{ij}\delta_{i'j'} \tag{B.5}$$

$$\langle l_{ii'} l_{jj'} l_{kk'} \rangle = \epsilon_{ijk}\epsilon_{i'j'k'} \tag{B.6}$$

$$\langle l_{ii'} l_{jj'} l_{kk'} l_{ll'} \rangle = \frac{1}{30}[\delta_{ij}\delta_{kl}(4\delta_{i'j'}\delta_{k'l'} - \delta_{i'k'}\delta_{j'l'} - \delta_{i'l'}\delta_{j'k'}) \tag{B.7}$$

$$+\delta_{ij}\delta_{il}(-\delta_{i'j'}\delta_{k'l'} + 4\delta_{i'k'}\delta_{j'l'} - \delta_{i'l'}\delta_{j'k'}) \tag{B.8}$$

$$+\delta_{il}\delta_{jk}(-\delta_{i'j'}\delta_{k'l'} - \delta_{i'k'}\delta_{j'l'} + 4\delta_{i'l'}\delta_{j'k'})] \tag{B.9}$$

with $i, j, k, l = x, y, z$ and i', j', k' and $l' = X, Y, Z$

B.3 Isotropic averages of the response functions

The aim is to calculate the general orientational term :

$$\langle(\overrightarrow{u}_{sig}.\overrightarrow{e}_{LO})(\overrightarrow{u}_3.\overrightarrow{e}_3)(\overrightarrow{u}_2.\overrightarrow{e}_2)(\overrightarrow{u}_1.\overrightarrow{e}_1)\rangle \tag{B.10}$$

Which can be easily calculated with the general formulae derived by A.Tokmakoff [140] or R.Hochstrasser [44] :

$$\begin{aligned}
a =& \frac{1}{30}[\langle cos(\theta_{u_3,u_{sig}})cos(\theta_{u_1,u_2})\rangle \\
&(4cos(\theta_{e_{LO},e_3})cos(\theta_{e_1,e_2}) - cos(\theta_{e_{LO},e_2})cos(\theta_{e_3,e_1}) - cos(\theta_{e_{LO},e_1})cos(\theta_{e_2,e_3})) \\
&+ \langle cos(\theta_{u_2,u_{sig}})cos(\theta_{u_1,u_3})\rangle \\
&(-cos(\theta_{e_{LO},e_3})cos(\theta_{e_1,e_2}) + 4cos(\theta_{e_{LO},e_2})cos(\theta_{e_3,e_1}) - cos(\theta_{e_{LO},e_1})cos(\theta_{e_2,e_3})) \\
&+ \langle cos(\theta_{u_1,u_{sig}})cos(\theta_{u_2,u_3})\rangle \\
&(-cos(\theta_{e_{LO},e_3})cos(\theta_{e_1,e_2}) - cos(\theta_{e_{LO},e_2})cos(\theta_{e_3,e_1}) + 4cos(\theta_{e_{LO},e_1})cos(\theta_{e_2,e_3}))]
\end{aligned} \tag{B.11}$$

Where the angles θ_{e_i,e_j} are the relative angles between the polarised pulses of the different interactions.

This equation was used to fill out the table in chapter 1, with $P_2(cos(\theta_{u_i,u_j}) = \frac{1}{2}(3cos^2(\theta_{u_i,u_j})+1)$.

Appendix C

Müller Matrix Calculus

C.1 Introduction

Stokes vector is a 1×4 vector describing the polarization and intensity of a light beam [128]. It is useful when dealing with light which is not perfectly polarised; it replaces the Jones vector which deals only with perfect polarisation. The first element of the Stokes vector represents the intensity of the light, and is interesting in our case as it is directly the quantity that is measured by the detector. The effect of an optical system on the polarisation of light is modelized from the Stokes vector entering the system and applying Müller matrix calculus, which leads to the Stokes vector of light out of the system.

Müller matrices are 4×4 used to model optical elements which have an effect on polarisation or intensity of the beam. All linear effects such as absorption, dichroism or birefringence can be described using Müller matrices. This aim of this appendix is to give to the reader the tools to derive the equations in section 6.5.

C.2 The Stokes Vector

The Stokes vector $\overrightarrow{S}$ describes the intensity and degree of polarisation of light, using 4 parameters know as the Stokes parameters, which are, in the basis (X,Y) of the laboratory frame :

- $s_0 = |E_x|^2 + |E_y|^2$
- $s_1 = |E_x|^2 - |E_y|^2$
- $s_2 = 2\Re(E_x E_y^*)$
- $s_3 = 2\Im(E_x E_y^*)$

The Stokes parameters are real and related to observable quantities. The first parameter s_0 is the intensity of light, s_1 is the intensity of horizontal or vertical polarised light, the parameter s_2 gives the amount of linear +45 (or -45) polarised light and s_3 describes the amount of right- or left-circular polarised light in the beam.

And the Stokes vector is composed of these four parameters :

$$\vec{S} = \begin{pmatrix} s_0 \\ s_1 \\ s_2 \\ s_3 \end{pmatrix} \tag{C.1}$$

Unpolarised light	$\begin{pmatrix}1\\0\\0\\0\end{pmatrix}$	Plane of polarisation in the X direction	$\begin{pmatrix}1\\-1\\0\\0\end{pmatrix}$
Plane of polarisation at 45° relative to X	$\begin{pmatrix}1\\0\\1\\0\end{pmatrix}$	Right Circular polarisation	$\begin{pmatrix}1\\0\\0\\1\end{pmatrix}$

And below are some examples of Stokes vectors related to some states of polarisation :

The detectors measure intensities, which are square of the electric fields ("square law detectors"), so the first element of the Stokes vector corresponds to the observable measured on the experiments used in this thesis.

C.3 Müller Matrices of a combination of optical elements

The Müller matrices for each elements used in the set-ups presented in this thesis are :

1. Absorption :

$$M_{Abs} = e^{-A}\begin{pmatrix}1 & 0 & 0 & 0\\ 0 & 1 & 0 & 0\\ 0 & 0 & 1 & 0\\ 0 & 0 & 0 & 1\end{pmatrix}$$

2. Linear Dichroism at 45° :

$$M_{LD}(45°) = \begin{pmatrix}cosh(LD) & 0 & sinh(LD) & 0\\ 0 & 1 & 0 & 0\\ sinh(LD) & 0 & cosh(LD) & 0\\ 0 & 0 & 0 & 1\end{pmatrix}$$

3. Polariser at Θ :

$$M_{LP}(\Theta) = \begin{pmatrix}\frac{(1+r)}{2} & \frac{q\cos 2\theta}{2} & \frac{q\sin 2\theta}{2} & 0\\ \frac{q\cos 2\theta}{2} & \frac{2\sqrt{r}+b\cos^2 2\theta}{2} & \frac{b\cos 2\theta\sin 2\theta}{2} & 0\\ \frac{q\sin 2\theta}{2} & \frac{b\cos 2\theta\sin 2\theta}{2} & \frac{2\sqrt{r}+b\sin^2 2\theta}{2} & 0\\ 0 & 0 & 0 & \sqrt{r}\end{pmatrix}$$

4. Half-wave plate :

$$M_{\frac{\lambda}{2}} = \begin{pmatrix}1 & 0 & 0 & 0\\ 0 & 1 & 0 & 0\\ 0 & 0 & -1 & 0\\ 0 & 0 & 0 & -1\end{pmatrix}$$

5. Linear Birefringence at 45° :

$$M_{LD}(45°) = \begin{pmatrix} 1 & 0 & 0 & 0 \\ 0 & 1 & 0 & 0 \\ 0 & 0 & cos(LB) & -sin(LB) \\ 0 & 0 & sin(LB) & cos(LB) \end{pmatrix}$$

They are two matrices to describe the Photo-Elastic Modulator in his inactive or active states, the first is the identity matrix, the second is that of a half-wave plate. When a succession of n elements have to be considered, each of them is represented by a matrix M_i, the Stokes vector S_{out} going out of the system is calculated knowing S_{in}, through the relation :

$$\overrightarrow{S}_{out} = M_n.M_{n-1}...M_1.\overrightarrow{S}_{in} \tag{C.2}$$

The matrices presented above are valid only when the different effects can be considered individually. When two effect are concomitant, we have to use infinitesimal matrices for each effect and integrate them [50, 129]. For a sample with LD and LB at 45°, plus absorption, the resulting matrix is :

$$M_{sample} = e^{-\overline{A}} \begin{pmatrix} cosh(LD) & 0 & sinh(LD) & 0 \\ 0 & cos(LB) & 0 & sin(LB) \\ sinh(LD) & 0 & cosh(LD) & 0 \\ 0 & -sin(LB) & 0 & cos(LB) \end{pmatrix} \tag{C.3}$$

which is the one used in Eq. 5.28 to determine Eq. 5.33.

Bibliography

[1] F. Crick. *What Mad Pursuit.* Basic Books, 1990.

[2] K. Wuthrich. The way to NMR structures of proteins. *Nature Structural Biology*, 8(11):923–925, 2001.

[3] P. A. Anfinrud, C. Han, and R. M. Hochstrasser. Direct observations of ligand dynamics in hemoglobin by subpicosecond infrared spectroscopy. *Proceedings of the National Academy of Sciences*, 86(21):8387–8391, 1989.

[4] F. Schotte, M. Lim, T.A. Jackson, A.V. Smirnov, J. Soman, J.S. Olson, G.N. Phillips, M. Wulff, and P.A. Anfinrud. Watching a protein as it functions with 150-ps time-resolved x-ray crystallography. *Science*, 300(5627):1944–1947, 2003.

[5] T.S. Rose, M.J. Rosker, and A.H. Zewail. Femtosecond realtime probing of reactions. IV. the reactions of alkali halides. *The Journal of Chemical Physics*, 91(12):7415–7436, 1989.

[6] K.M. Solntsev, O. Poizat, J. Dong, J. Réhault, Y.B. Lou, C. Burda, and L.M. Tolbert. Meta and para effects in the ultrafast excited-state dynamics of the green fluorescent protein chromophores. *Journal OF Physical Chemistry B*, 112(9):2700–2711, 2008.

[7] B. Moine, G. Buntinx, O. Poizat, J. Réhault, C. Moustrou, and A. Samat. Transient absorption investigation of the photophysical properties of new photochromic 3H-naphtho[2,1-b]pyran. *Journal of Physical Organic Chemistry*, 20(11):936–943, 2007.

[8] P. Hamm, M. Lim, and R.M. Hochstrasser. Vibrational energy relaxation of the cyanide ion in water. *Journal of Chemical Physics*, 107(24):10523–10531, 1997.

[9] N. Demirdöven, M. Khalil, and A. Tokmakoff. Correlated vibrational dynamics revealed by two-dimensional infrared spectroscopy. *Physical Review Letters*, 89(23):237401, 2002.

[10] C. Fang, J. Wang, Y. S. Kim, A. K. Charnley, W. Barber-Armstrong, A. B. Smith, S. M. Decatur, and R. M. Hochstrasser. Two-dimensional infrared spectroscopy of isotopomers of an alanine rich alpha-helix. *Journal of Physical Chemistry B*, 108(29):10415–10427, 2004.

[11] I.J. Finkelstein, J. Zheng, H. Ishikawa, S. Kim, K. Kwak, and M.D. Fayer. Probing dynamics of complex molecular systems with ultrafast 2D-IR vibrational echo spectroscopy. *Physical Chemistry Chemical Physics*, 9(13):1533–1549, 2007.

[12] M.L. Cowan, B.D. Bruner, N. Huse, J.R. Dwyer, B. Chugh, E.T.J. Nibbering, T. Elsaesser, and R.J.D. Miller. Ultrafast memory loss and energy redistribution in the hydrogen bond network of liquid H2O. *Nature*, 434(7030):199–202, 2005.

[13] F. Perakis and P. Hamm. Two-dimensional infrared spectroscopy of supercooled water. *The Journal of Physical Chemistry B*, 115(18):5289–5293, 2011.

[14] M. Khalil, N. Demirdöven, and A. Tokmakoff. Coherent 2D IR spectroscopy: molecular structure and dynamics in solution. *The Journal of Physical Chemistry A*, 107(27):5258–5279, 2003.

[15] J.D. Eaves, J.J. Loparo, C.J. Fecko, S.T. Roberts, A. Tokmakoff, and P.L. Geissler. Hydrogen bonds in liquid water are broken only fleetingly. *Proceedings of the National Academy of Sciences of the United States of America*, 102(37):13019–13022, 2005.

[16] J. Manor, P. Mukherjee, Y.S. Lin, H. Leonov, J. L. Skinner, M.T. Zanni, and I.T Arkin. Gating mechanism of the influenza a m2 channel revealed by 1D and 2D IR spectroscopies. *Structure*, 17(2):247–254, 2009.

[17] R.A. Mathies and J. Lugtenburg The primary photoreaction of rhodopsin. In *Handbook of Biological Physics*, volume 3 of *Elsevier Science B.V.* 2000.

[18] H. Kandori, Y. Shichida, and T. Yoshizawa. Photoisomerization in rhodopsin. *Biochemistry-Moscow*, 66(11):1197–1209, 2001.

[19] G.G. Kochendoerfer and R.A. Mathies. Ultrafast spectroscopy of rhodopsins - photochemistry at its best! *Israel Journal of Chemistry*, 35(3-4):211–226, 1995.

[20] A. Warshel. Bicycle-pedal model for 1st step in vision process. *Nature*, 260(5553):679–683, 1976.

[21] R.W. Schoenlein, L.A. Peteanu, R.A. Mathies, and C.V. Shank. The 1st step in vision - femtosecond isomerization of rhodopsin. *Science*, 254(5030):412–415, October 1991.

[22] L.A. Peteanu, R.W. Schoenlein, Q. Wang, R.A. Mathies, and C.V. Shank. The first step in vision occurs in femtoseconds: complete blue and red spectral studies. *Proceedings of the National Academy of Sciences*, 90(24):11762–11766, December 1993.

[23] G. Haran, E.A. Morlino, J. Matthes, R.H. Callender, and R.M. Hochstrasser. Femtosecond polarized pumpprobe and stimulated emission spectroscopy of the isomerization reaction of rhodopsin. *The Journal of Physical Chemistry A*, 103(14):2202–2207, 1999.

[24] R. Gonzalez-Luque, M. Garavelli, F. Bernardi, M. Merchan, M.A. Robb, and M. Olivucci. Computational evidence in favor of a two-state, two-mode model of the retinal chromophore photoisomerization. *Proceedings of the National Academy of Sciences*, 97(17):9379–9384, August 2000.

[25] L.M. Frutos, T. Andruniow, F. Santoro, N. Ferre, and M. Olivucci. Tracking the excited-state time evolution of the visual pigment with multiconfigurational quantum chemistry. *Proceedings of the National Academy of Sciences*, 104(19):7764–7769, May 2007.

[26] A. Melloni, R.R. Paccani, D. Donati, V. Zanirato, A. Sinicropi, M.L. Parisi, E. Martin, M. Ryazantsev, W.J. Ding, L.M. Frutos, R. Basosi, S. Fusi, L. Latterini, N. Ferré, and M. Olivucci. Modeling, preparation, and characterization of a dipole moment switch driven by Z/E photoisomerization. *Journal of the American Chemical Society*, 132(27):9310–9319, 2010.

[27] F. Lumento, V. Zanirato, S. Fusi, E. Busi, L. Latterini, F. Elisei, A. Sinicropi, T. Andruniow, N. Ferré, R. Basosi, and M. Olivucci. Quantum chemical modeling and preparation of a biomimetic photochemical switch. *Angewandte Chemie-International Edition*, 46(3):414–420, 2007.

[28] A. Sinicropi, E. Martin, M. Ryazantsev, J. Helbing, J. Briand, D. Sharma, J. Leonard, S. Haackee, A. Cannizzo, M. Chergui, V. Zanirato, S. Fusi, F. Santoro, R. Basosi, N. Ferre, and M. Olivucci. An artificial molecular switch that mimics the visual pigment and completes its photocycle in picoseconds. *Proceedings of the National Academy of Sciences of the United States of America*, 105(46):17642–17647, 2008.

[29] J. Réhault, V. Zanirato, M. Olivucci, and J. Helbing. Linear dichroism amplification: Adapting a long-known technique for ultrasensitive femtosecond IR spectroscopy. *Journal of Chemical Physics*, 134(12):124516–124516–10, 2011.

[30] J. Réhault and J. Helbing. Angle Determination and Scattering Suppression in polarization-Enhanced Two-Dimensional Infrared Spectroscopy in the Pump-Probe Geometry *Optics Express*, 20(19) 21665–21677 (2012)

[31] S. Mukamel. *Principles of nonlinear optical spectroscopy.* Oxford University Press, 1999.

[32] P. Hamm and M.T. Zanni. *Concepts and Methods of 2D Infrared Spectroscopy.* Cambridge University Press, 2011.

[33] D.M. Jonas. Two-Dimensional Femtosecond Spectroscopy. *Annual Review of Physical Chemistry*, 54(1):425–463, 2003.

[34] M. Khalil, N. Demirdöven, and A. Tokmakoff. Obtaining absorptive line shapes in two-dimensional infrared vibrational correlation spectra. *Physical Review Letters*, 90(4):047401, 2003.

[35] A.H. Zewail. Laser Femtochemistry. *Science*, 242(4886):1645–1653, 1988.

[36] P.O. Stoutland, R.B. Dyer, and W.H. Woodruff. Ultrafast infrared spectroscopy. *Science*, 257(5078):1913–1917, 1992.

[37] P. Hamm, M.H. Lim, and R.M. Hochstrasser. Structure of the amide i band of peptides measured by femtosecond nonlinear-infrared spectroscopy. *Journal Of Physical Chemistry B*, 102(31):6123–6138, 1998.

[38] L.P. DeFlores, R.A. Nicodemus, and A. Tokmakoff. Two-dimensional Fourier transform spectroscopy in the pump-probe geometry. *Optics Letters*, 32(20):2966–2968, 2007.

[39] S.H. Shim and M.T. Zanni. How to turn your pumpprobe instrument into a multidimensional spectrometer: 2D IR and vis spectroscopies via pulse shaping. *Physical Chemistry Chemical Physics*, 11(5):748, 2009.

[40] J. Helbing and P. Hamm. Compact implementation of fourier transform two-dimensional IR spectroscopy without phase ambiguity. *Journal of the Optical Society of America B*, 28(1):171–178, 2011.

[41] R. Hochstrasser, M. Pereira, P. Share, M. Sarisky, Y. Kim, S. Repinec, R. Sension, J. Thorne, M. Iannone, R. Diller, P. Anfinrud, C. Han, T. Lian, and B. Locke. Anisotropy studies of ultrafast dipole reorientations. *Journal of Chemical Sciences*, 103(3):351–362, 1991.

[42] S. Woutersen and P. Hamm. Structure determination of trialanine in water using polarization sensitive two-dimensional vibrational spectroscopy. *The Journal of Physical Chemistry B*, 104(47):11316–11320, 2000.

[43] M.T. Zanni and R.M. Hochstrasser. Two-dimensional infrared spectroscopy: a promising new method for the time resolution of structures. *Current Opinion in Structural Biology*, 11(5):516–522, 2001.

[44] R.M. Hochstrasser. Two-dimensional IR-spectroscopy: polarization anisotropy effects. *Chemical Physics*, 266(2-3):273–284, 2001.

[45] A.T. Krummel and M.T. Zanni. DNA vibrational coupling revealed with two-dimensional infrared spectroscopy: insight into why vibrational spectroscopy is sensitive to DNA structure. *Journal of Physical Chemistry. B*, 110(28):13991–14000, 2006.

[46] J. Helbing, K. Nienhaus, G.U. Nienhaus, and P. Hamm. Restricted rotational motion of CO in a protein internal cavity: Evidence for nonseparating correlation functions from IR pump-probe spectroscopy. *The Journal of Chemical Physics*, 122(12):124505, 2005.

[47] M.T. Zanni, N.H. Ge, Y.Sam. Kim, and R.M. Hochstrasser. Two-dimensional IR spectroscopy can be designed to eliminate the diagonal peaks and expose only the crosspeaks needed for structure determination. *Proceedings of the National Academy of Sciences*, 98(20):11265–11270, 2001.

[48] K.K. Lee, K.H. Park, S. Park, S.J. Jeon, and M. Cho. Polarization-angle-scanning 2DIR spectroscopy of coupled anharmonic oscillators: A polarization null angle method. *The Journal of Physical Chemistry B*, 115(18):5456–5464, 2011.

[49] P.N. Butcher and D. Cotter. *The Elements of Nonlinear Optics*. Cambridge University Press, 1991.

[50] H.P. Jensen, J.A. Schellman, and T. Troxell. Modulation techniques in polarization spectroscopy. *Applied Spectroscopy*, 32(2):192–200, 1978.

[51] D.J. Dummer, S.G. Kaplan, L.M. Hanssen, A.S. Pine, and Y. Zong. High-quality brewster's angle polarizer for broadband infrared application. *Applied Optics*, 37(7):1194–1204, 1998.

[52] D.S. Alavi, R.S. Hartman, and D.H. Waldeck. Optically heterodyned polarization spectroscopy. measurement of the orientational correlation function. *The Journal of Chemical Physics*, 92(7):4055, 1990.

[53] A. Tokmakoff. Orientational correlation functions and polarization selectivity for nonlinear spectroscopy of isotropic media. i. third order. *The Journal of Chemical Physics*, 105(1):1, 1996.

[54] R.A. Kaindl, M. Wurm, K. Reimann, P. Hamm, A.M. Weiner, and M. Woerner. Generation, shaping, and characterization of intense femtosecond pulses tunable from 3 to 20 mu m. *Journal of the Optical Society of America B-Optical Physics*, 17(12):2086–2094, 2000.

[55] P. Hamm, R.A. Kaindl, and J. Stenger. Noise suppression in femtosecond mid-infrared light sources. *Optics Letters*, 25(24):1798–1800, 2000.

[56] M. Bonmarin and J. Helbing. Polarization control of ultrashort mid-IR laser pulses for transient vibrational circular dichroism measurements. *Chirality*, 21(1E):E298–E306, 2010.

[57] M. Bonmarin *Development of Ultrafast Time-Resolved Chiral Infrared Spectroscopy.* PhD thesis, 2010.

[58] C. Dugave. *Cis-Trans Isomerization in Biochemistry.* Wiley-VCH Verlag GmbH & Co, 2006.

[59] W.J. Wedemeyer, E. Welker, and H.A. Scheraga. Proline cis-trans isomerization and protein folding. *Biochemistry*, 41(50):14637–14644, 2002.

[60] S.C.R. Lummis, D.L. Beene, L.W. Lee, H.A. Lester, R.W. Broadhurst, and D.A. Dougherty. Cis-trans isomerization at a proline opens the pore of a neurotransmitter-gated ion channel. *Nature*, 438(7065):248–252, 2005.

[61] K.P. Lu, G. Finn, T.H. Lee, and L.K. Nicholson. Prolyl cis-trans isomerization as a molecular timer. *Nature Chemical Biology*, 3(10):619–629, 2007.

[62] D. Sampedro, A. Migani, A. Pepi, E. Busi, R. Basosi, L. Latterini, F. Elisei, S. Fusi, F Ponticelli, V Zanirato, and M Olivucci. Design and photochemical characterization of a biomimetic light-driven Z/E switcher. *Journal of the American Chemical Society*, 126(30):9349–9359, 2004.

[63] V. Zanirato, GP. Pollini, C. De Risi, F. Valente, A. Melloni, S. Fusi, J. Barbetti, and M. Olivucci. Synthesis of biomimetic light-driven molecular switches via a cyclopropyl ring-opening/nitrilium ion ring-closing tandem reaction. *Tetrahedron*, 63(23):4975–4982, 2007.

[64] P. Altoè, F. Bernardi, I. Conti, M. Garavelli, F. Negri, and G. Orlandi. Light driven molecular switches: exploring and tuning their photophysical and photochemical properties. *Theoretical Chemistry Accounts: Theory, Computation, and Modeling (Theoretica Chimica Acta)*, 117(5):1041–1059, 2007.

[65] T. Andruniów, N. Ferré, and M. Olivucci. Structure, initial excited-state relaxation, and energy storage of rhodopsin resolved at the multiconfigurational perturbation theory level. *Proceedings of the National Academy of Sciences of the United States of America*, 101(52):17908–17913, 2004.

[66] A. Cembran, F. Bernardi, M. Olivucci, and M. Garavelli. The retinal chromophore/chloride ion pair: Structure of the photo isomerization path and interplay of charge transfer and covalent states. *Proceedings of the National Academy of Sciences*, 102(18):6255–6260, 2005.

[67] B.G. Levine and TJ. Martinez. Isomerization through conical intersections. *Annual Review of Physical Chemistry*, 58:613–634, 2007.

[68] M. Bletz, U. Pfeifer-Fukumura, U. Kolb, and W. Baumann. Ground- and first-excited-singlet-state electric dipole moments of some photochromic spirobenzopyrans in their spiropyran and merocyanine form. *Journal of Physical Chemistry A*, 106(10):2232–2236, 2002.

[69] G. Mayer and A. Heckel. Biologically active molecules with a "light switch". *Angewandte Chemie-International Edition*, 45(30):4900–4921, 2006.

[70] B.L. Feringa. The art of building small: From molecular switches to molecular motors. *Journal of Organic Chemistry*, 72(18):6635–6652, 2007.

[71] K. Hoki, M. Yamaki, and Y. Fujimura. Chiral molecular motors driven by a nonhelical laser pulse13. *Angewandte Chemie International Edition*, 42(26):2976–2978, 2003.

[72] N. Koumura, E.M. Geertsema, M.B. van Gelder, A. Meetsma, and B.L. Feringa. Second generation light-driven molecular motors. unidirectional rotation controlled by a single stereogenic center with near-perfect photoequilibria and acceleration of the speed of rotation by structural modification. *Journal of the American Chemical Society*, 124(18):5037–5051, 2002.

[73] J. Briand. *Ultrafast isomerization and vibrational coherence of biomimetic photoswitches: Experimental investigation by femtosecond transient absorption spectroscopy.* PhD thesis, 2009.

[74] J. Bredenbeck and P. Hamm. Versatile small volume closed-cycle flow cell system for transient spectroscopy at high repetition rates. *Review of Scientific Instruments*, 74(6):3188–3189, 2003.

[75] Gaussian 03, Revision C.02, M.J. Frisch, G.W. Trucks, H.B. Schlegel, G.E. Scuseria, M.A. Robb, J.R. Cheeseman, J.A. Montgomery, Jr., T. Vreven, K.N. Kudin, J.C. Burant, J.M. Millam, S.S. Iyengar, J. Tomasi, V. Barone, B. Mennucci, M. Cossi, G. Scalmani, N. Rega, G.A. Petersson, H. Nakatsuji, M. Hada, M. Ehara, K. Toyota, R. Fukuda, J. Hasegawa, M. Ishida, T. Nakajima, Y. Honda, O. Kitao, H. Nakai, M. Klene, X. Li, J.E. Knox, H.P. Hratchian, J.B. Cross, V. Bakken, C. Adamo, J. Jaramillo, R. Gomperts, R. E. Stratmann, O. Yazyev, A.J. Austin, R. Cammi, C. Pomelli, J.W. Ochterski, P.Y. Ayala, K. Morokuma, G.A. Voth, P. Salvador, J.J. Dannenberg, V.G. Zakrzewski, S. Dapprich, A.D. Daniels, M.C. Strain, O. Farkas, D.K. Malick, A.D. Rabuck, K. Raghavachari, J.B. Foresman, J.V. Ortiz, Q. Cui, A.G. Baboul, S. Clifford, J. Cioslowski, B. B. Stefanov, G. Liu, A. Liashenko, P. Piskorz, I. Komaromi, R.L. Martin, D.J. Fox, T. Keith, M.A. Al-Laham, C.Y. Peng, A. Nanayakkara, M. Challacombe, P.M.W. Gill, B. Johnson, W. Chen, M.W. Wong, C. Gonzalez, and J.A. Pople, Gaussian, Inc., Wallingford CT, 2004.

[76] A. Sinicropi, R. Basosi, and M. Olivucci. Recent applications of a QM/MM scheme at the CASPT2//CASSCF/AMBER (or CHARMM) level of theory in photochemistry and photobiology. *Journal of Physics: Conference Series*, 101:012001, 2008.

[77] J. Herbst, K. Heyne, and R. Diller. Femtosecond infrared spectroscopy of bacteriorhodopsin chromophore isomerization. *Science*, 297(5582):822–825, 2002.

[78] R. Gross, C. Schumann, M. M.N. Wolf, J. Herbst, R. Diller, N. Friedman, and M. Sheves. Ultrafast protein conformational alterations in bacteriorhodopsin and its locked analogue BR5.12. *The Journal of Physical Chemistry B*, 113(22):7851–7860, 2009.

[79] P. Hamm, S. M. Ohline, and W. Zinth. Vibrational cooling after ultrafast photoisomerization of azobenzene measured by femtosecond infrared spectroscopy. *The Journal of Chemical Physics*, 106(2):519–529, 1997.

[80] B.L. Feringa, R.A. van Delden, N. Koumura, and E.M. Geertsema. Chiroptical molecular switches. *Chemical Reviews*, 100(5):1789–1816, 2000.

[81] B.L. Feringa, N. Koumura, R.A. van Delden, and M.K.J.T. Wiel. Light-driven molecular switches and motors. *Applied Physics A-Materials Science & Processing*, 75(2):301–308, 2002.

[82] A. Sinicropi, C. Bernini, R. Basosi, and M. Olivucci. A novel biomimetic photochemical switch at work: design of a photomodulable peptide. *Photochemical & Photobiological Sciences*, 8(12):1639–1649, 2009.

[83] E. Drexler. *Nanosystems: Molecular Machinery, Manufacturing, and Computation.* John Wiley & Sons Inc, 1992.

[84] J.P. Sauvage. *Molecular machines and motors.* Springer, 2001.

[85] R.D. Vale and R.A. Milligan. The way things move: Looking under the hood of molecular motor proteins. *Science*, 288(5463):88–95, 2000.

[86] P.D. Boyer. Energy, life, and ATP (Nobel lecture). *Angewandte Chemie International Edition*, 37(17):2296-2307, 1998.

[87] A. Strambi, B. Durbeej, N. Ferr, and M. Olivucci. Anabaena sensory rhodopsin is a light-driven unidirectional rotor. *Proceedings of the National Academy of Sciences*, 107(50):21322–21326, 2010.

[88] N. Koumura, R.W.J. Zijlstra, R.A. van Delden, N. Harada, and B.L. Feringa. Light-driven monodirectional molecular rotor. *Nature*, 401(6749):152–155, 1999.

[89] S.P. Fletcher, F. Dumur, M.M. Pollard, and B.L. Feringa. A reversible, unidirectional molecular rotary motor driven by chemical energy. *Science*, 310(5745):80–82, 2005.

[90] J. Vicario, M. Walko, A. Meetsma, and B.L. Feringa. Fine tuning of the rotary motion by structural modification in light-driven unidirectional molecular motors. *Journal of the American Chemical Society*, 128(15):5127–5135,2006.

[91] M. Klok, N. Boyle, M.T. Pryce, A. Meetsma, W.R. Browne, and B.L. Feringa. MHz unidirectional rotation of molecular rotary motors. *Journal of the American Chemical Society*, 130(32):10484–10485, 2008.

[92] J. iegel. Inventing the nanomolecular wheel. *Science*, 310(5745):63–64, 2005.

[93] D.S. Kliger, J.W. Lewis, C.E. Randall, and R.M.A. Azzam. Polarized light in optics and spectroscopy. *Physics Today*, 44(10):117–118, 1991.

[94] C.V. Shank and E.P. Ippen. Anisotropic absorption saturation with picosecond pulses. *Applied Physics Letters*, 26(2):62, 1975.

[95] J.W. Lewis, R.F. Tilton, C.M. Einterz, S.J. Milder, I.D. Kuntz, and D.S. Kliger. New technique for measuring circular dichroism changes on a nanosecond time scale. application to (carbonmonoxy)myoglobin and (carbonmonoxy)hemoglobin. *Journal of Physical Chemistry.*, 89(2):289–294, 1985.

[96] D. Waldeck. Picosecond pulse induced transient molecular birefringence and dichroism. *The Journal of Chemical Physics*, 74(6):3381, 1981.

[97] D. Che, D.B. Shapiro, R.M. Esquerra, and D.S. Kliger. Ultrasensitive time-resolved linear dichroism spectral measurements using near-crossed linear polarizers. *Chemical Physics Letters*, 224(1-2):145–154, 1994.

[98] S.H. Shim, D.B. Strasfeld, Y.L. Ling, and M.T. Zanni. Automated 2D IR spectroscopy using a mid-IR pulse shaper and application of this technology to the human islet amyloid polypeptide. *Proceedings of the National Academy of Sciences*, 104(36):14197–14202, 2007.

[99] L. Wang, C.T. Middleton, S. Singh, A.S. Reddy, A.M. Woys, D.B. Strasfeld, P. Marek, D.P. Raleigh, J.J. de Pablo, M.T. Zanni, and J.L. Skinner. 2DIR spectroscopy of human amylin fibrils reflects stable -sheet structure. *J. Am. Chem. Soc.*, 133(40):16062–16071, 2011.

[100] A. Keston and J. Lospalluto. Simple ultrasensitive spectropolarimeters. *Federation Proceedings*, 12:229, 1953.

[101] J. Briand, O. Bräm, J. Réhault, J. Léonard, A. Cannizzo, M. Chergui, V. Zanirato, M. Olivucci, J. Helbing, and S. Haacke. Coherent ultrafast torsional motion and isomerization of a biomimetic dipolar photoswitch. *Physical Chemistry Chemical Physics*, 12:3178–3187, 2010.

[102] J. Helbing, L. Bonacina, R. Pietri, J. Bredenbeck, P. Hamm, F. van Mourik, F. Chaussard, A. Gonzalez-Gonzalez, M. Chergui, C. Ramos-Alvarez, C. Ruiz, and J. Lpez-Garriga. Time-resolved visible and infrared study of the cyano complexes of myoglobin and of hemoglobin I from Lucina Pectinata. *Biophysical Journal*, 87(3):1881–1891, 2004.

[103] C. Niezborala and F. Hache. Measuring the dynamics of circular dichroism in a pump-probe experiment with a babinet-soleil compensator. *Journal of the Optical Society of America B*, 23(11):2418–2424, 2006.

[104] D.B. Shapiro, R.A. Goldbeck, D. Che, R.M. Esquerra, S.J. Paquette, and D.S. Kliger. Nanosecond optical rotatory dispersion spectroscopy: application to photolyzed hemoglobin-CO kinetics. *Biophysical Journal*, 68(1):326–334, 1995. PMID: 7711258 PMCID: 1281691.

[105] P.M. Donaldson, H. Strzalka, and P. Hamm. High sensitivity transient infrared spectroscopy: a UV/Visible transient grating spectrometer with a heterodyne detected infrared probe. *Optics Express*, 20(12):12761-12770, 2012.

[106] J. Helbing and M. Bonmarin. Vibrational circular dichroism signal enhancement using self-heterodyning with elliptically polarized laser pulses. *The Journal of Chemical Physics*, 131(17):174507, 2009.

[107] W. Xiong and M.T. Zanni. Signal enhancement and background cancellation in collinear two-dimensional spectroscopies. *Optics Letters*, 33(12):1371–1373, 2008.

[108] P. Hamm, M. Lim, and R.M. Hochstrasser. Ultrafast dynamics of amide-i vibrations. *Biohysical Journal*, 74(2):A332–A332, 1998.

[109] J.A. Myers, K.L. Lewis, P.F. Tekavec, and J.P. Ogilvie. Two-color two-dimensional fourier transform electronic spectroscopy with a pulse-shaper. *Optics Express*, 16(22):17420–17428, 2008.

[110] R. Bloem, S. Garrett-Roe, H. Strzalka, P. Hamm, and P. Donaldson. Enhancing signal detection and completely eliminating scattering using quasi-phase-cycling in 2D IR experiments. *Optics Express*, 18(26):27067–27078, 2010.

[111] A.W. Albrecht, J.D. Hybl, S.M. Gallagher Faeder, and D.M. Jonas. Experimental distinction between phase shifts and time delays: Implications for femtosecond spectroscopy and coherent control of chemical reactions. *The Journal of Chemical Physics*, 111:10934, 1999.

[112] R.A. Nicodemus, K. Ramasesha, S.T. Roberts, and A. Tokmakoff. Hydrogen bond rearrangements in water probed with temperature-dependent 2D IR. *Journal of Physical Chemistry. Lett.*, 1(7):1068–1072, 2010.

[113] S. Yeremenko, M.S. Pshenichnikov, and D.A. Wiersma. Interference effects in IR photon echo spectroscopy of liquid water. *Physical Review A*, 73(2):021804, 2006.

[114] A.J. Lock, S. Woutersen, and H.J. Bakker. Ultrafast energy equilibration in hydrogen-bonded liquids. *Journal of Physical Chemistry. A*, 105(8):1238–1243, 2001.

[115] Y.L.A. Rezus and H.J. Bakker. On the orientational relaxation of HDO in liquid water. *The Journal of Chemical Physics*, 123(11):114502, 2005.

[116] M. Ji and K.J. Gaffney. Orientational relaxation dynamics in aqueous ionic solution: Polarization-selective two-dimensional infrared study of angular jump-exchange dynamics in aqueous 6M NaClO4. *The Journal of Chemical Physics*, 134(4):044516, 2011.

[117] D.C Hutchings, M. Sheikbahae, D.J. Hagan, and E.W. Vanstryland. Kramers-Kronig relations in nonlinear optics. *Optical and Quantum Electronics*, 24(1):1–30, 1992.

[118] J.D. Hybl, A.W. Albrecht, S.M. Gallagher Faeder, and D.M. Jonas. Two-dimensional electronic spectroscopy. *Chemical Physics Letters*, 297(3-4):307–313, 1998.

[119] P. Hamm, M. Lim, and R.M. Hochstrasser. Vibrational relaxation and dephasing of small molecules strongly interacting with water. *Ultrafast Phenomena XI, Oxford University Press, New York*, 63:514–516, 1998.

[120] J. Réhault and J. Helbing. Exploring the polarization degrees of freedom in collinear two-dimensional infrared spectroscopy. *Ultrafast Phenomena XVIII, Oxford University Press, New York*, 2012.

[121] W.P. de Boeij, M.S. Pshenichnikov, and D.A. Wiersma. Heterodyne-detected stimulated photon echo: applications to optical dynamics in solution. *Chemical Physics*, 233(2-3):287–309, 1998.

[122] P. Tian. Femtosecond phase-coherent two-dimensional spectroscopy. *Science*, 300(5625):1553–1555, 2003.

[123] J.C. Vaughan, T. Hornung, K.W. Stone, and K.A. Nelson. Coherently controlled ultrafast four-wave mixing spectroscopy. *The Journal of Physical Chemistry A*, 111(23):4873–4883, 2007.

[124] J. Bredenbeck, J. Helbing, and P. Hamm. Transient two-dimensional infrared spectroscopy: Exploring the polarization dependence. *The Journal of Chemical Physics*, 121(12):5943–5957, 2004.

[125] C. Renner and L. Moroder. Azobenzene as conformational switch in model peptides. *Chembiochem*, 7(6):869–878, 2006.

[126] R. Pfister, J. Ihalainen, P. Hamm, and C. Kolano. Synthesis, characterization and applicability of three isotope labeled azobenzene photoswitches. *Organic & Biomolecular Chemistry*, 6(19):3508, 2008.

[127] V. Botan, Ellen H.G. Backus, R. Pfister, A. Moretto, M. Crisma, C. Toniolo, P.H. Nguyen, G. Stock, and P. Hamm. Energy transport in peptide helices. *Proceedings of the National Academy of Sciences*, 104(31):12749–12754, 2007.

[128] G.G. Stokes. *Mathematical and Physical Papers*, volume 4 of *Cambridge Library Collection - Mathematics*. Cambridge University Press, 2009.

[129] T.C. Troxell and H.A. Scheraga. Electric dichroism and polymer conformation. I. theory of optical properties of anisotropic media, and method of measurement. *Macromolecules*, 4(5):519–527, 1971.

[130] P. Hamm. 2D Infrared spectroscopy. In *Handbook of High-resolution Spectroscopy*. John Wiley & Sons, Ltd, 2011.

[131] Y.C. Cheng and G.R. Fleming. Dynamics of light harvesting in photosynthesis. *Annual Review of Physical Chemistry*, 60:241–262, 2009.

[132] D.M. Jonas. Two-dimensional femtosecond spectroscopy. *Annual Review of Physical Chemistry*, 54(1):425–463, 2003.

[133] T.K. Yee and T.K. Gustafson. Diagrammatic analysis of the density operator for nonlinear optical calculations: Pulsed and cw responses. *Physical Review A*, 18(4):1597–1617, 1978.

[134] Y. Prior. A complete expression for the third-order susceptibility $\chi^{(3)}$ - perturbative and diagrammatic approaches. *IEEE Journal of Quantum Electronics*, 20(1):37 –42, 1984.

[135] R.W. Boyd and S. Mukamel. Origin of spectral holes in pump-probe studies of homogeneously broadened lines. *Physical Review A*, 29(4):1973–1983, 1984.

[136] P. Hamm. Principles of non-linear optical spectroscopy: A practical approach or: Mukamel for dummies, 2005.

[137] D.L. Andrews and T. Thirunamachandran. On three-dimensional rotational averages. *The Journal of Chemical Physics*, 67(11):5026, 1977.

[138] D.L. Andrews and N.P. Blake. Three-dimensional rotational averages in radiation-molecule interactions: an irreducible cartesian tensor formulation. *Journal of Physics A: Mathematical and General*, 22(1):49–60, 1989.

[139] S.S. Andrews. Using rotational averaging to calculate the bulk response of isotropic and anisotropic samples from molecular parameters. *Journal of Chemical Education*, 81(6):877, 2004.

[140] A. Tokmakoff. Orientational correlation functions and polarization selectivity for nonlinear spectroscopy of isotropic media. II. fifth order. *The Journal of Chemical Physics*, 105(1):13, 1996.

Acknowledgements

First, I would like to thank Prof. Peter Hamm for hosting me in his lab. I learned a lot during my PhD in this group and this is thanks to his high level of expectation and the good atmosphere prevailing in his group.

I am grateful to Prof. Hutter, Prof. Seeger, Prof. Krishnan for participating in my PhD committee. I also thank Prof. Vauthey for reviewing my thesis.

Jan Helbing was my PhD advisor, and I thank him for the great help in the lab, with the data and for the numerous discussion we had about science in particular. I appreciated a lot his disponibility, and I am sure many other PhD students will be jealous if I say that I had daily discussion with my advisor ! This thesis owes a lot to him and his ideas, I would have liked to have more time (or more dedication), to explore all the ideas we had. Let's keep that for later maybe.

I thank all the collaborators with whom I worked with for the work on the biomimetic photoswitches: Julien Briand, Jérémie Léonard and Stefan Haacke, and also the groups of Prof. Olivucci, Prof. Chergui and Prof. Zanirato.

I want to thank all the technical support from the PCI. In disorder : Herr Kühne, Roland, Martin, Maja, Sascha, Rolf. The quality of the work done in the lab rely a lot on you and your Swiss efficiency, merci viel mal.

Thank you to all the PhD students and Postdoc from the group. Some former ones, Marco, Matthias, Helen, Paul, Sean and the ones who are still there. I appreciated a lot the final party, I had a great time. Good luck to all of you !

I wish to thank also the graduate school of chemical and molecular science of university Zurich, for the financial support to attend conferences and for the monthly apéros.

Of course I have a particular thank to give to Fivos, for all the good time, the scientific and the terrific discussions. Also for managing the office's music and follow the mood of the day.

Ciao to the running team, Ana, Konstanze and Marcella continue without me girls and keep going please. I have a special thought to Jaime, we miss you a lot.

Thank to all the people I went out with in Zurich, JC and Anaëlle, it was great to meet you and share part of your life. Pierre, I'll miss not being there for Do-bar and friday beers in BQM. The other friends, Cédric, Daphne, Lucas, Valeria, Arne, Vivian, Nicolas, Romain, Samuele, and those I forgot.

Thanks to my parents for the support and for joining the final party and feed with oysters and Champagne all the crazy scientists.

Grazie mille Elsa, per tutto.

Curriculum vitae

Name: Réhault
Surname: Julien
Place and date of birth: Léhon, France, 06.10.1978
Citizenship: French

Professional Experience:

2003–2008 *Research Engineer, Centre National de la Recherche Scientifique (CNRS)*
Laboratoire de Spectrochimie Infrarouge et Raman
University of Lille 1, Lille (France)

Education:

2008–pres. *Ph.D. Program, Graduate School of Chemical and Molecular Sciences*
University of Zurich, Zurich (Switzerland)

1996–2001 *Master of Science Laser and Applications*
University of Lille 1, Lille (France)

1996 *French Scientific Baccalauréat*
Lyce St Martin, Rennes (France)